

NO-A191 182

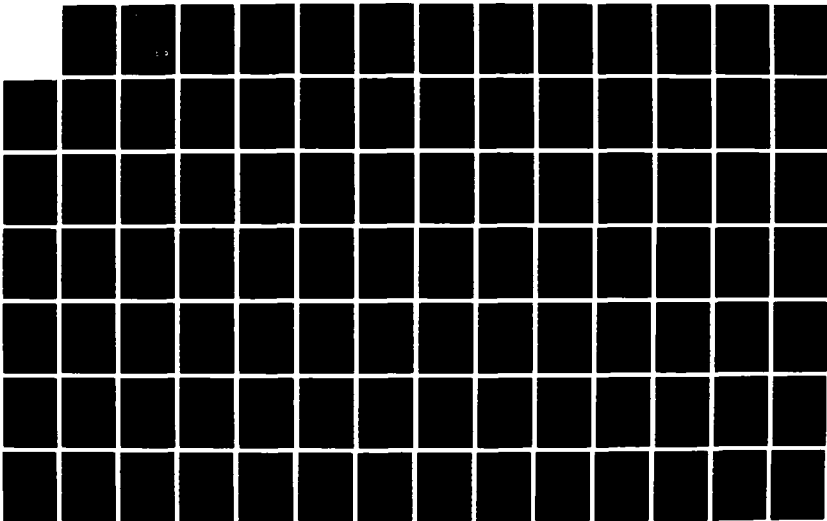
FRAGMENTATION AND PLUGGING FAILURE OF PROJECTILE/TARGET  
SYSTEM(U) LEHIGH UNIV BETHLEHEM PA INST OF FRACTURE AND  
SOLID MECHANICS G C SIH ET AL. MAR 87 NTL-TR-87-18  
DAG846-85-K-0011

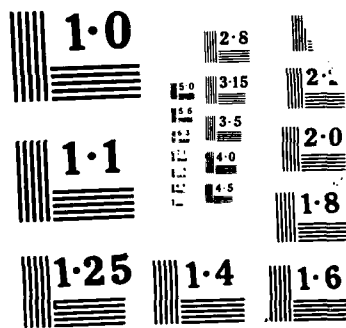
1/2

UNCLASSIFIED

F/G 19/10

NL





AD-A191 182



US ARMY  
LABORATORY COMMAND  
MATERIALS TECHNOLOGY  
LABORATORY

AD

DTIC FILE COPY

MTL TR 87-18

FRAGMENTATION AND PLUGGING FAILURE OF  
PROJECTILE/TARGET SYSTEM

March 1987

G. C. SIH and Y. D. LEE  
Institute of Fracture and Solid Mechanics  
Lehigh University  
Bethlehem, Pennsylvania 18015

FINAL REPORT

Contract No. DAAG46-85-K-0011

Approved for public release; distribution unlimited

DTIC  
ELECTE  
JAN 25 1988  
S H D

Prepared for

U.S. ARMY MATERIALS TECHNOLOGY LABORATORY  
Watertown, Massachusetts 02172-0001

88 1 14 048

The findings in this report are not to be construed as an official Department of the Army position, unless so designated by other authorized documents.

Mention of any trade names or manufacturers in this report shall not be construed as advertising nor as an official indorsement or approval of such products or companies by the United States Government.

#### DISPOSITION INSTRUCTIONS

Destroy this report when it is no longer needed.  
Do not return it to the originator

**SECURITY CLASSIFICATION OF THIS PAGE (When Data Entered)**

DD FORM 1473 EDITION OF 1 NOV 65 IS OBSOLETE

SECURITY CLASSIFICATION OF THIS PAGE (When Data Entered)

Block No. 20

## ABSTRACT

The energy density theory is applied to analyze the progressive damage of a projectile/target system with emphases placed on failure by fragmentation and/or fracture. Presented is a finite element code that accounts for the exchange of surface and volume energy density in each element. Such an interaction being neglected in the conventional theories of continuum mechanics plays a major role in the damage process where energy is transferred from the projectile to the target during impact. The dynamically loaded elements are not only highly stressed but they also undergo high gradients of strain whose history is no longer preassumed as in the classical approach. The distribution for each time increment is determined analytically. This enables a realistic prediction of the damage states and provides a consistent means of analyzing projectile/target failure. Results are obtained for a projectile made of tungsten impacting a target plate made of 4340 steel at a velocity of 1,200 m/sec. Appropriate time increments are chosen such that a sequence of damage states can be exhibited leading up to the final fracture of the target plate by plugging whose thickness is approximately one-half of that of the target plate.

As thermal/mechanical interaction effects are inherently coupled in the energy density theory, heat dissipation and temperature change are automatically embedded in the solution. Information such as the latent heat used to alter the material microstructure can be found in a straightforward manner for estimating the location and size of the so-called "adiabatic shear band" that occurs during plugging, a topic that will be left for future investigation.

## FOREWORD

The work in this report is prepared for the Army Materials Technology Laboratory (MTL) under Contract No. DAAG46-85-K-0011 with the Institute of Fracture and Solid Mechanics at Lehigh University, Bethlehem, Pennsylvania. The authors are particularly grateful to the Project Manager, Mr. J. F. Dignam and Technical Monitor, Dr. S.-C. Chou from MTL. Their constant interest and encouragement have made the progress in this work possible.

An improved version of the computer code is made for predicting the damage of projectile/target systems where failure takes place predominantly by permanent deformation, fragmentation and/or fracture. Instead of considering the failure of individual elements, a more detailed account of the damage pattern can be obtained from the distribution of the surface and volume energy density. In order to demonstrate the validity of the energy density theory, it is only logical to first consider an example in which the projectile velocity is sufficiently low such that material phase transformation does not occur. The method of approach, however, applies equally well to situations where the solid can transform to liquid and/or gas as the projectile velocity is increased into the hypervelocity range. Unlike the conventional approaches, the energy density theory requires only a knowledge of the initial uniaxial response of the projectile/target system. Change in the local strain rates are determined analytically for each time increment. The proposed methodology has far-reaching significance as it can provide useful information for modeling subscaling tests.

Accession For	
NTIS GRA&I	<input checked="checked" type="checkbox"/>
DTIC TAB	<input type="checkbox"/>
Unannounced	<input type="checkbox"/>
Justification	
By	
Distribution/	
Availability Codes	
Dist	Avail and/or Special
A-1	

## INTRODUCTION

Damage prediction of projectile/target systems has been the subject of many past discussions [1-4]. The majority of the works make use of the classical theories of continuum mechanics by assuming that the constitutive relations of the materials are specified or known as an a priori. These theories are generally referred to as elasticity, plasticity, viscoplasticity, etc., and are not sufficient for describing the projectile/target damage process unless additional failure criteria are invoked. Such a loosely adopted procedure leaves room for arbitrariness in terms of empirical parameters and lacks the consistency and uniqueness required in theoretic prediction. Stress and failure analysis cannot be separated. They should be inherently coupled in the theoretical formulation.

An earlier attempt was made in [5] to analyze the damage of a projectile/target system by application of the energy density theory [6,7]. Data banks were constructed to account for the change in material behavior of the projectile and target as damage occurred progressively. Changes in local strain rates and strain rate history are included such that the dynamic stress and stress behavior of each material element is different and derived independently. For the first time, stress and failure analysis were treated simultaneously. Damage by permanent deformation and/or fragmentation was modelled by application of triangular finite elements. Element failure is assumed to occur when the corresponding surface and/or volume energy density reach their critical values. These elements are thus removed from the analysis and the grid pattern is modified accordingly. This process is repeated for each time increment until the target is completely fractured. The shortcoming of the element failure model became obvious as the solution accuracy depended exclusively on the size of the finite element mesh.



Increasing accuracy can only be achieved at the expense of extensive labor and computer time. Nevertheless, the qualitative feature of target failure by plugging is predicted. What has been accomplished is a preliminary confirmation on the validity of the methodology.

An alternative scheme for determining the progressive damage of projectile/target systems is developed in this investigation. Instead of considering the failure of individual elements, contours of surface and volume energy density are obtained. Damage patterns are then mapped in accordance with the intensity distribution of the energy densities. This may involve the creation of free surface areas, fragmentation over a region or the fracture of solid segments. A much more realistic prediction of projectile/target failure behavior is obtained. Even though results are displayed only on the mechanical fragmentation and plugging of the impacted target, change in local temperature and the formation of adiabatic shear band [8-10] are also contained in the present work. Material transformation that occurs within this narrow band of material adjacent to the plug can be verified by computing for the latent heat. Other thermal properties of the projectile/target material may be made available to check with available experimental data. Study on changes in microstructure is beyond the scope of this investigation.

#### PROJECTILE/TARGET DAMAGE CONSIDERATION

Damage is a process by which material elements experience permanent change and no longer return to their original states. It changes with time and continues to occur if the surface and volume energy density are not evenly proportioned. As a result, the rate change of volume and surface area of each element, i.e.,

$dV/dA$  depends on the rate of energy input. The energy quantities identified with  $dV$  and  $dA$  are, respectively, the volume energy density  $dW/dV$  and surface energy density  $dW/dA$ . Their interdependence<sup>\*</sup> is well-known in the homogeneous nucleation theory of Gibbs. The inclusion of the length parameter  $dV/dA$  in the energy density theory represents a fundamental departure from all existing approaches.

*Damage Plane.* Each unit volume of material in the projectile/target system is considered to be damaged under deformation or strain, say  $\epsilon_{ij}$ . If the rectangular Cartesian coordinates  $(x,y,z)$  are used to denote the original coordinates, then the deformed coordinates  $(\xi,\eta,\zeta)$  locate the so-called "plane of homogeneity" or damage plane. An unique damage or strain state is said to exist for each time increment of loading. It is only on this plane<sup>\*\*</sup> that the volume energy density can be completely determined by

$$\frac{dW}{dV} = \iiint \lambda \left( \frac{dV}{dA} \right)_{\xi} d\epsilon_{\xi} d\epsilon_{\xi} \quad (1)$$

The quantity  $\lambda$  is a proportionality parameter that relates the slope of the equivalent uniaxial stress and strain relation on the damage plane to the rate of change of volume with the surface area, i.e.,

$$\frac{d\sigma_{\xi}}{d\epsilon_{\xi}} = \lambda \left( \frac{dV}{dA} \right)_{\xi} \quad (2)$$

<sup>\*</sup> The surface and volume energy density are assumed to be unconnected in the classical theories of continuum mechanics because of the invokement of  $dV/dA \rightarrow 0$  in the limit. Such a simplification leads to an inaccurate account of energy transmission across the projectile/target interface.

<sup>\*\*</sup> The invariant concept so widely used for deriving constitutive relations in continuum mechanics no longer holds here because the damage plane occupies a definite orientation and is different for each material element.

Hence, the surface energy density  $(dW/dA)_\xi$  can be written as

$$\left(\frac{dW}{dA}\right)_\xi = \left(\frac{dV}{dA}\right)_\xi \frac{dW}{dV} \quad (3)$$

with  $dW/dV$  being a scalar. For a homogeneous and isotropic material, the damage plane can be determined from the assumption that there prevails three orthogonal directions  $(\xi, \eta, \zeta)$  along which the surface energy densities  $(dW/dA)_i$  ( $i = \xi, \eta, \zeta$ ) are equal, i.e.,

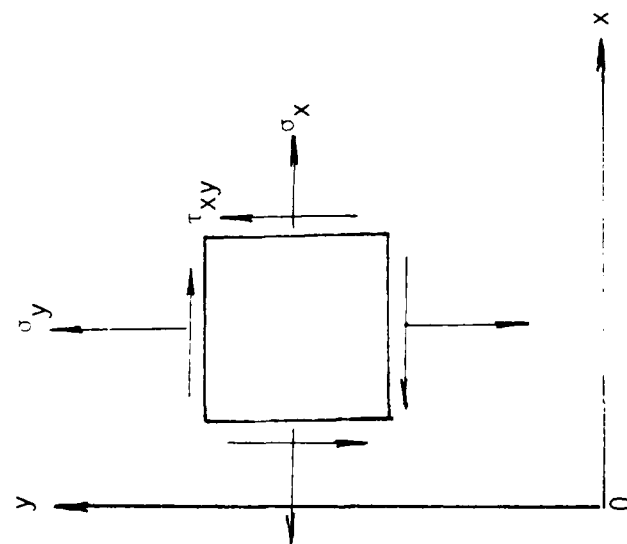
$$\left(\frac{dW}{dA}\right)_\xi = \left(\frac{dW}{dA}\right)_\eta = \left(\frac{dW}{dA}\right)_\zeta = \left(\frac{dW}{dA}\right)_0 \quad (4)$$

This provides an one-to-one correspondence between each element in the projectile/target system under a multi-axial stress or strain state with that in the uniaxial data bank or the value  $(dW/dA)_0$ . Since equation (3) may be generalized to read as

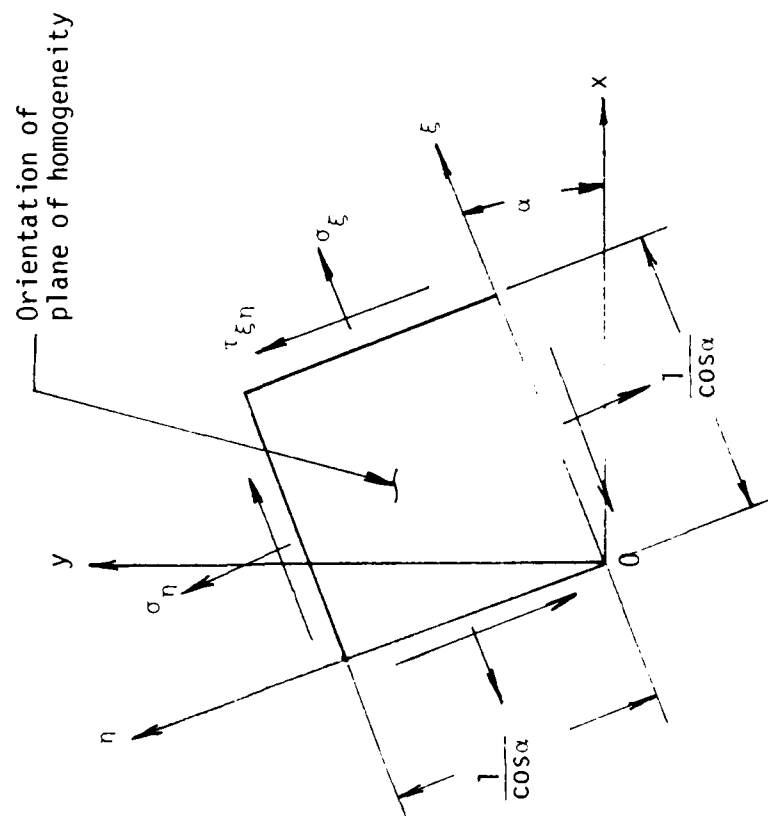
$$\left(\frac{dW}{dA}\right)_i = \left(\frac{dV}{dA}\right)_i \frac{dW}{dV}, \quad i = \xi, \eta, \zeta \quad (5)$$

it follows also that the  $(dV/dA)_\xi$ ,  $(dV/dA)_\eta$  and  $(dV/dA)_\zeta$  are equal on the damage plane.

*Change of Volume with Area.* The quantity  $dV/dA$  is most unique as it is related to the slope of the uniaxial stress and strain curve as indicated in equation (2). For a two-dimensional stress state in Figure 1(a), the corresponding plane of homogeneity or damage plane makes an angle  $\alpha$  with the x- and y-axis as shown in Figure 1(b). The stresses and strains are such that the condition in equation (4) is satisfied. In two dimensions, the damage, say in the z- or  $\zeta$ -



(a) Stress notation



(b) Plane of homogeneity

Figure 1. Stress notation and plane of homogeneity.

direction, may be regarded as constant. This means that  $(dW/dA)_z$  or  $(dW/dA)_\zeta$  remains the same. Alternatively, it can be stated that

$$\left(\frac{dV}{dA}\right)_z \text{ or } \left(\frac{dV}{dA}\right)_\zeta = c \quad (6)$$

where  $c$  is a constant. Without going into details and making use of the results in [7], the strain component in the  $z$ - or  $\zeta$ -direction may be written as

$$\varepsilon_z \text{ or } \varepsilon_\zeta = (c-1)(\varepsilon_\xi + \varepsilon_\eta) \cos \alpha \quad (7)$$

It follows that the  $(dV/dA)_i$  ( $i = \zeta, \eta$ ) expressions are given by [7]

$$\begin{aligned} \left(\frac{dV}{dA}\right)_\zeta &= \frac{\varepsilon_\xi + \varepsilon_\eta}{\left[\left(\frac{c-1}{c}\right)\varepsilon_\xi + \varepsilon_\eta\right] \cos \alpha} \\ \left(\frac{dV}{dA}\right)_\eta &= \frac{\varepsilon_\xi + \varepsilon_\eta}{\left[\varepsilon_\xi + \left(\frac{c-1}{c}\right)\varepsilon_\eta\right] \cos \alpha} \end{aligned} \quad (8)$$

This is referred to as the planar formulation of the energy density theory [6]. The case when  $c \rightarrow 1$  corresponds to the state of plane strain in the classical theory of elasticity with  $\varepsilon_\zeta \rightarrow 0$ . In general,  $c$  can take any appropriate constant greater than unity depending on the constraint in the  $\zeta$ -direction. The determination of the various quantities will be discussed in connection with the finite element procedure.

*Damage Thresholds.* Damage of the projectile/target system will be analyzed by observing the contours of  $dW/dA$  on the damage plane and  $dW/dV$ . Initially, the surface energy density would be more dominant as the projectile first hits the target where energy is transferred across the contact or interface. Fragmenta-

tion may occur as the result of  $(dW/dA)_\xi$  exceeding its critical value. Increase in the volume energy density takes place when the disturbance spreads over a larger portion of the target. The following conditions may serve as a guide for determining the damage pattern:

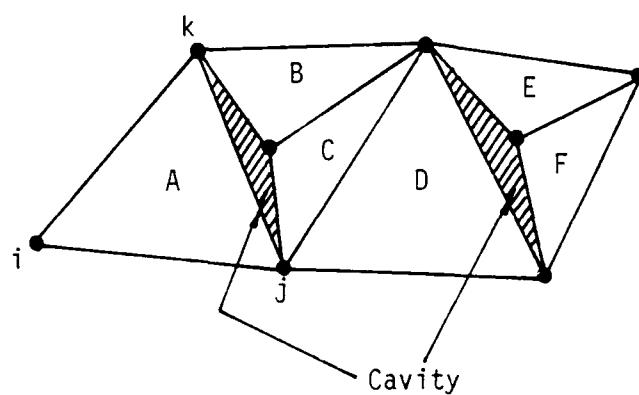
$$\frac{dW}{dV} > \left(\frac{dW}{dV}\right)_c; \quad \left(\frac{dW}{dA}\right)_\xi \approx \left(\frac{dW}{dA}\right)_c, \quad \left(\frac{dV}{dA}\right)_\xi < \left(\frac{dV}{dA}\right)_c \quad (9)$$

or

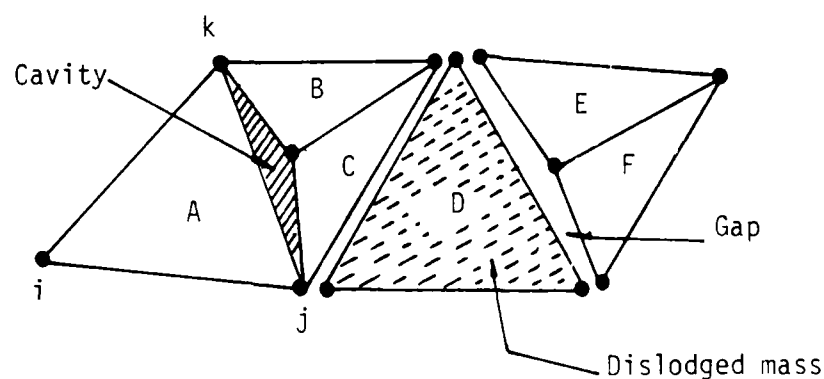
$$\left(\frac{dW}{dA}\right)_\xi > \left(\frac{dW}{dA}\right)_c; \quad \frac{dW}{dV} \approx \left(\frac{dW}{dV}\right)_c, \quad \left(\frac{dV}{dA}\right)_\xi > \left(\frac{dV}{dA}\right)_c \quad (10)$$

The other possibility would be for both  $(dW/dA)_\xi$  and  $dW/dV$  to exceed their critical values at the same time. This would occur when damage occurs at large. Equations (9) and (10) suffice for projectile/target systems where failure is dominated by permanent deformation, fragmentation and fracture including the formation of a plug. Predicted damage patterns are simulated by altering the connectivity of the triangular elements as displayed in Figures 2(a) and 2(b). Regridding is then carried out as further damage occurs within the system. This procedure is continued until the projectile either penetrates through the target or arrest in the target.

Should the condition in equation (9) be met locally over a relatively narrow region such as those shown between elements A and B, C and D and E, F in Figure 2(a), the enclosed material may be regarded as fragmented into small pieces and their masses are redistributed onto the neighboring nodes. The shaded areas are then modelled as cavities. Fragmented sizes are even smaller if the condition  $(dW/dA)_\xi < (dW/dA)_c$  prevails in equation (9) because  $(dV/dA)_\xi$  would then be much smaller than  $(dV/dA)_c$ . When the condition in equation (10) is met by a set of



(a) local fragmentation and mass redistribution



(b) dislodged mass

Figure 2. Change in element connectivity simulating material damage;  
(a) fragmentation and (b) dislodged mass.

constant  $(dW/dA)_{\xi} > (dW/dA)_c$  contours that are narrowly spaced but encircling a relatively large undamaged area, then a block of mass is assumed to be dislodged. No damage is predicted in the detached mass if  $dW/dV < (dW/dV)_c$  while some damage may be present for the case when  $dW/dV \approx (dW/dV)_c$ . The situation just described is shown in Figure 2(b) where the element D is dislodged from its neighboring elements. The element D retains its stiffness and is trapped within the system as damage proceeds. Plugging would be predicted in the same way. The  $(dW/dA)_{\xi} > (dW/dA)_c$  lines would then conform with plug shape in the target. To be emphasized is that  $(dW/dA)_{\xi}$  plays a more dominant role in material fracturing into block masses while  $dW/dV$  in material failure by fragmentation.

#### METHOD OF SOLUTION: FINITE ELEMENT

The projectile/target system is discretized by subdividing both of the contacting solids into a finite number of subdomains or elements in the form of triangles that are interconnected by nodes. A typical triangular element, say A in Figures 2(a) or 2(b), will contain nodes i, j and k referred to in a counterclockwise direction. The coordinates of each node are located in the xy-domain such that attention is focused on analyzing the kinematics of the individual elements. A stiffness matrix containing the properties of both the projectile and target is obtained for relating the accelerations of each element to the dynamic forces via the nodal points. The incremental strains are then found from the incremental displacements. As mentioned before, no a priori assumption is made on the form of the constitutive relations. What needs to be known is only the initial material behavior for the first load increment which is taken to be sufficiently small such that all elements are assumed to respond in the same way. Deviations in the dynamic stress and strain behavior from element to element are accounted for thereafter. There is no restriction on the rate of local strain which can be



as high as  $10^4$  or  $10^6 \text{ sec}^{-1}$  depending on velocity at which the projectile impacts the target.

*Nodal Displacements.* Referring to a rectangular Cartesian coordinate system  $(x,y)$ , the displacement vector  $\{u\}$  possesses the components  $u_x$  and  $u_y$  and it takes the form

$$\{u\} = \begin{Bmatrix} u_x \\ u_y \end{Bmatrix} \quad (11)$$

In the case of triangular elements, the displacement is a linear function of the space variables:

$$\{u\} = \{\alpha_1\} + \{\alpha_2\}x + \{\alpha_3\}y \quad (12)$$

in which  $\{\alpha_1\}$ ,  $\{\alpha_2\}$  and  $\{\alpha_3\}$  are column vectors. It is convenient to express the displacements in terms of those at nodal points  $\{u^e\}$  by making use of the interpolation function  $[N]$ , i.e.,

$$\{u\} = [N]\{u^e\} \quad (13)$$

In equation (13), the nodal point displacement vector is

$$\{u^e\} = \{u_x^i, u_y^i, u_x^j, u_y^j, u_x^k, u_y^k\}^T \quad (14)$$

while  $[N]$  stands for

$$[N] = \begin{bmatrix} N_i & 0 & N_j & 0 & N_k & 0 \\ 0 & N_i & 0 & N_j & 0 & N_k \end{bmatrix} \quad (15)$$

The components  $N_i$  are given by

$$N_i = \frac{1}{2\Delta} (a_i + b_i x + c_i y) \quad (16)$$

with  $\Delta$  being the area of the triangular element  $i, j$  and  $k$ , i.e.,

$$\Delta = \frac{1}{2} \det \begin{vmatrix} 1, x_i, y_i \\ 1, x_j, y_j \\ 1, x_k, y_k \end{vmatrix} \quad (17)$$

The parameters  $a_i, b_i$  and  $c_i$  are

$$a_i = x_j y_k - x_k y_j, \quad b_i = y_j - y_k, \quad c_i = x_k - x_j \quad (18)$$

Once  $\{u\}$  or  $\{u^e\}$  is known, the strains follow immediately from the strain/displacement relations.

*Incremental Strain.* Let  $\{\epsilon\}$  denote the strain tensor referred to the components  $\epsilon_x, \epsilon_y$  and  $\gamma_{xy}$ , i.e.,

$$\{\epsilon\} = \begin{Bmatrix} \epsilon_x \\ \epsilon_y \\ \gamma_{xy} \end{Bmatrix} \quad (19)$$

If  $\{\epsilon\}$  stands for the strain at time  $t$ , then the strain increment in the time interval  $\Delta t$  can be written as

$$\{\Delta\epsilon\}_{\Delta t} = \{\epsilon\}_t - \{\epsilon\}_{t-\Delta t} \quad (20)$$

A zero initial strain field is taken while the strain increment  $\Delta\epsilon$  can be obtained from  $\Delta u$  as

$$\{\Delta \epsilon\} = \begin{Bmatrix} \Delta \epsilon_x \\ \Delta \epsilon_y \\ \Delta \gamma_{xy} \end{Bmatrix} = \begin{Bmatrix} \frac{\partial(\Delta u_x)}{\partial x} \\ \frac{\partial(\Delta u_y)}{\partial y} \\ \frac{\partial(\Delta u_y)}{\partial x} + \frac{\partial(\Delta u_x)}{\partial y} \end{Bmatrix} \quad (21)$$

In terms of the displacement increments at the nodal points, equation (21) becomes

$$\{\Delta \epsilon\} = [B]\{\Delta u^e\} \quad (22)$$

where

$$\{\Delta u^e\} = \{\Delta u_x^i, \Delta u_y^i, \Delta u_x^j, \Delta u_y^j, \Delta u_x^k, \Delta u_y^k\}^T \quad (23)$$

The matrix  $[B]$  is defined by

$$[B] = \begin{bmatrix} \frac{\partial}{\partial x} & 0 \\ 0 & \frac{\partial}{\partial y} \\ \frac{\partial}{\partial y} & \frac{\partial}{\partial x} \end{bmatrix} \begin{bmatrix} N_i & 0 & N_j & 0 & N_k & 0 \\ 0 & N_i & 0 & N_j & 0 & N_k \end{bmatrix} \quad (24)$$

This completes the preliminaries on expressions associated with strain increments.

*Equivalent Uniaxial Stress State.* One of the unique features of the energy density theory lies in the translation of uniaxial data to multi-axial stress or strain states without loss in generality\*. This is accomplished via the con-

\*The plasticity theory assumes the coincidence of the uniaxial data with the effective stress and strain curve which tends to ignore the effects of dilatation that are by no means negligible in the projectile/target damage process.

cept of a damage plane on which the energy transferred across a unit surface area is the same in all directions. In two dimensions, such a plane is defined by  $[(dV/dA)_\xi, \varepsilon_\xi]$  or  $[(dV/dA)_\eta, \varepsilon_\eta]$  which is related to the uniaxial data  $[(dV/dA)_0, \varepsilon_0]$ . In view of equation (2), the stress components  $\sigma_\xi$  and  $\sigma_\eta$  are obtainable as

$$\sigma_\xi = \int \lambda \left( \frac{dV}{dA} \right)_\xi d\varepsilon_\xi, \quad \sigma_\eta = \int \lambda \left( \frac{dV}{dA} \right)_\eta d\varepsilon_\eta \quad (25)$$

Hence, the association of  $\sigma_\xi$  with  $\varepsilon_\xi$  or  $\sigma_\eta$  with  $\varepsilon_\eta$  may be regarded as the equivalent uniaxial stress and strain relation because they refer to an unique volume energy density<sup>\*</sup>

$$\frac{dW}{dV} = \int \sigma_\xi d\varepsilon_\xi \text{ or } \int \sigma_\eta d\varepsilon_\eta \quad (26)$$

which is the equivalent of equation (1).

In retrospect, it can be concluded from equations (8) and the condition  $(dV/dA)_\xi = (dV/dA)_\eta$  that  $\varepsilon_\xi$  equals to  $\varepsilon_\eta$  on the damage plane. Equation (26) thus follows. The equivalence<sup>\*\*</sup> of  $\varepsilon_\xi$  and  $\varepsilon_\eta$ , however, is not a necessary condition in the energy density theory. It will no longer hold when the expressions of  $(dV/dA)_\xi$  and  $(dV/dA)_\eta$  in equations (8) are altered to include nonlinear and/or

<sup>\*</sup> The expression  $dW/dV = \int \sigma_{ij} d\varepsilon_{ij}$  used in nonlinear elasticity or plasticity invokes the independence of load sequence on stored energy. This, of course, is a restriction that cannot be justified in any theories involving irrecoverable energy dissipation.

<sup>\*\*</sup> This should not be confused with the plane of principal strain. Such a relation occurred by chance as a result of the neglect of nonlinear and/or shear stress effects in equations (8).

shear stress effects. What is relevant is the unique determination of  $dW/dV$  from  $\sigma_{\xi}$  and  $\epsilon_{\xi}$  or  $\sigma_{\eta}$  and  $\epsilon_{\eta}$ . The functional relationships of the two pairs of normal stress and normal strain may or may not be the same but they must be uniquely defined on the damage plane.

The procedure for constructing the dynamic stress and strain history of a typical element becomes straightforward after the damage plane or the angle  $\alpha$  is determined from the condition  $\epsilon_{\xi} = \epsilon_{\eta}$  or other equivalent relations that may involve  $\epsilon_{\xi}$ ,  $\epsilon_{\eta}$  and  $\gamma_{\xi\eta}$  depending on the forms of  $(dV/dA)_i$  ( $i = \xi, \eta$ ). Using the base material property for the first load increment, the damage plane  $\alpha_1$  is obtained from which  $(\epsilon_{\xi})_1$  and  $(dV/dA)_1$  can be found. This locates the point  $p_1$  as shown in Figure 3. The following load step leads to  $\alpha_2$  and hence the point  $p_2$  involving  $(\epsilon_{\xi})_2$  and  $(dV/dA)_2$ . In this way, a series of points  $p_1, p_2$ , etc., can be obtained to yield the actual response\* of each element whose strain rate is determined rather than preassigned as in the classical approach. Unloading can be carried out incrementally by the same procedure. The corresponding shear stresses\*\*  $(\tau_{\xi\eta})_1, (\tau_{\xi\eta})_2$ , etc., can be calculated from the equations of motion:

$$\begin{aligned} \frac{\partial \sigma_{\xi}}{\partial \xi} + \frac{\partial \tau_{\xi\eta}}{\partial \eta} &= \rho \frac{\partial^2 u_{\xi}}{\partial t^2} \\ \frac{\partial \tau_{\xi\eta}}{\partial \xi} + \frac{\partial \sigma_{\eta}}{\partial \eta} &= \rho \frac{\partial^2 u_{\eta}}{\partial t^2} \end{aligned} \quad (27)$$

\* The stress and strain response of any element does not follow any preassigned data in the computer data bank which is provided only for the convenience of numerical computation.

\*\* There is no need to assume a separate shear stress and shear strain relation as in the classical theory of elasticity. The energy density theory requires only a knowledge of  $dV/dA$  which is associated with the slope of the stress and strain curve.

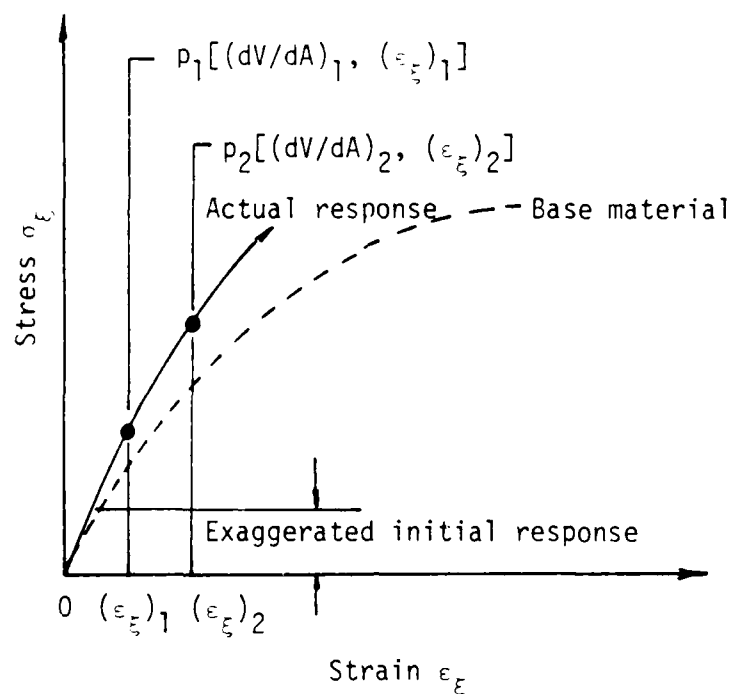


Figure 3. Schematic of actual stress and strain response of a typical element.

in which  $\rho$  is the mass density of the local element that may vary from location to location in the projectile/target problem. Since the mechanical properties in each element will vary, the classically defined wave velocities are no longer applicable in the energy density theory.

*Dependency of Surface and Body Forces.* In order to simulate the traction conditions at the projectile/target contact surface, it is necessary to obtain the nodal forces in terms of the stresses within the elements. Let these forces be denoted as

$$\{F^e\} = \{F_x^i, F_y^i, F_x^j, F_y^j, F_x^k, F_y^k\}^T \quad (28)$$

They will act on the nodes with lump masses obtained from the element. The prin-

ciple of virtual work will be applied to assure that the nodes are in dynamic equilibrium. Consider an arbitrary nodal virtual displacement  $\delta u^e$  such that it is consistent with the mechanical constraint. It follows that

$$\int_V \{\delta \epsilon\}^T \{\sigma\} dV - \int_A \{\delta u\}^T \{T\}^n dA - \{\delta u^e\} \{F^e\} = 0 \quad (29)$$

in which  $\{T\}^n$  is the traction vector with normal  $n$  and  $\delta \epsilon$  is the virtual strain associated with the virtual displacement  $\delta u$ . Making use of equations (13) and (22) in the forms

$$\{\delta u\}^T = \{\delta u^e\}^T [N]^T \quad (30)$$

and

$$\{\delta \epsilon\}^T = \{\delta u^e\}^T [B]^T \quad (31)$$

equation (29) may be rearranged to read as

$$\{F^e\} + \int_A [N]^T \{T\}^n dA = \int_V [B]^T \{\sigma\} dV \quad (32)$$

This is the fundamental equation to be programmed in the finite element formulation. Further simplification of the volume integral in equation (32) can be made in view of the fact that both  $[B]$  and  $\{\sigma\}$  are constant over the triangular element. For a unit thickness, it is obvious that

$$\int_V [B]^T \{\sigma\} dV = 0.5 [B]^T \{\sigma\} \quad (33)$$

The evaluation of the surface integral involves averaging the tractions between two nodes and summing the results.

Unlike the classical approaches where the effect of  $dV/dA$  is neglected, the surface tractions and body or inertia forces are no longer independent in the energy density theory. This effect is particularly significant at the interface where the projectile comes in contact with the target. The condition to be satisfied is

$$T_i^n = \sigma_{ji} n_j + \rho \frac{\partial^2 u_i}{\partial t^2} \left( \frac{dV}{dA} \right)_n, \quad i = \xi, \eta \quad (34)$$

with  $n_j$  being the components of the unit normal vector. The term involving the acceleration and the rate change of volume with surface area is of the same order of magnitude as the surface tractions and stresses. The neglect of  $(dV/dA)_n$  in equation (34) is the reason why the classical continuum mechanics theories are not able to accurately account for the transmission of energy and/or traction from the projectile to the target or vice versa.

*Sliding Contact Surface.* As the projectile comes into contact with the target, sliding of the adjacent surfaces is permitted and will be implemented in the finite element formulation following the technique presented in [3]. This necessitates the specification of the relative nodal displacements or the nodal coordinates  $\{x^e\}$ . To this end, let the mass of an element be evenly distributed at the three nodal points on which the nodal forces in equation (32) are applied. The accelerations at these nodes may be obtained as

$$\{\ddot{u}^e\}_t = \frac{\{F^e\}_t}{M^e} \quad (35)$$



where  $M^e$  stands for the lumped mass at the eth node. The velocity vector can thus be found by integrating equation (35). Assuming that the acceleration is constant for a small time increment  $\Delta t$ , then

$$\{\dot{u}^e\}_{t+} = \{\dot{u}^e\}_{t-} + \{\ddot{u}^e\}_t \overline{\Delta t} \quad (36)$$

Referring to Figure 4,  $\{\dot{u}^e\}_{t+}$  and  $\{\dot{u}^e\}_{t-}$  are the velocities just after and before the current time  $t$  and  $\overline{\Delta t}$  stands for the average time increment about  $t$ , i.e.,

$$\overline{\Delta t} = \frac{(\Delta t)_{t-} + (\Delta t)_{t+}}{2} \quad (37)$$

At incipient impact  $t = 0$ ,  $\{\dot{u}^e\}_{t-}$  are the initial velocities of those nodes in the projectile which come in contact with the target such that  $\{\ddot{u}^e\}_t = 0$  for  $(\Delta t)_{t-}$ . Assuming that the velocities are constant over the time increment  $\Delta t$ , equation (36) can be integrated to yield the nodal displacements

$$\{u^e\}_{t+\Delta t} = \{u^e\}_t + \{\dot{u}^e\}_t \cdot (\Delta t)_{t+} \quad (38)$$

where

$$\{\Delta u^e\} = \{\dot{u}^e\}_t \cdot (\Delta t)_{t+} \quad (39)$$

is, in fact, the incremental displacement. The nodal coordinates are then obtained from the displacements:

$$\{x^e\}_{t+\Delta t} = \{x^e\}_t + \{u^e\}_{t+\Delta t} \quad (40)$$

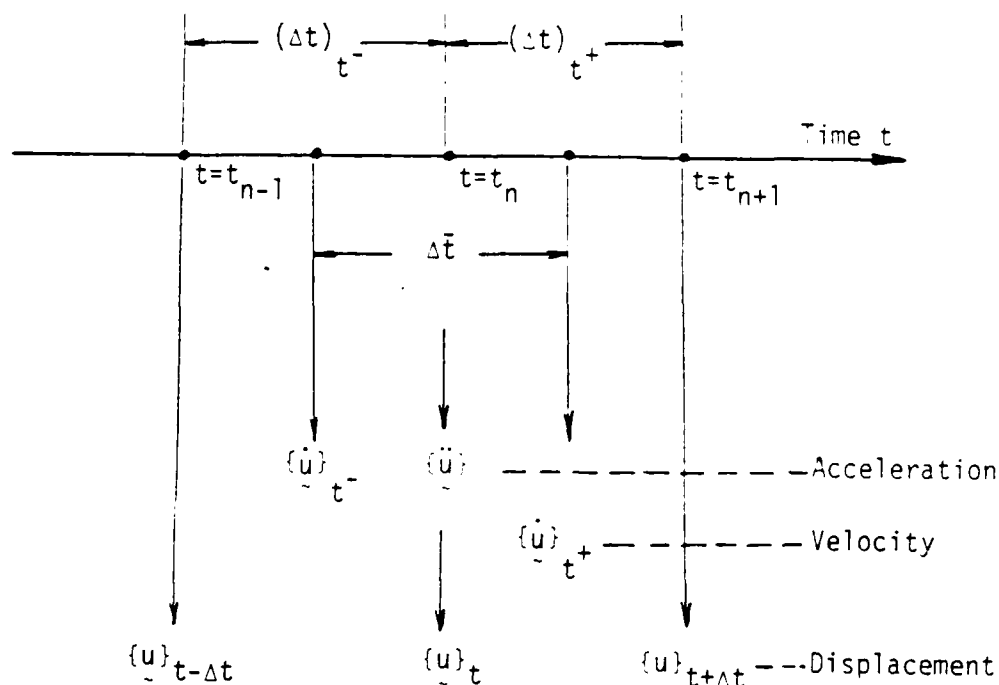


Figure 4. Time sequence of displacement, velocity and acceleration.

To reiterate, the nodal velocities are calculated at the mid-point of the time interval which represents the average velocities during the time increment  $\Delta t$ . The nodal displacements and accelerations are defined at the beginning or the end of the time increment. Sliding of the projectile and target interface enables the readjustment of the nodal displacements, velocities and accelerations as a result of the interchange of momentum and kinetic energy between the projectile and target.

*Regriidding.* Because of the complex nature of the projectile/target failure pattern that changes for each time increment, the finite element grid requires readjustment as the system undergoes damage. This procedure is labor-intensive and depends on the experience of the analyst who must be familiar with the theory of energy density; particularly, in grasping the concept of exchange of surface and volume energy. Discussed below are some of the adjustments that must be con-

sidered during remeshing of the finite element grid pattern.

As the material between the projectile and target is highly compressed, there is a tendency for the local density to increase. This can be simulated by judicious redistribution of the nodal masses. Since the projectile also suffers damage in the form of fragmentation, its mass will alter giving rise to change of the projectile momentum and velocity. These considerations together with those outlined in equations (9) and (10) are sufficient for analyzing the progressive damage of the projectile/target system.

#### COMPUTER PROGRAM

The computer program consists of three main portions. They are referred to as INIXY, PSEDA and PLTXY. Table 1 shows the flow chart for INIXY that deals with the initial input data on material properties, grid generation for the projectile/target system and the relevant parameters that are required for carrying out the failure analysis. The chart in Table 2 gives an overall view of PSEDA that incorporates the strain energy density theory for evaluating the damage and failure of all elements. Sliding nodes are introduced at the interface where projectile comes into contact with the target in order to ensure displacement compatibility and to avoid overlapping or interpenetration of material points. The damage and failure pattern for each time increment can be exhibited graphically via the PLTXY routine shown in Table 3. Contours of constant  $dW/dV$  and  $dW/dA$  can also be plotted such that equations (9) and/or (10) can be applied to determine the failure pattern and the information on regriding for the next time increment. The time increment  $\Delta t$  is chosen according to the interaction of dynamic disturbance with the finite element mesh size. If  $\delta_{min}$  denotes the minimum dimension of the triangular element, then the time increment should be chosen to be smaller than the

Table 1. Flow chart of INIXY: preprocessing.

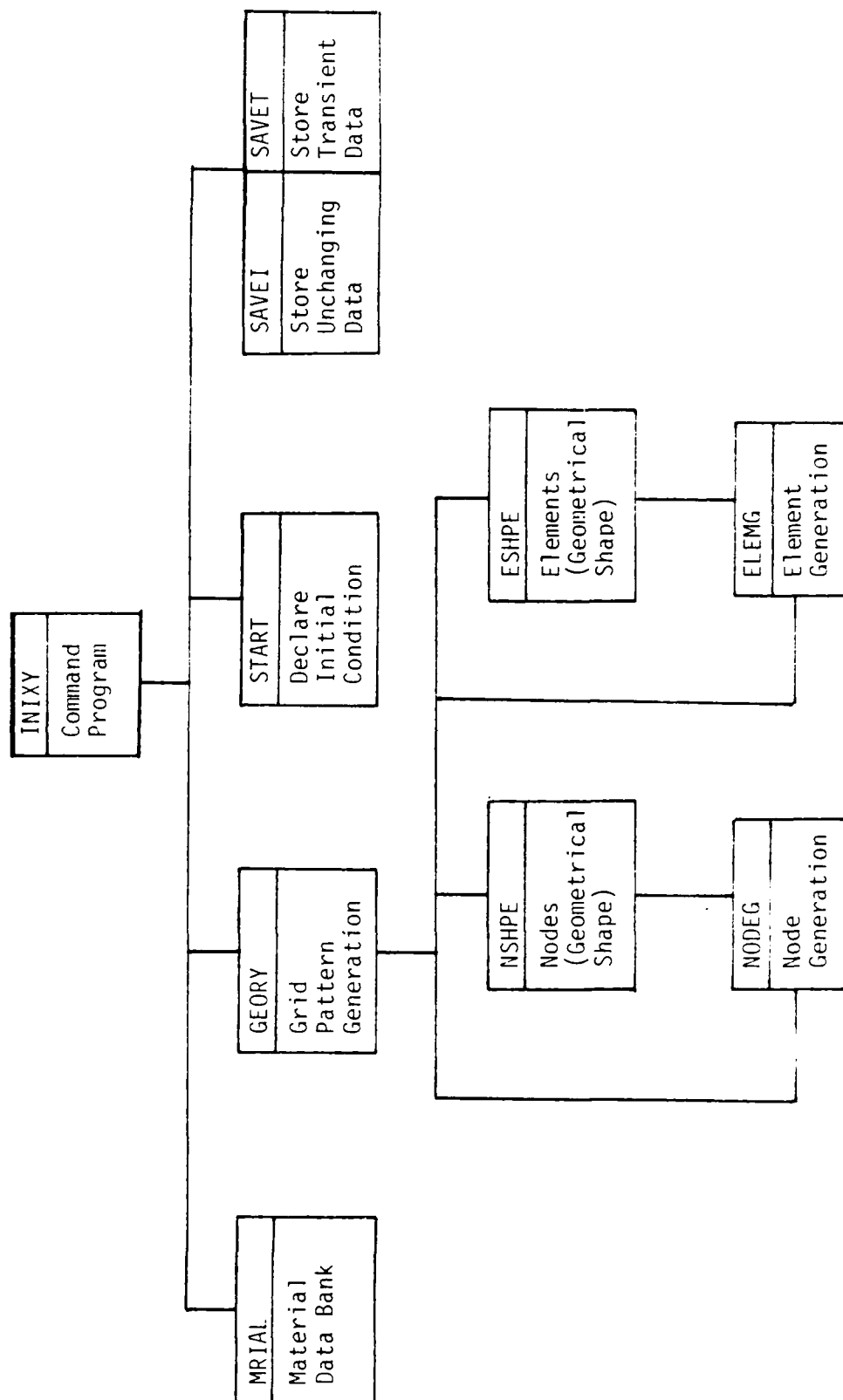


Table 2. Flow chart of PSEDA: failure analysis.

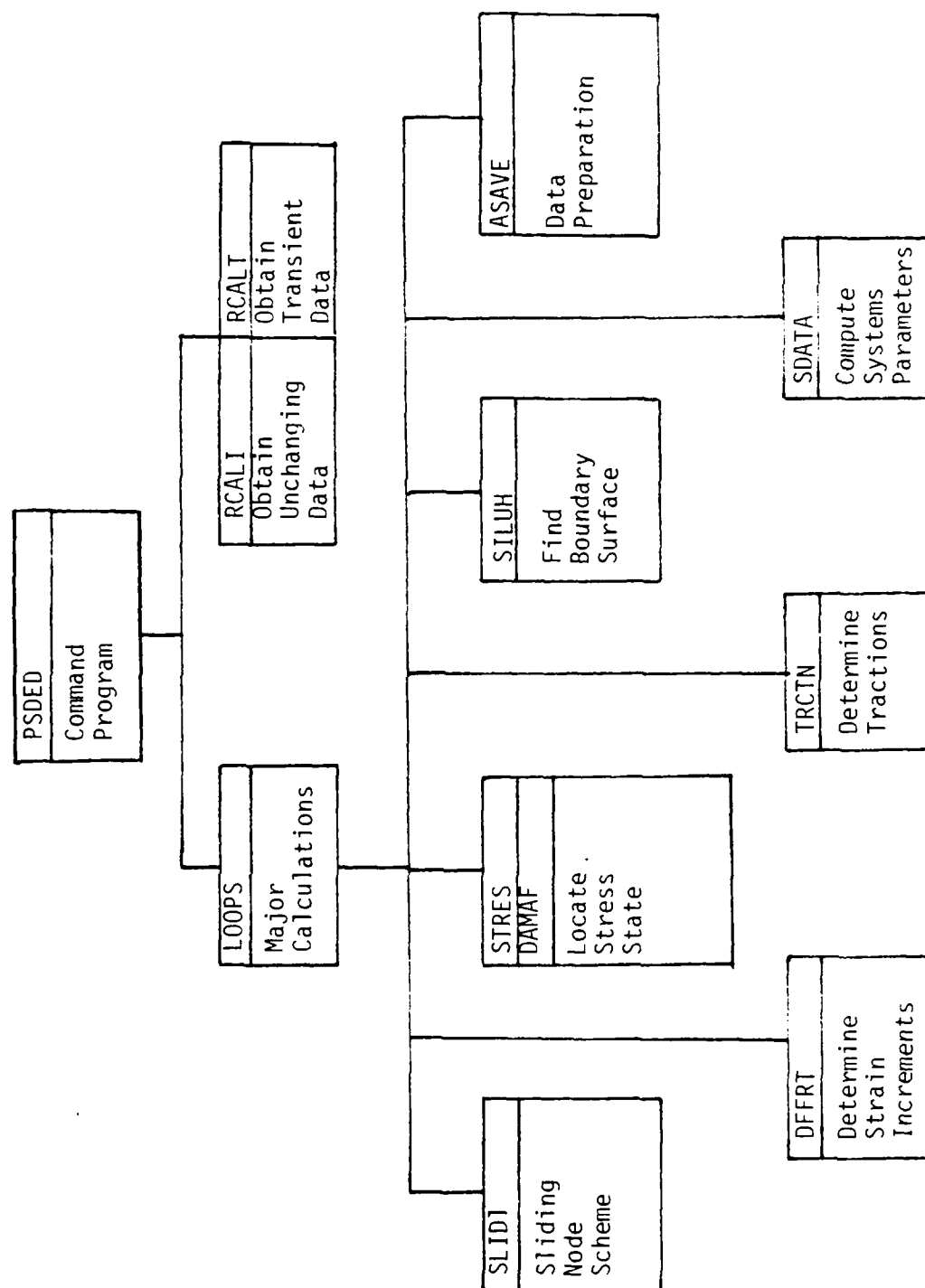
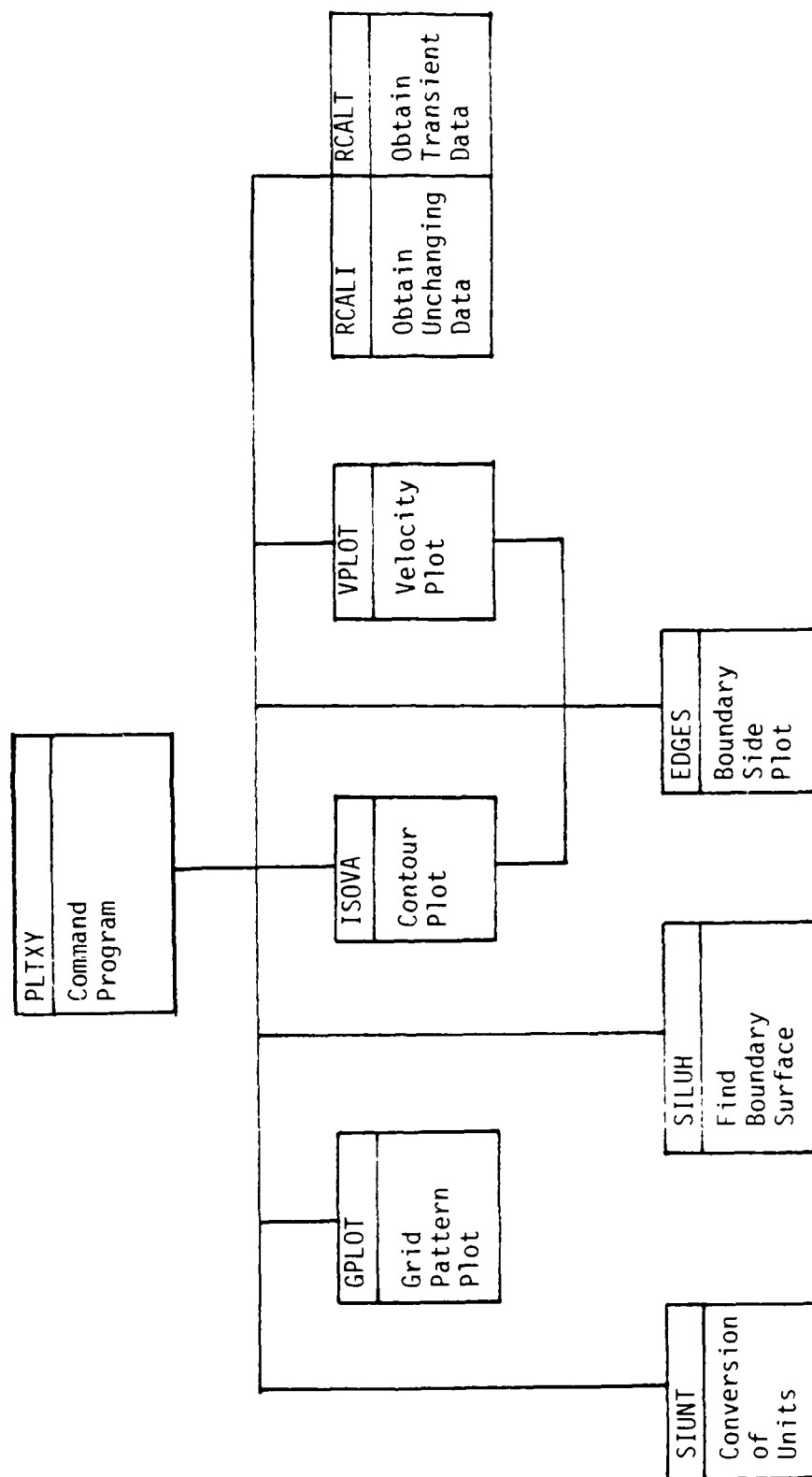


Table 3. Flow chart of PLTXY: postprocessing.



time required for the dynamic disturbance to travel across  $\delta_{\min}$ , i.e.,

$$\Delta t < \text{Min} \left( \frac{\delta_{\min}}{\delta_0} \right) \quad (41)$$

where  $\delta_0$  is a normalizing length parameter. The accuracy of the predictions can be improved by reducing the mesh size and the time increment. This increases the labor of regriding and computer time in addition to the readjustments that must be made on mass redistribution and momentum change. Refer to Tables 4, 5 and 6 for a more detailed account of the computing procedures involving INIXY, PSEDA and PLTXY.

#### IMPACT OF PROJECTILE ON TARGET PLATE

The computer program described previously will be referred to as the Plane Strain Energy Density Analysis (PSEDA) code and it will be applied to solve the problem of a projectile impacting a target plate. Analyzed will be the sequence of damage pattern as the projectile penetrates through the target in an incremental manner without making any assumptions on the failure modes and the local strain rates. The material data bank has the capacity of covering strain rates from  $10^{-4}$  to  $10^6 \text{ sec}^{-1}$  which is more than adequate for the example to be considered.

*System Geometry.* A tungsten projectile with dimensions  $D_p = 1.4 \text{ cm}$  and  $L_p = 4.7 \text{ cm}$  is traveling at a velocity of 1,200 m/sec and comes into normal contact with a plate with dimensions  $h_t = 2 \text{ cm}$  and  $D_t = 10 \text{ cm}$  as illustrated in Figure 5. Because of symmetry, only one-half of the problem needs to be discretized by application of triangular elements. The initial grid pattern is displayed in Figure 6 in which 64 elements and 52 nodes are employed. Smaller elements are de-

Table 4. Block diagram for computing algorithm of INIXY.

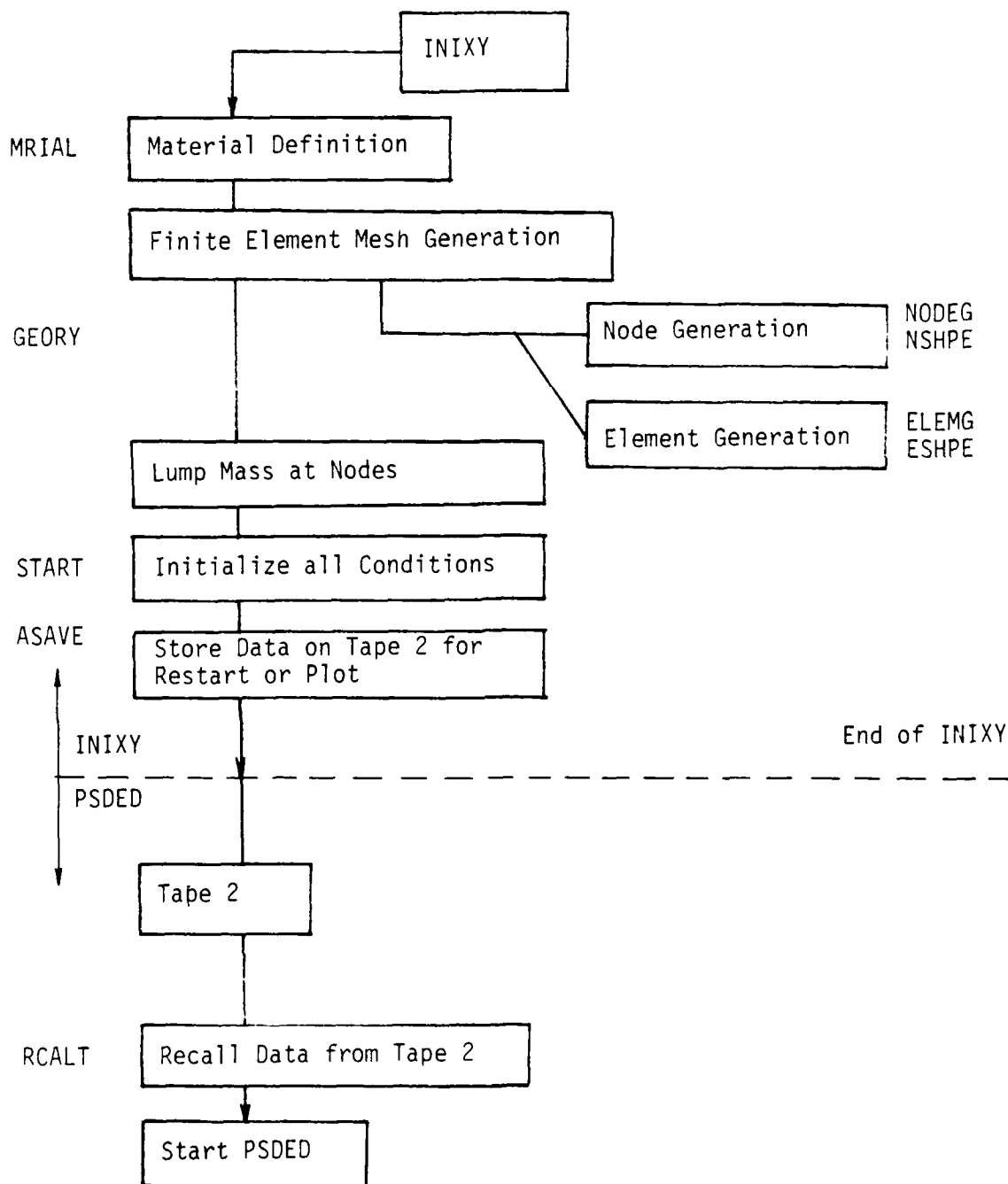




Table 5. Block diagram for computing algorithm of PSEDA.

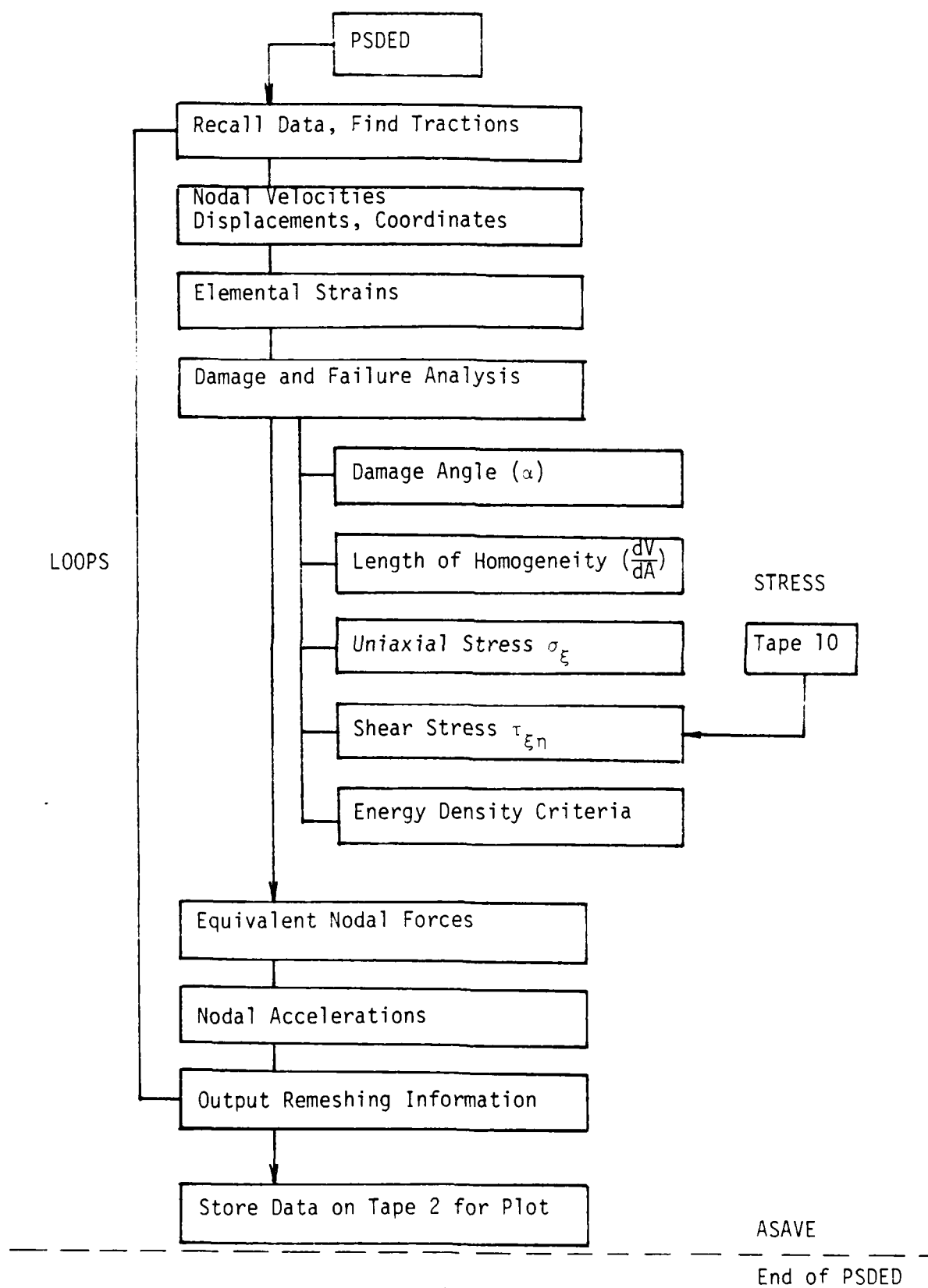
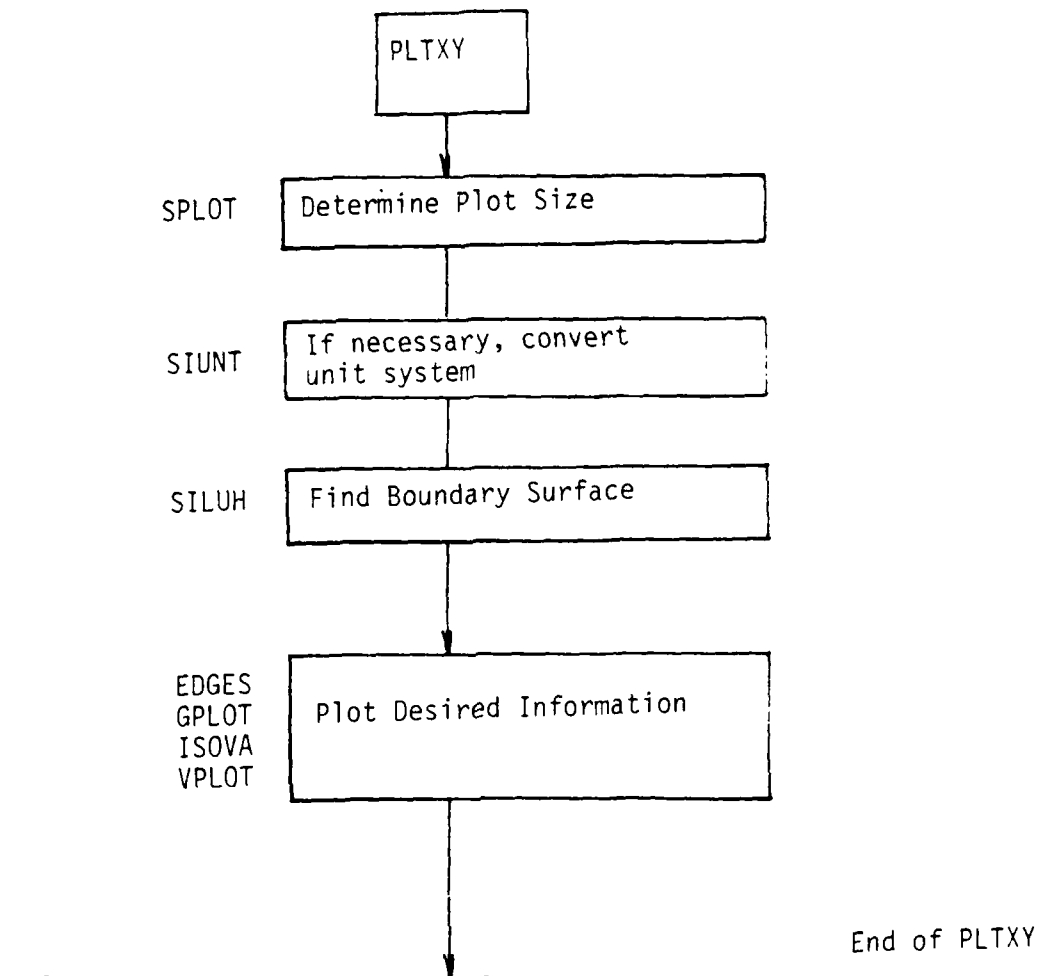


Table 6. Block diagram for computing algorithm of PLTX.



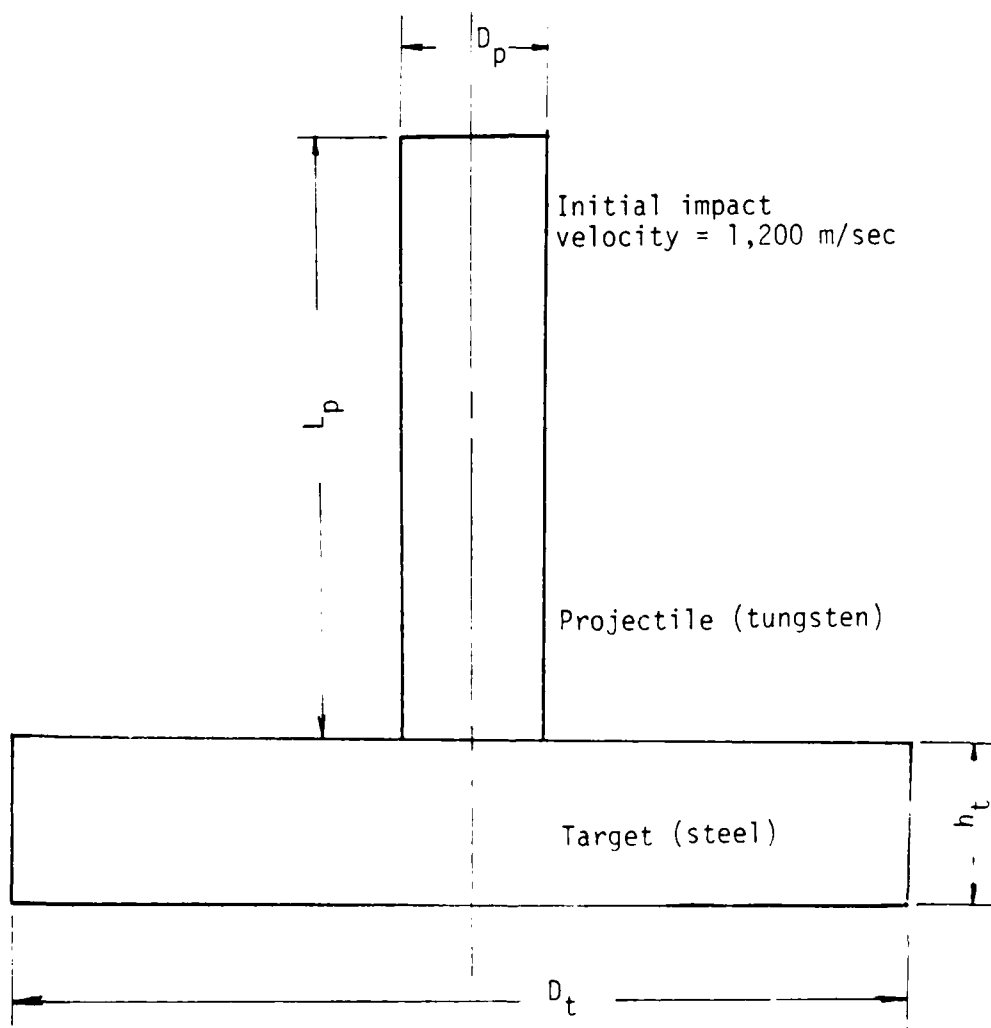


Figure 5. Schematic of projectile/target system under normal impact.

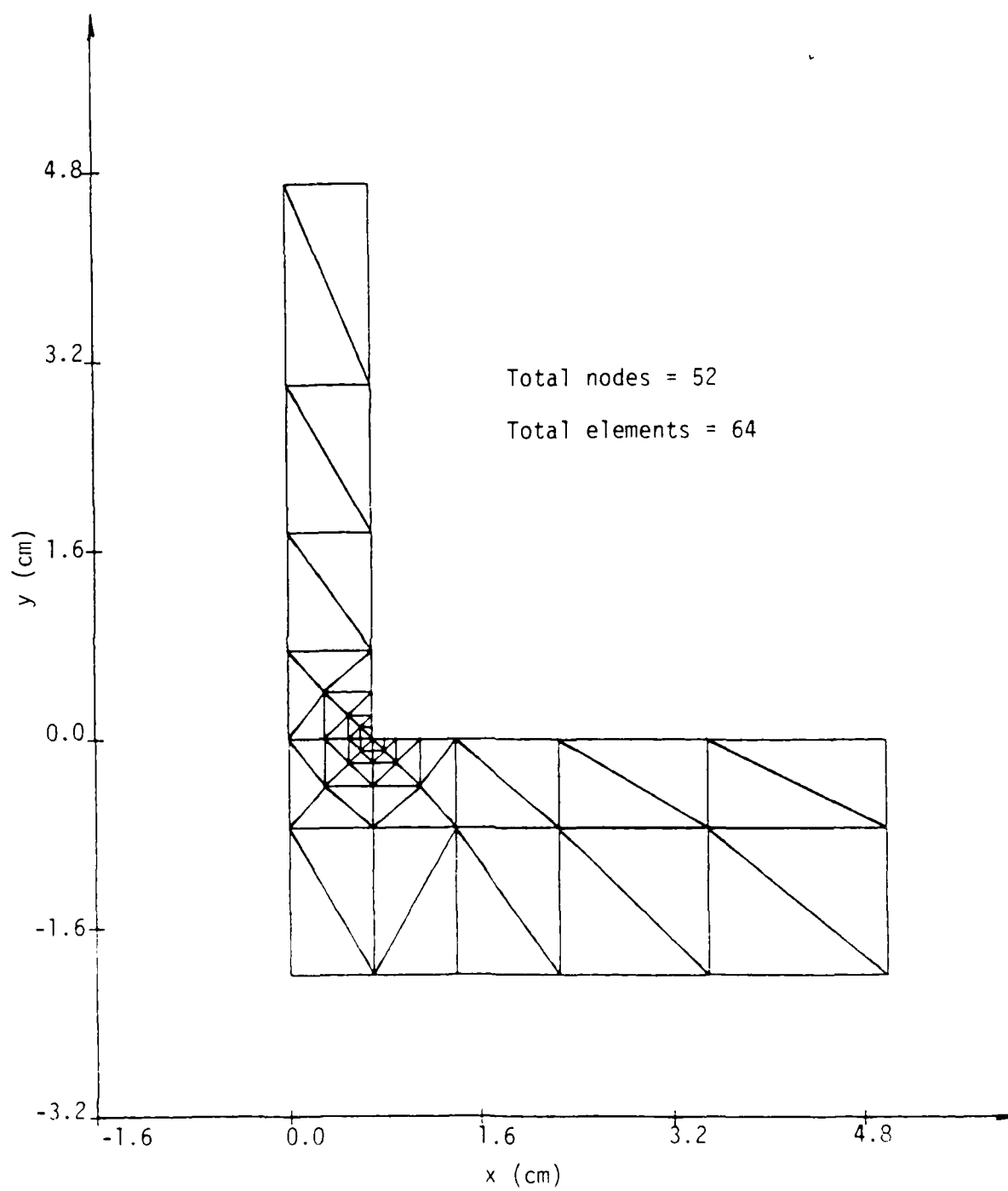


Figure 6. Initial grid pattern of projectile/target system.

picted near the contacting end with a reentrant-corner where the stress and energy are concentrated and failure is most likely to initiate. The locations of each element and node are referenced to the x- and y-coordinate. An enlarged view of the region near the contact end is given in Figure 7 which also provides information on the numbering of the nodes and elements. As damage proceeds, the grid pattern in Figure 6 will be modified accordingly.

*Base Material.* Under normal strain rates, say  $10^{-3}$  or  $10^{-4}$   $\text{sec}^{-1}$ , the stress and strain response of most metals will first rise sharply and then level off until fracture occurs at  $f$  in Figure 8 at which point the uniaxial test terminates. Such a behavior, however, will not be valid for all points in the projectile/target system after the initial impact because the local strain rates will not only be higher but they will vary from one location to another. Therefore, the base material property can be used only during the early onset of impact.

As a reference, Table 7 gives the conventional mechanical properties of the tungsten projectile and the 4340 steel target plate. The symbols  $E$ ,  $\epsilon_{ys}$  and  $\epsilon_f$  stand, respectively, for the Young's modulus, yield strain and final strain. The coefficients  $\beta$  and  $\gamma$  correspond to those used in the uniaxial stress and strain relation

$$\sigma = E\epsilon - \beta\epsilon_{ys} \left[ \left( \frac{\epsilon}{\epsilon_{ys}} \right)^{\gamma} - 1 \right] \quad (42)$$

The resulting curves are given in Figure 9. Note that the tungsten has a higher yield strength  $\sigma_{ys}$  and fracture toughness related to  $(dW/dV)_c$  or area under the true stress and true strain curve than the 4340 steel. This is further illustrated in Figure 10 where  $\gamma_{ys}$  tends to drop as  $(dW/dV)_c$  increases for both the projectile and target material. Such a trade-off is well-known for metals and

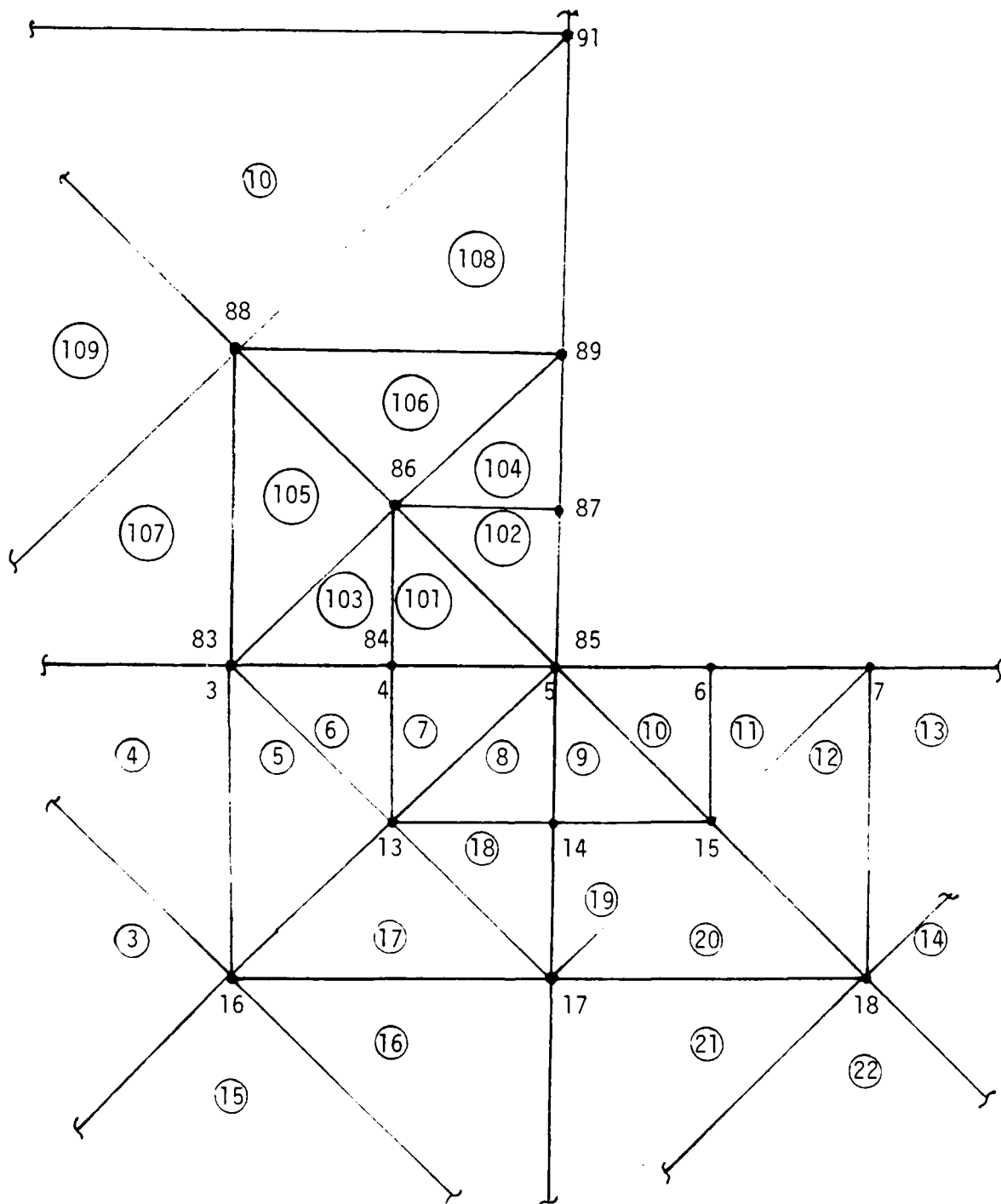


Figure 7. Numbering of nodes and elements near contact area.

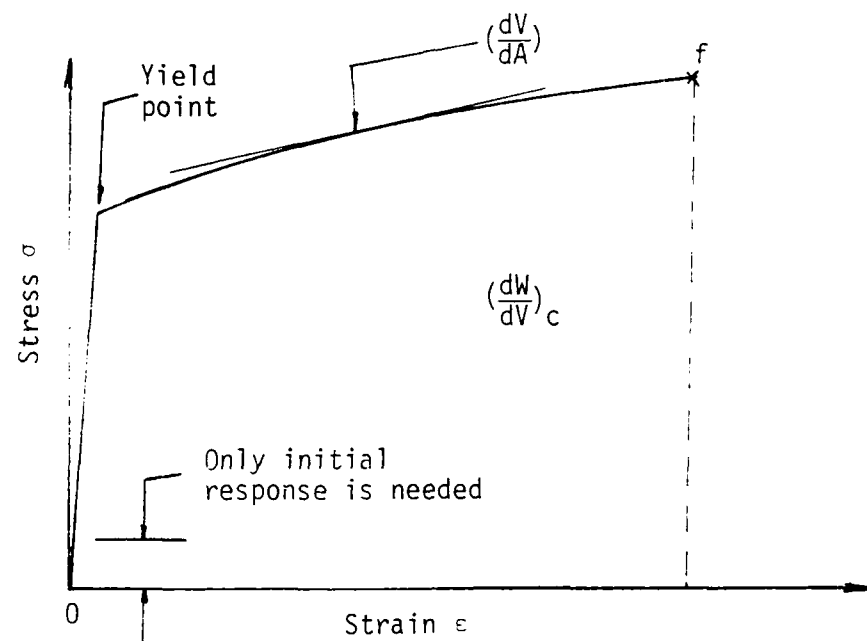


Figure 8. True stress versus true strain curve of base material.

Table 7. Properties of base material for projectile/target system.

	$E \times 10^{11} \text{ (N/m}^2\text{)}$	$\epsilon_y \times 10^{-3}$	$\beta$	$\gamma$	$\epsilon_f$
Projectile	3.450	3.058	0.9702	1.0044	0.1920
Target	2.068	4.691	0.9648	1.0071	0.088

must be considered in order to optimize their performance.

*Discussion of Results.* To start the calculation, all 64 elements in Figure 6 are assumed to respond in the same way while the projectile/target configuration corresponds to that in Figure 11. A number of trial and error runs were made for determining the appropriate choice of the initial and subsequent time steps.

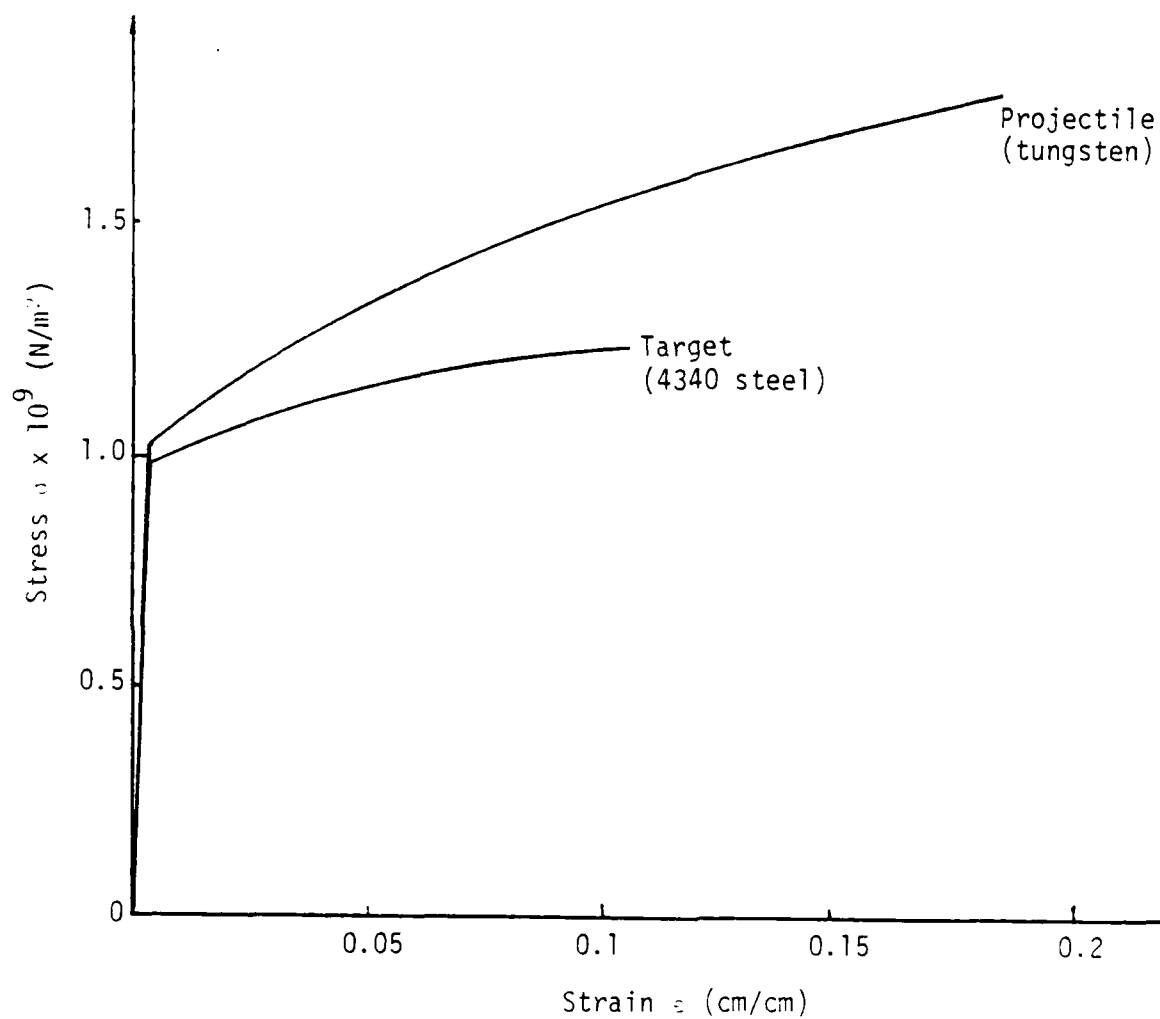


Figure 9. Uniaxial stress and strain relation for projectile and target for low strain rate.



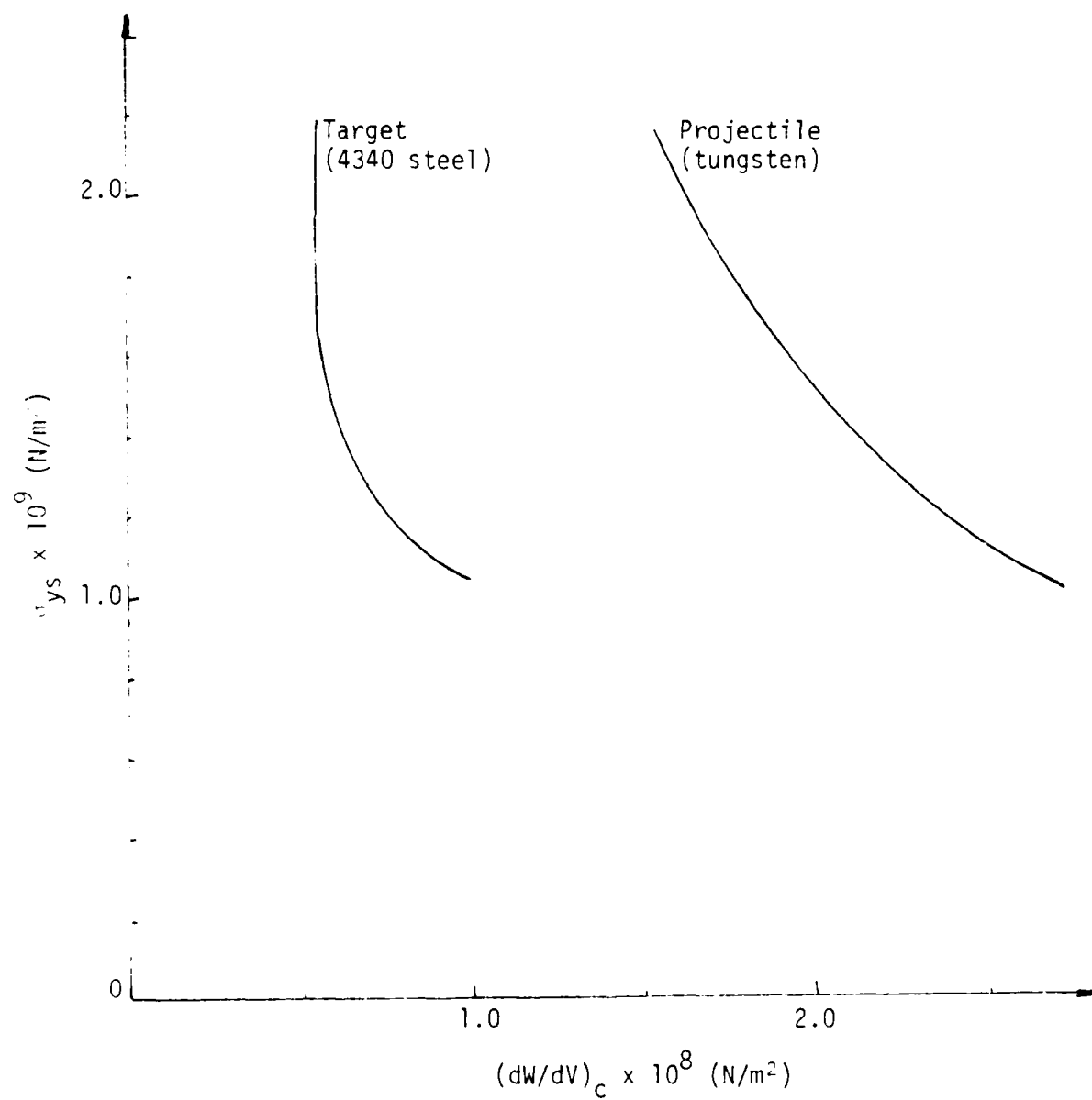


Figure 10. Relation between yield strength and critical strain energy density function for projectile/target system.

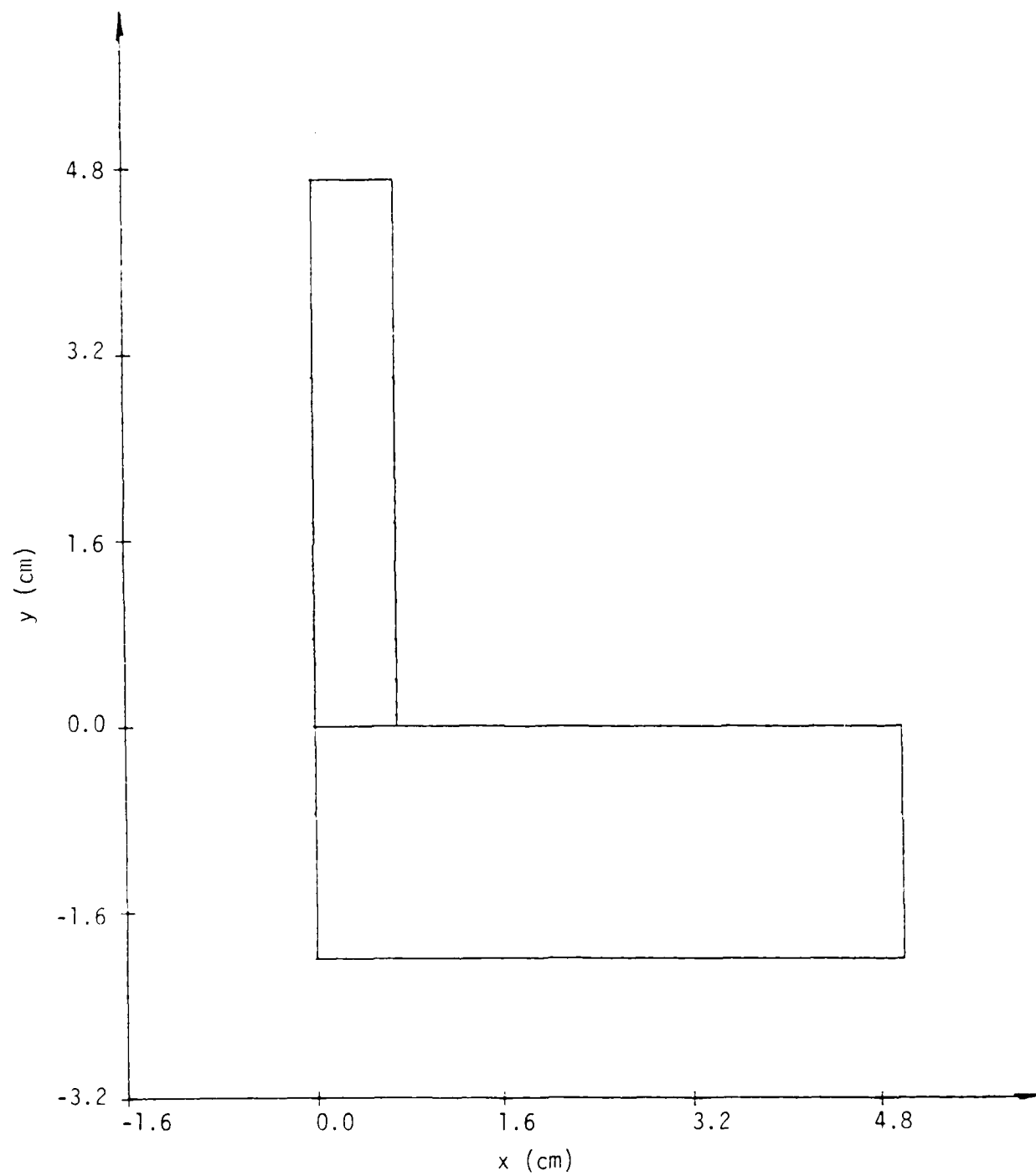


Figure 11. Initial geometry of projectile/target system  
at  $t = 0.0 \mu\text{sec}$ .

There is no formal procedure for optimizing the finite element mesh size with the corresponding time step. Any variance will alter the energy dissipation history or the time dependency of the  $H$ -function\* [11,12] that determines the degree of irreversibility or dissipative character of the projectile/target system. A thorough understanding of the combined influence of mesh size and time step on the damage of a physical system in general, however, is a topic beyond the scope of this investigation.

The contours of  $dW/dA$  on the damage plane and  $dW/dV$  are first obtained for  $t = 0.075 \text{ } \mu\text{sec}$ . They are displayed in Figures 12 and 13. To be kept in mind is that the critical values  $(dW/dA)_c$  and  $(dW/dV)_c$  will change from location to location because the stress and strain response in each element is different. For instance, Figure 12 shows that the intensity  $dW/dA$  for contours no. 1 to no. 4 increases from  $0.86 \times 10^3 \text{ N/m}$  to  $27.95 \times 10^3 \text{ N/m}$ . It is not obvious where failure will first initiate unless the  $(dW/dA)_c$  values at these locations are carefully examined. According to the condition in equation (10), failure by localized spall occurred first at the front surface of the target directly underneath the projectile corner. This justifies the removal of a semi-circular block of material whose boundary coincides with the surface along which  $(dW/dV)_c = 14.88 \times 10^3 \text{ N/m}$ . Even though the  $dW/dA$  values of contours no. 3 and no. 4 are higher, no failure is predicted at these locations because the corresponding  $(dW/dA)_c$  values are higher than  $19.21 \times 10^3 \text{ N/m}$  and  $27.95 \times 10^3 \text{ N/m}$ . Figure 13 shows that the magnitude of the  $dW/dV$  contours remained below the critical value. A corner cavity is thus modelled in the target after a time lapse of  $0.075 \text{ } \mu\text{sec}$ .

---

\* It is analogous to the entropy function in classical thermodynamics when energy is dissipated all in the form of heat. In general,  $H$  acquires a much broader interpretation [11,12] of order and disorder as disturbed by loading and can be either negative or positive.

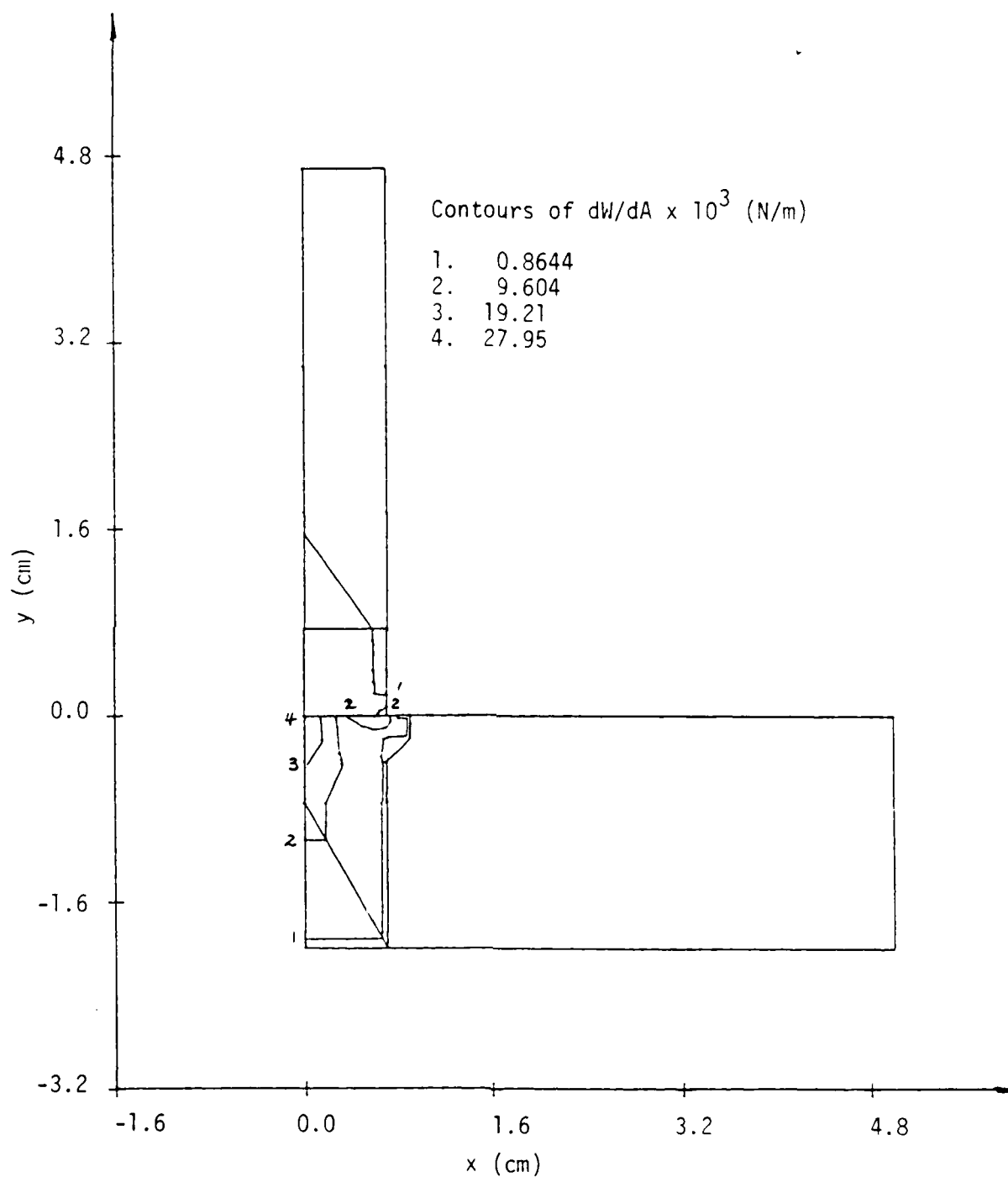


Figure 12. Contours of constant  $dW/dA$  at  $t = 0.075$  .sec.

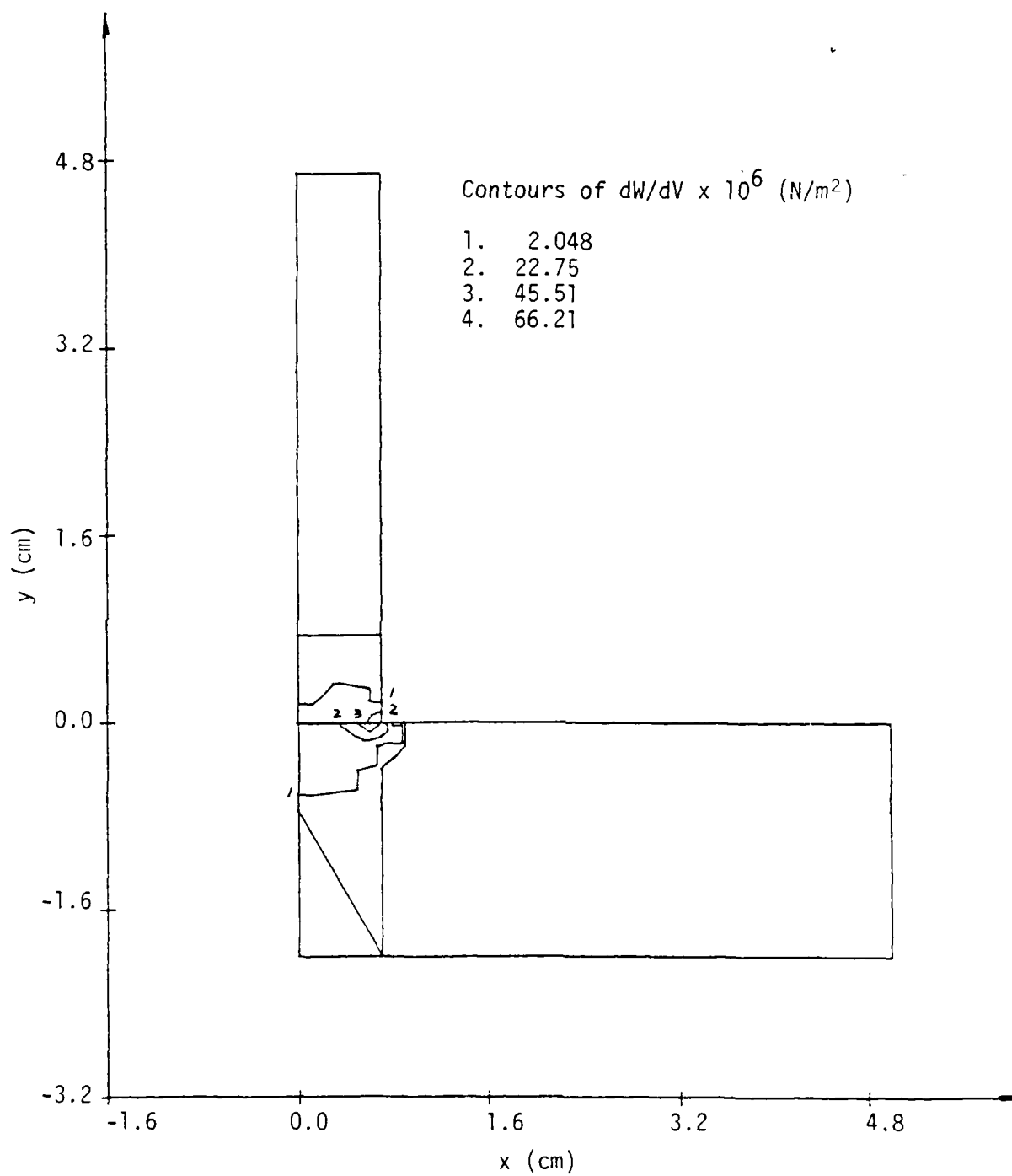


Figure 13. Contours of constant  $dW/dV$  at  $t = 0.075 \mu\text{sec}$ .

Because the cavity is sufficiently small, the same number of 64 elements and 52 nodes can be used for the next time increment except that the elements next to the cavity have been distorted as indicated in Figure 15. Calculations made at  $t = 0.120 \text{ } \mu\text{sec}$  yield another set of  $dW/dA$  and  $dW/dV$  contours and they revealed increasing dynamic disturbances in both the projectile and target as shown in Figures 16 and 17. Again, all  $dW/dV$  contours are below critical while the critical  $(dW/dV)_c = 16.04 \times 10^3 \text{ N/m}$  contour prevailed in a region circling the cavity in Figure 14 or 15. An increase in the cavity size is thus predicted as shown in Figure 18. Remeshing of the finite element grid pattern is carried out in Figure 19 such that the elements around the cavity periphery are made smaller for better accuracy. This results in an increase of element number from 64 to 67 and nodal points from 52 to 56.

As the material in the target under the projectile corner is being removed, energy transmission begins to shift towards the center of the target. For  $t = 0.175 \text{ } \mu\text{sec}$ , the values of  $(dW/dV)_c$  near the target surface under and away from the projectile are, respectively,  $15.53 \times 10^3 \text{ N/m}$  and  $14.88 \times 10^3 \text{ N/m}$ . According to the  $dW/dA$  contours displayed in Figure 20, further fragmentation of the target surface is predicted. The corresponding  $dW/dV$  contours no. 1, 2 and 3 in the same neighborhood are of the order of  $10^7 \text{ N/m}^2$  which is still one order of magnitude lower than the critical value. Surface energy density remains as the dominant cause of failure. Figure 22 shows the fragmented shape of the target surface and the corresponding grid pattern is given in Figure 23. No surface separation has yet occurred within the projectile. Damage continues to occur as  $t$  advances from  $0.175 \text{ } \mu\text{sec}$  to  $0.240 \text{ } \mu\text{sec}$ . The change in the  $dW/dA$  contours is small. This can be seen by comparing the results in Figure 24 with those in Figure 20. Higher values of  $dW/dV$  around the fractured region of the target did

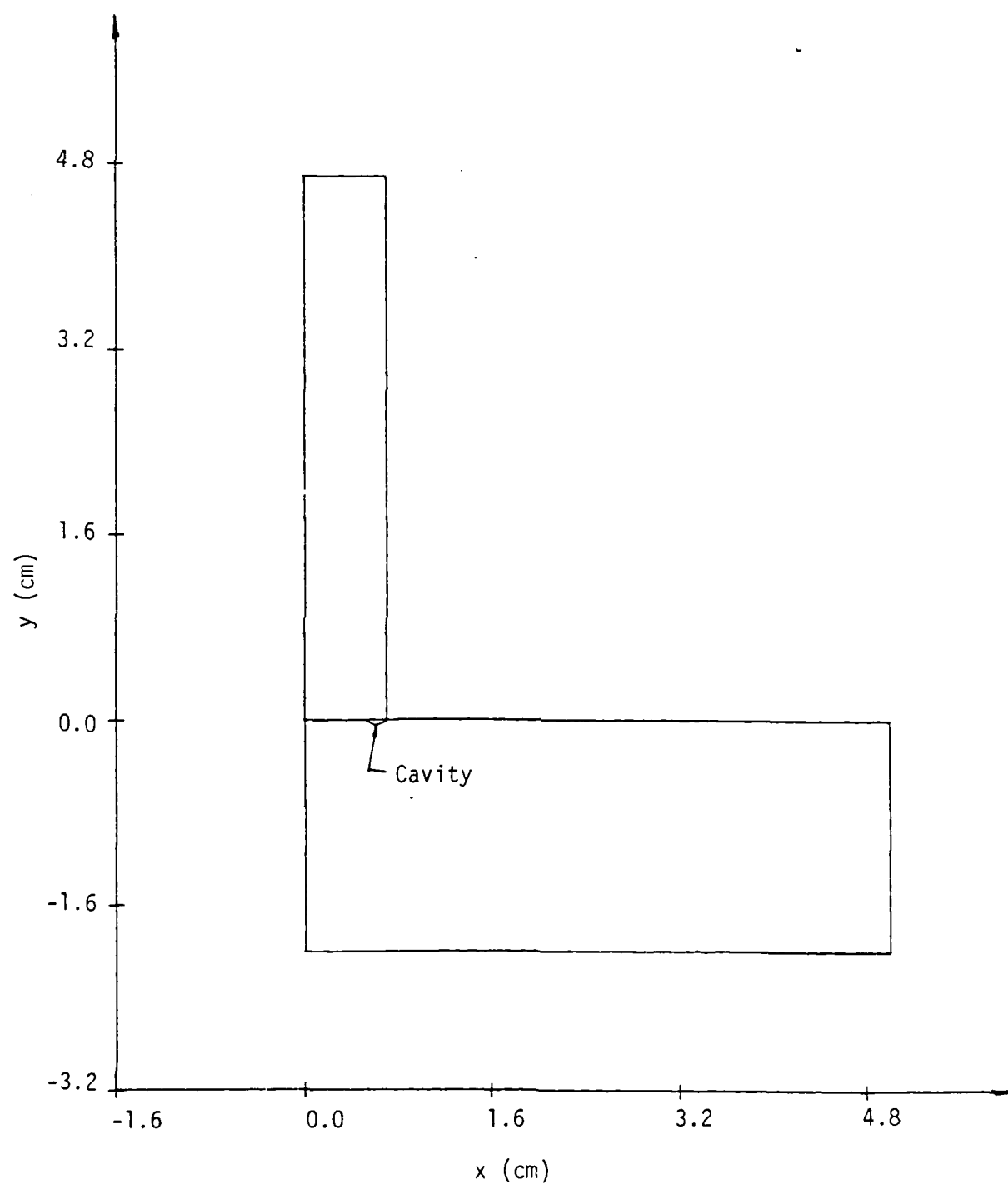


Figure 14. Corner cavity modelled in the target after 0.075  $\mu$ sec.

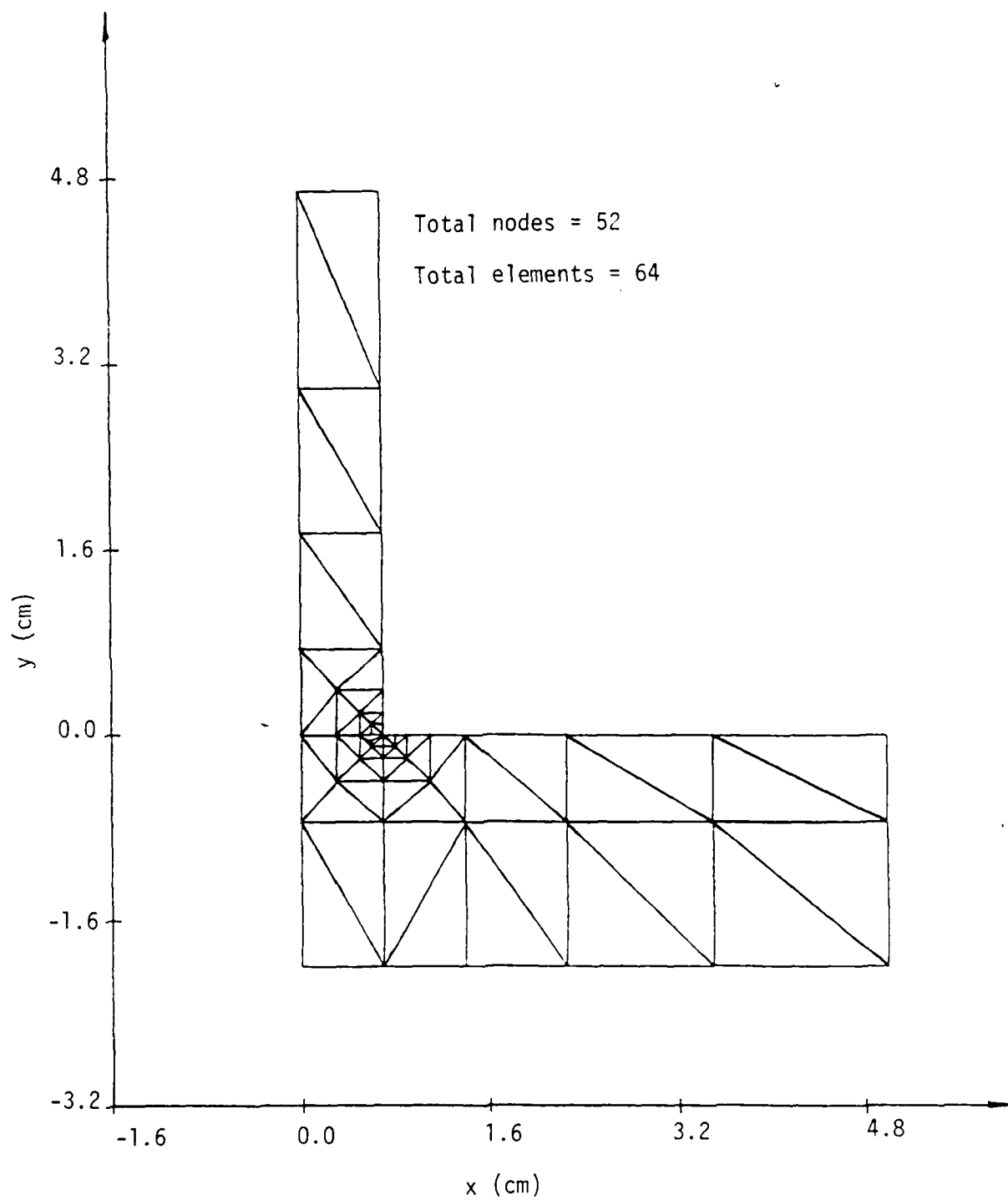


Figure 15. Grid pattern of projectile/target system with a corner cavity.



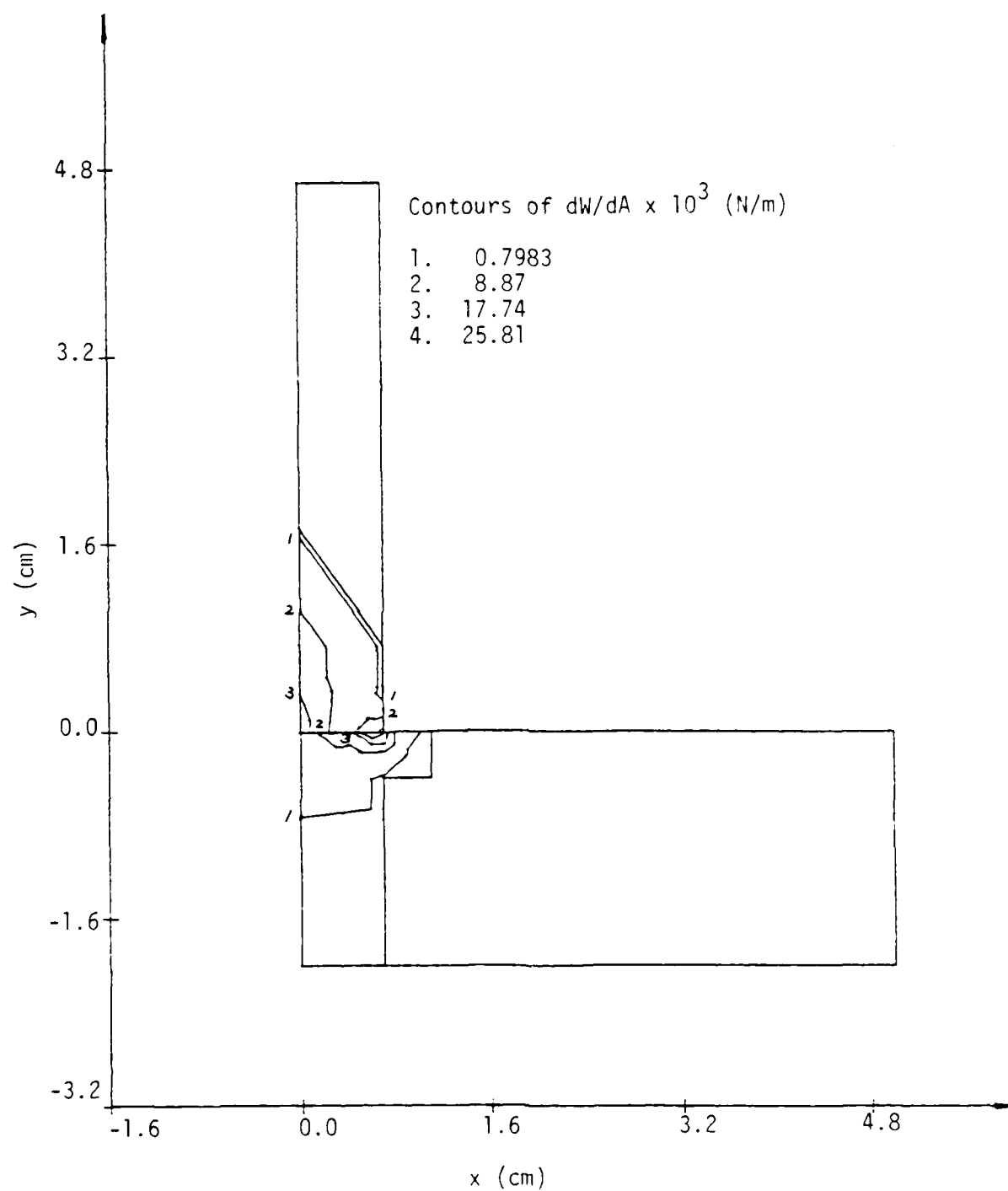


Figure 16. Contours of constant  $dW/dA$  at  $t = 0.120$  sec.

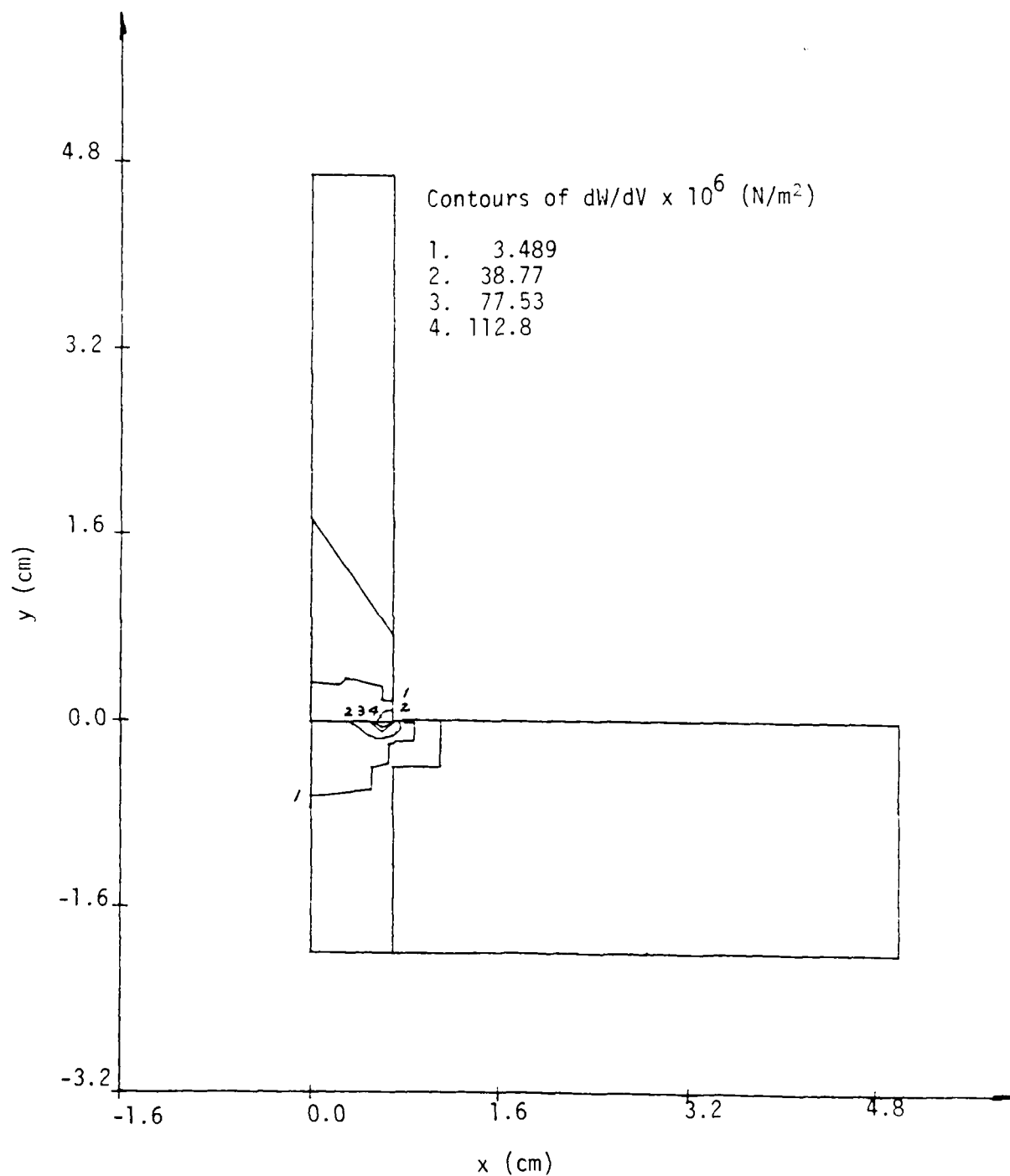


Figure 17. Contours of constant  $dW/dV$  at  $t = 0.120 \mu\text{sec}$ .

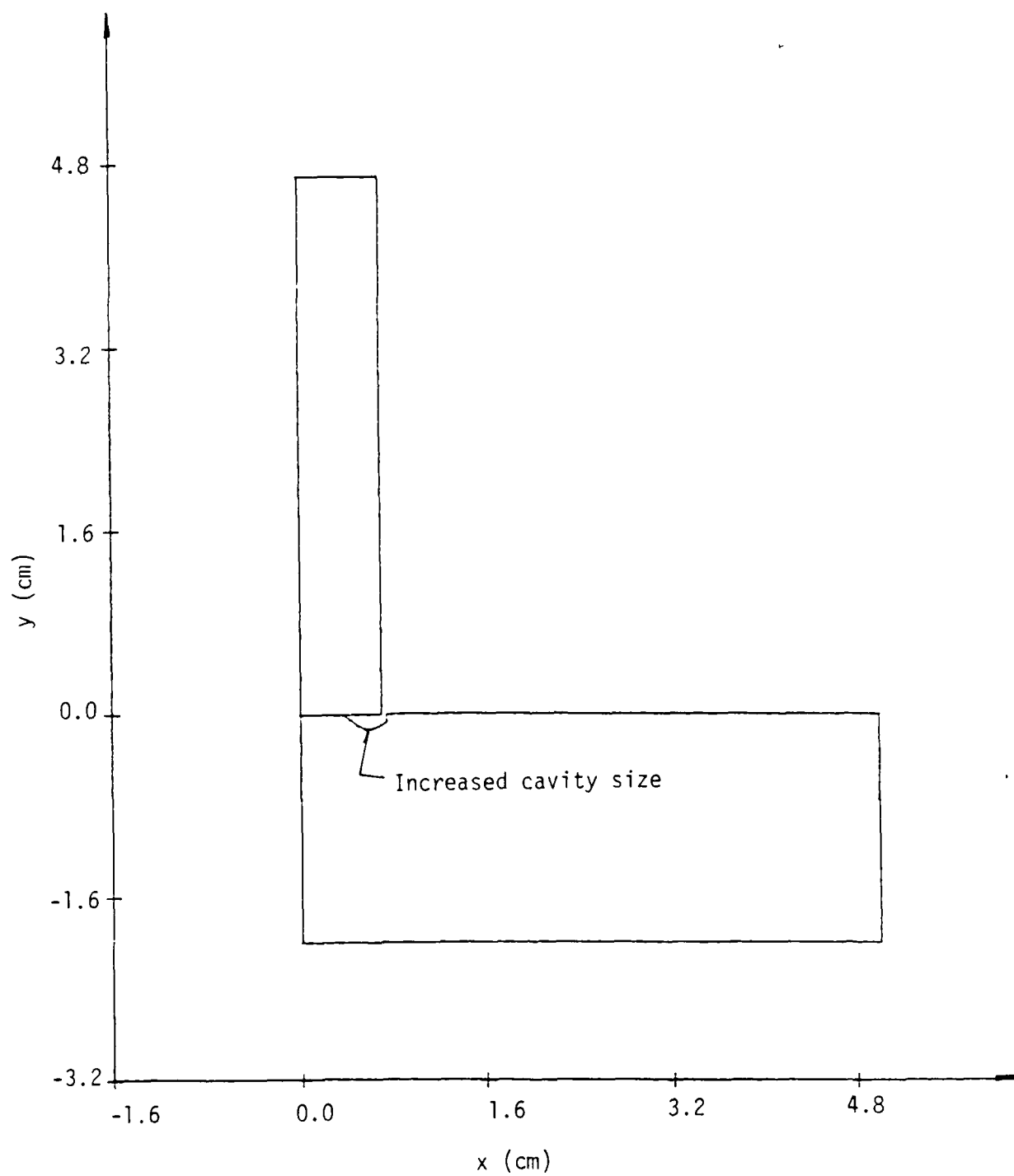


Figure 18. Increase size of local cavity in target as time increases to 0.120  $\mu\text{sec}$ .

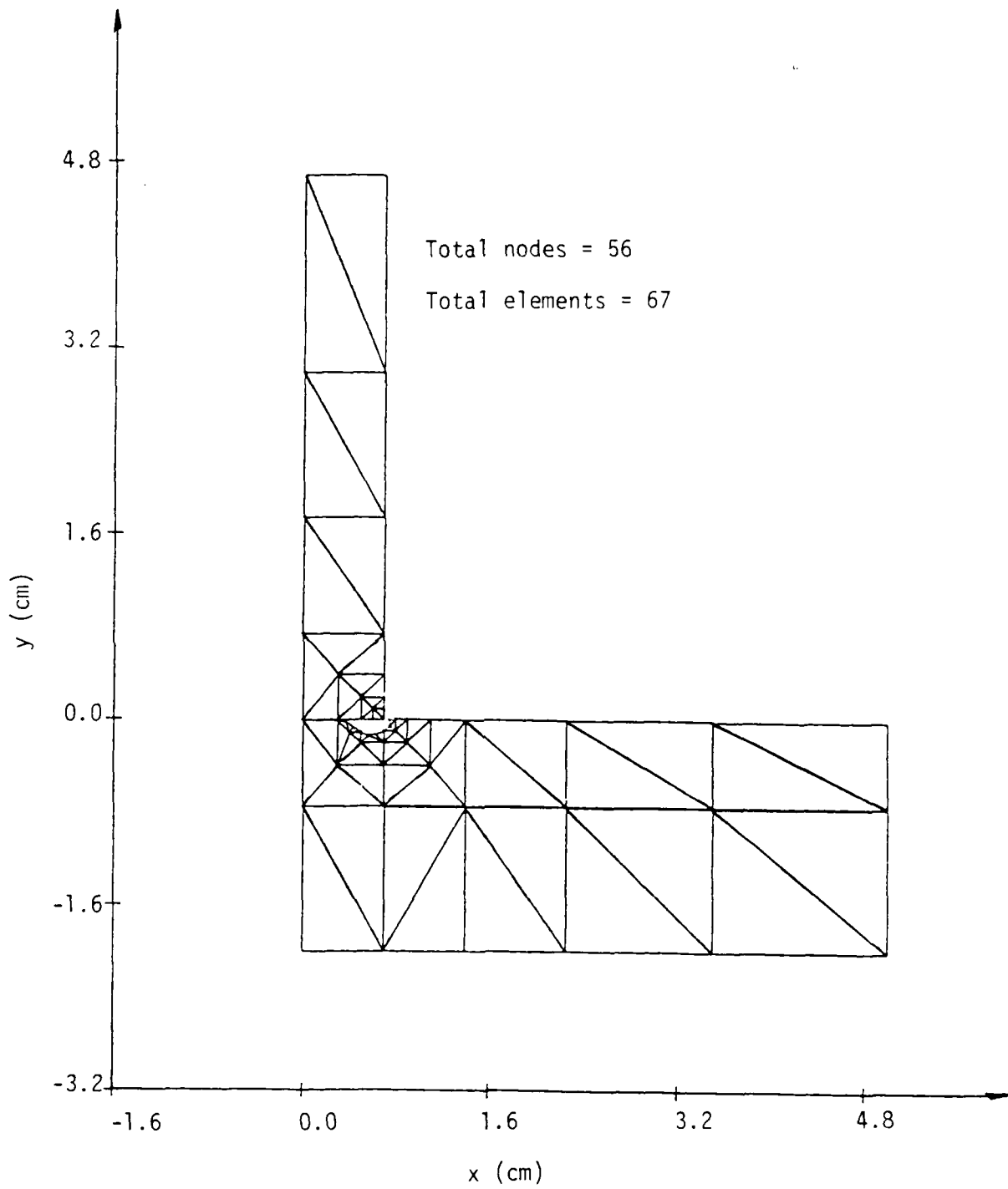


Figure 19. Remeshed grid pattern after 0.120 msec.

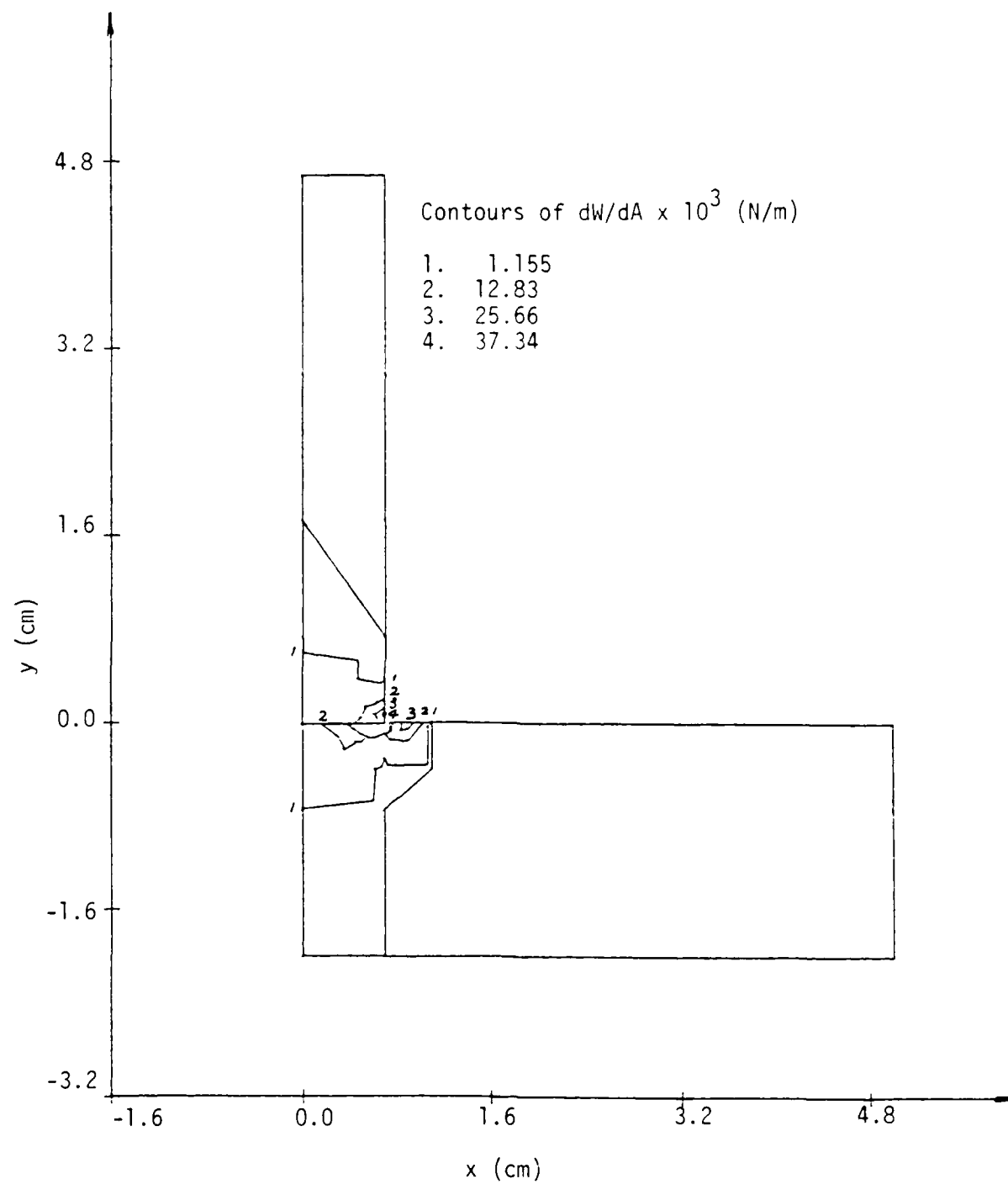


Figure 20. Contours of constant  $dW/dA$  at  $t = 0.175$  usec.

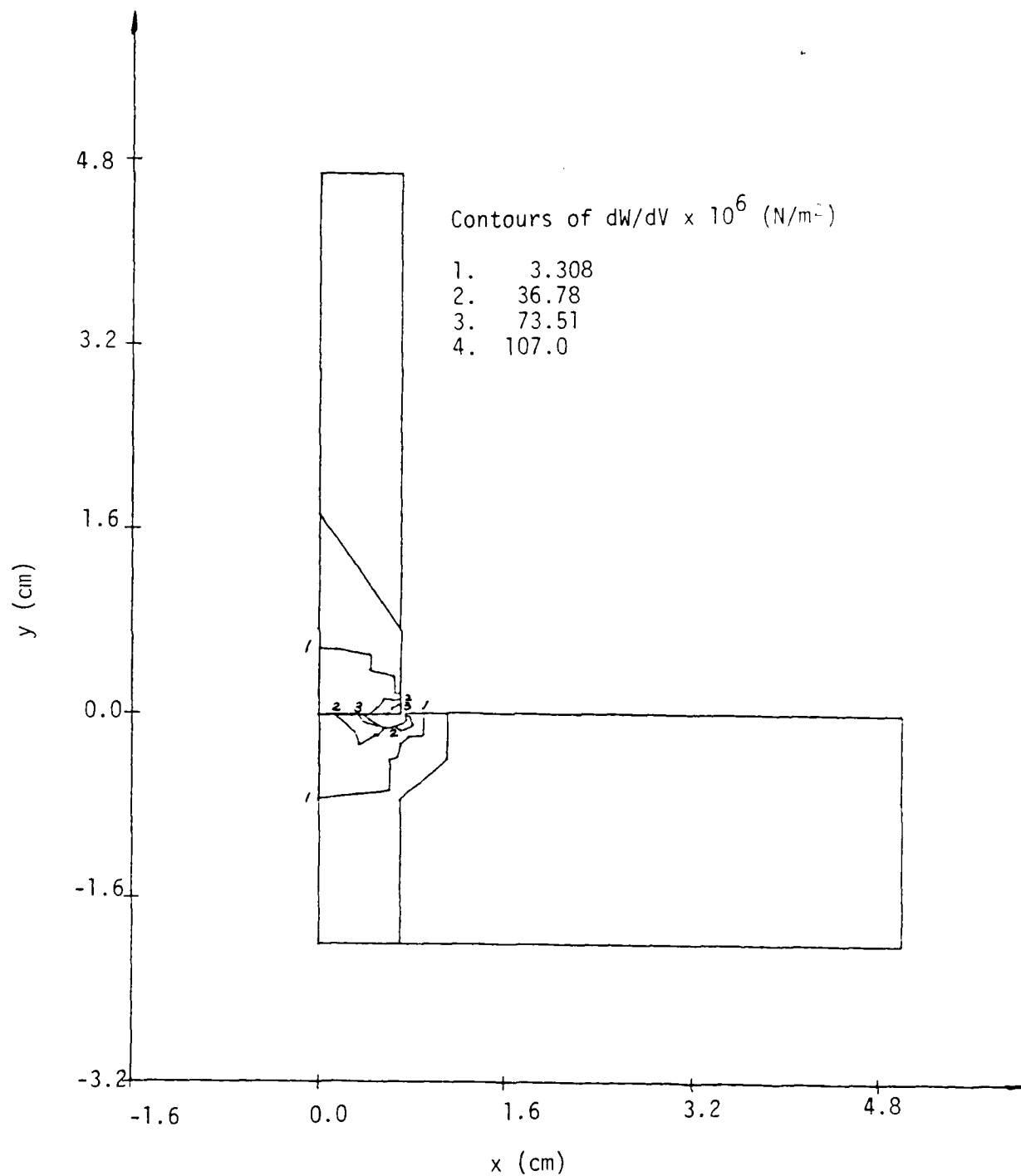


Figure 21. Contours of constant  $dW/dV$  at  $t = 0.175$  usec.

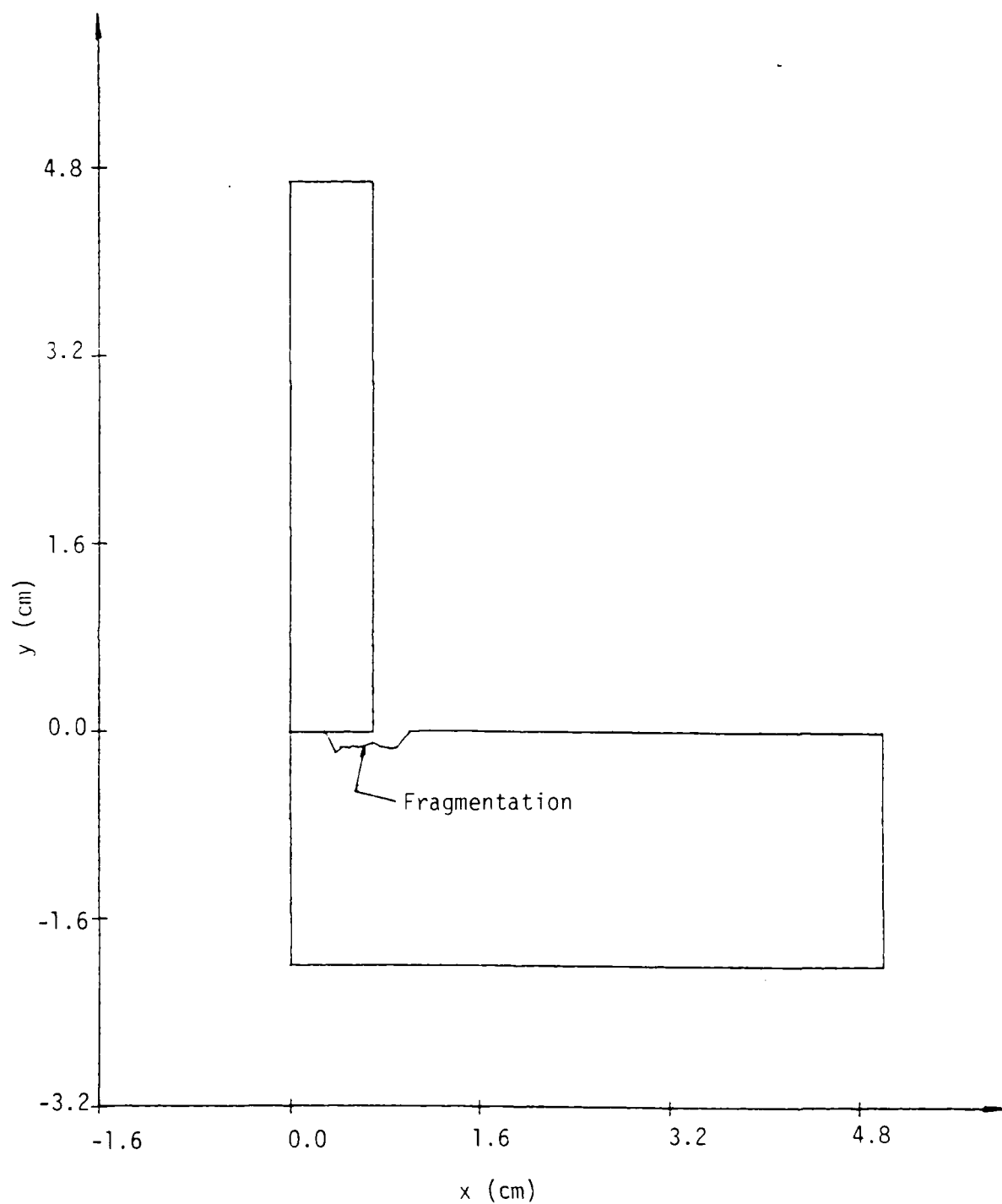


Figure 22. Fragmented target surface after 0.175  $\mu\text{sec}$ .

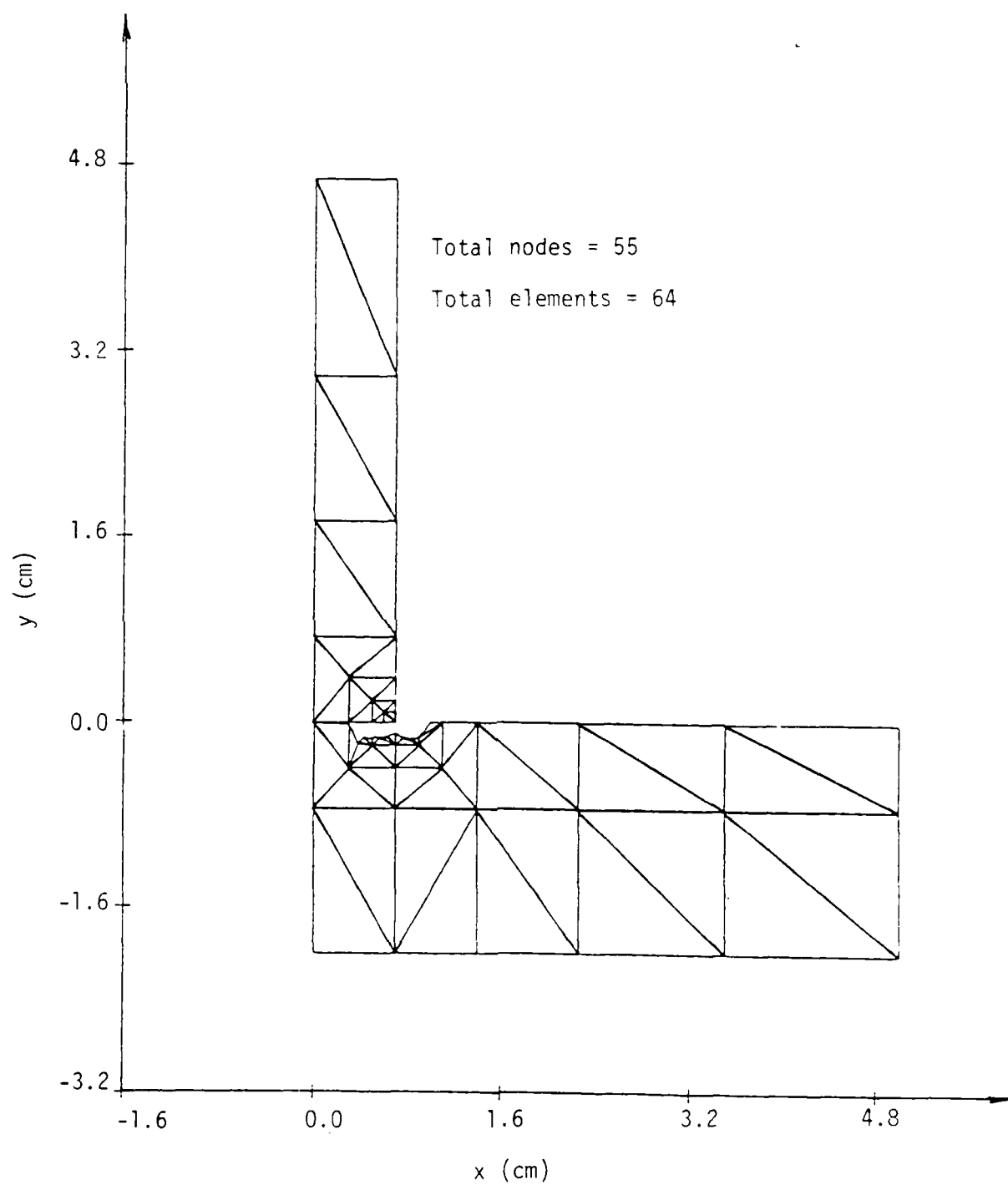


Figure 23. Remeshed grid pattern after 0.175  $\mu$ sec.



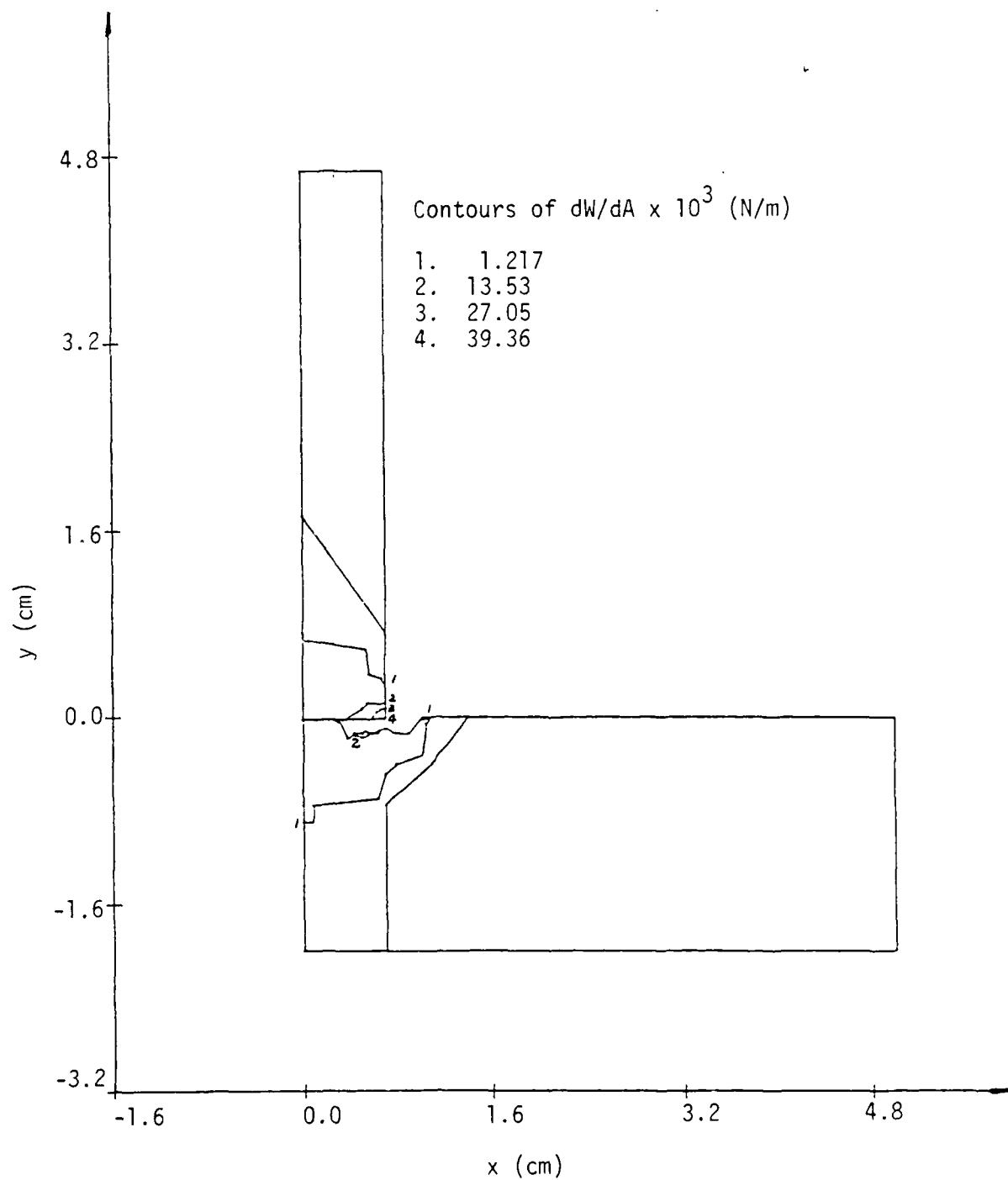


Figure 24. Contours of constant  $dW/dA$  at  $t = 0.240 \mu\text{sec}$ .

occur in a small element as indicated in Figure 25 with  $(dW/dV)_C = 7.29 \times 10^7 \text{ N/m}^2$ . A slight alteration of the fragmented zone is made in Figure 26 although its difference from Figure 22 is not noticeable at the scale level presented. Refer to Figure 27 for the remeshed grid pattern after 0.240  $\mu\text{sec}$ .

Since the dynamic disturbances propagate through the system at such a rapid rate, the geometry of the projectile/target system remained virtually unchanged. Exhibited in Figure 28 are the  $dW/dA$  contours in both the projectile and target for  $t = 0.345 \mu\text{sec}$ . At the projectile corner,  $dW/dA$  attained the values of  $41.62 \times 10^3 \text{ N/m}$  and  $60.56 \times 10^3 \text{ N/m}$  which have exceeded the critical surface energy density of  $38.99 \times 10^3 \text{ N/m}$ . Fracture of the corner element is thus assumed to take place. Additional damage also prevails near the already fragmented surface of the target where  $(dW/dA)_C$  has reached the values of  $10.9 \times 10^3 \text{ N/m}$  and  $16.2 \times 10^3 \text{ N/m}$  as shown in Figure 28. Similarly, the  $dW/dV$  contours in Figure 29 show that  $(dW/dV)_C = 179.6 \times 10^6 \text{ M/m}^2$  at the projectile corner and  $(dW/dV)_C = 80.34 \times 10^6 \text{ N/m}^2$  next to the cavity boundary in the target have also been exceeded. The resulting failure pattern is summarized schematically in Figure 30 while the corresponding grid pattern is presented in Figure 31. From here on, damage in the projectile and target tends to spread more widely as illustrated by the energy density contours in Figures 32 and 33. The computer output reveals that at  $t = 0.480 \mu\text{sec}$ , the  $(dW/dV)_C = 11.6 \times 10^3 \text{ N/m}$  critical boundary extends between contours no. 1 and no. 2 in Figure 32 from the target surface to its mid-portion dislocating and fracturing a large portion of the material. Figure 33 shows that  $dW/dV$  in several of the protruded regions has also been severely intensified beyond the critical value of  $(dW/dV)_C = 85.98 \times 10^6 \text{ N/m}^2$ . The material in these regions is fragmented into small pieces and can be removed by redistribution of the mass onto the neighboring nodal points. A schematic of the projectile/target

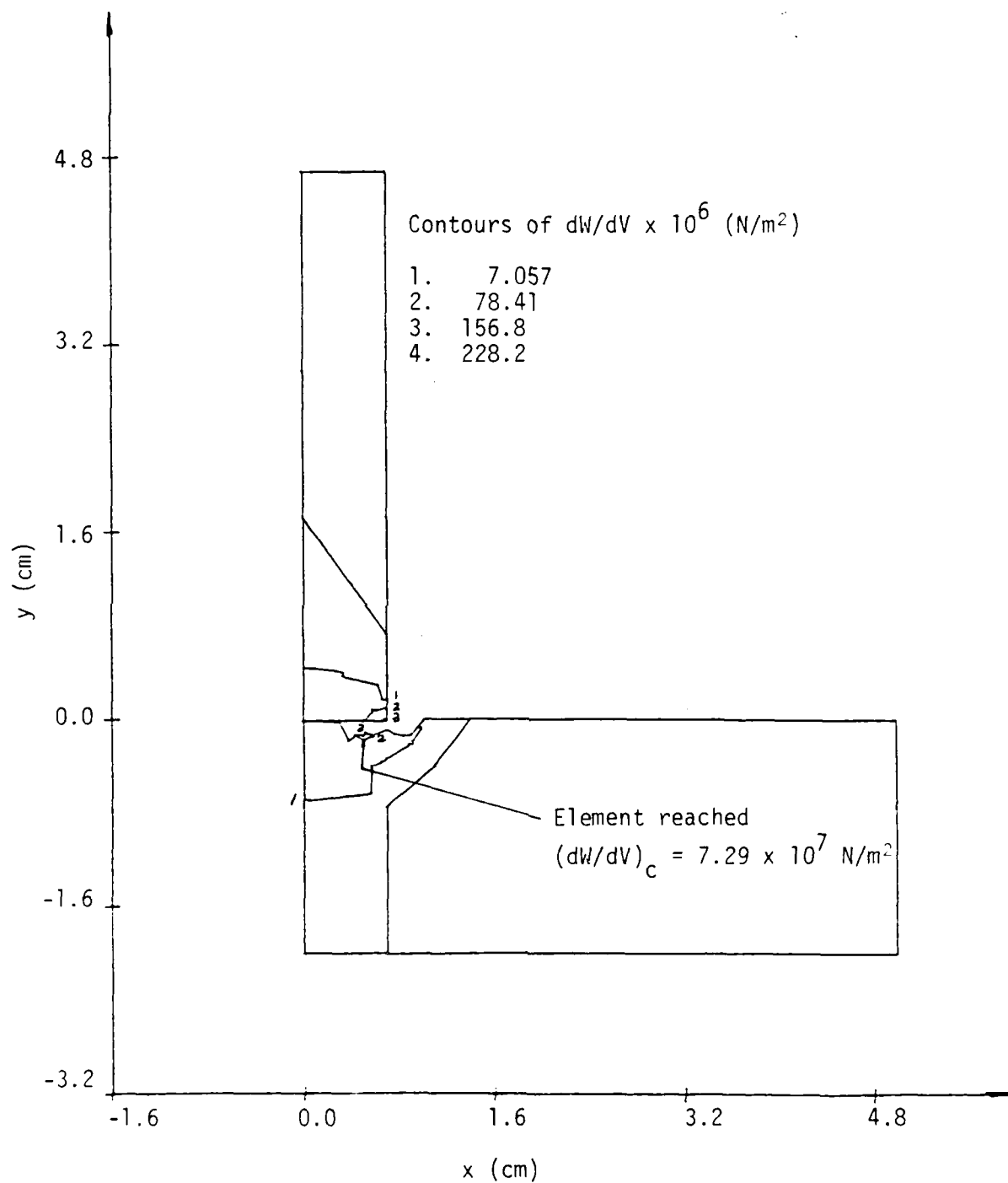


Figure 25. Contours of constant  $dW/dV$  at  $t = 0.240$  usec.

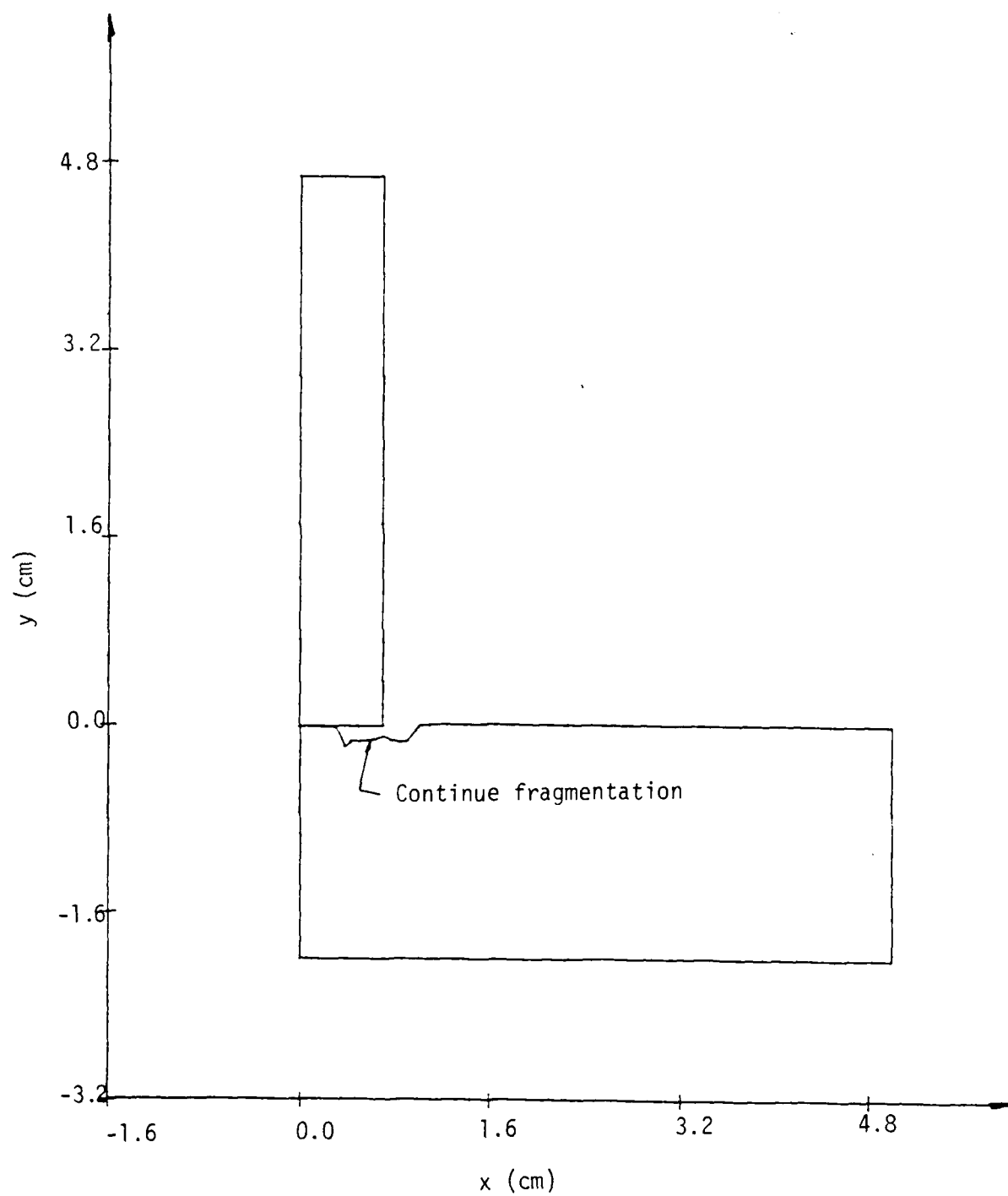


Figure 26. Fragmented target surface after 0.240  $\mu\text{sec}$ .

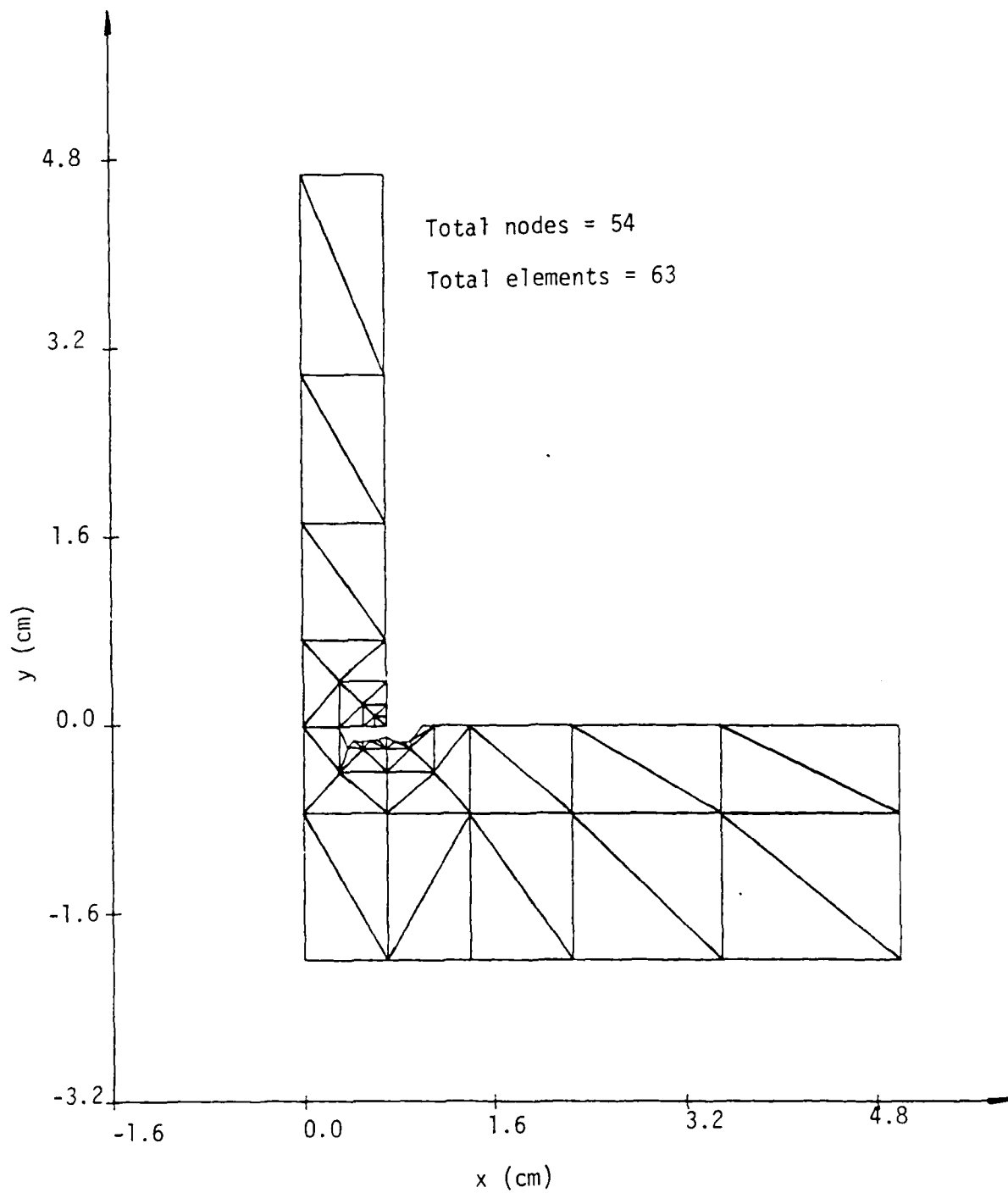


Figure 27. Remeshed grid pattern after 0.240  $\mu$ sec.

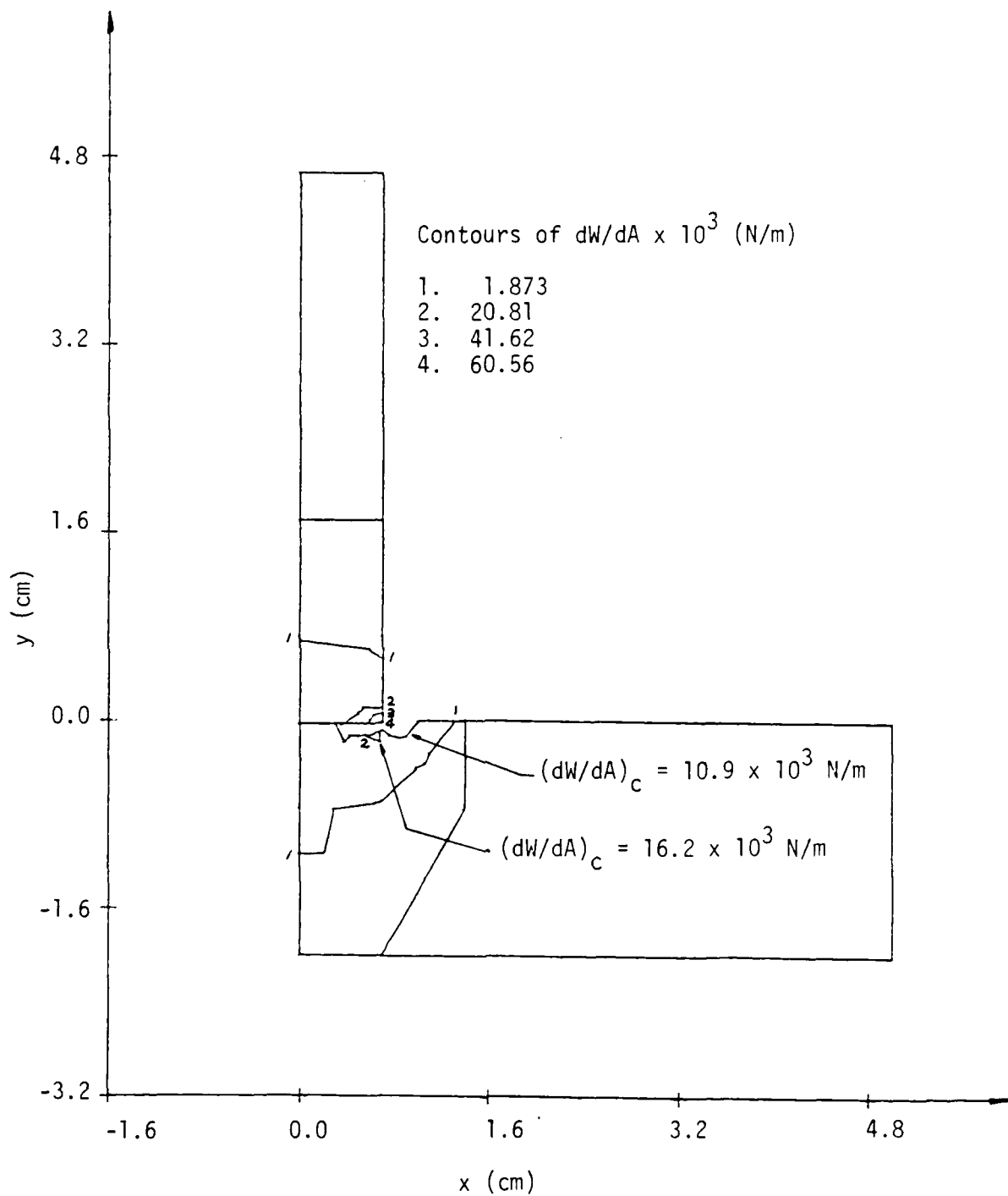


Figure 28. Contours of constant  $dW/dA$  at  $t = 0.345$  usec.

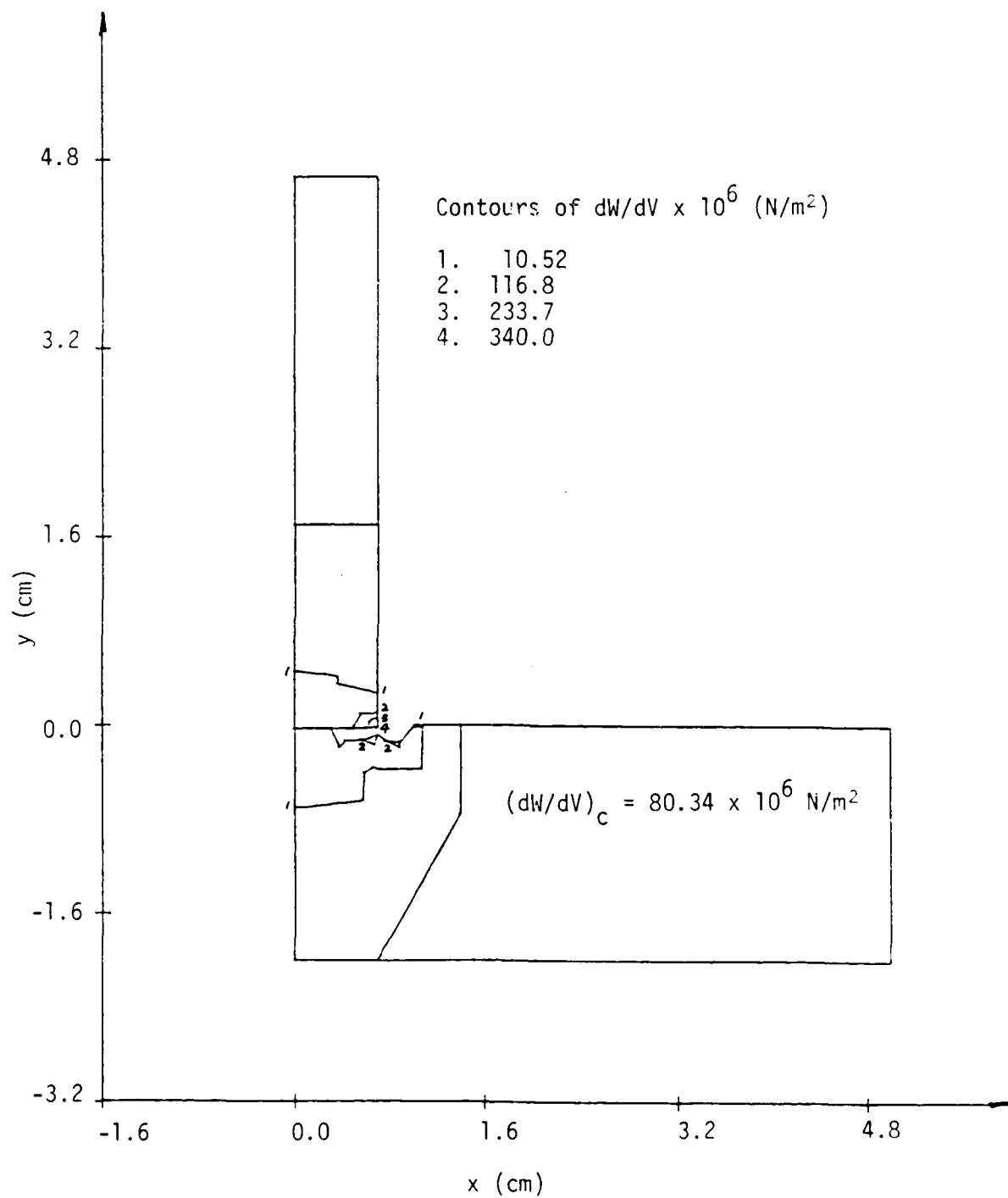


Figure 29. Contours of constant  $dW/dV$  at  $t = 0.345 \text{ } \mu\text{sec}$ .

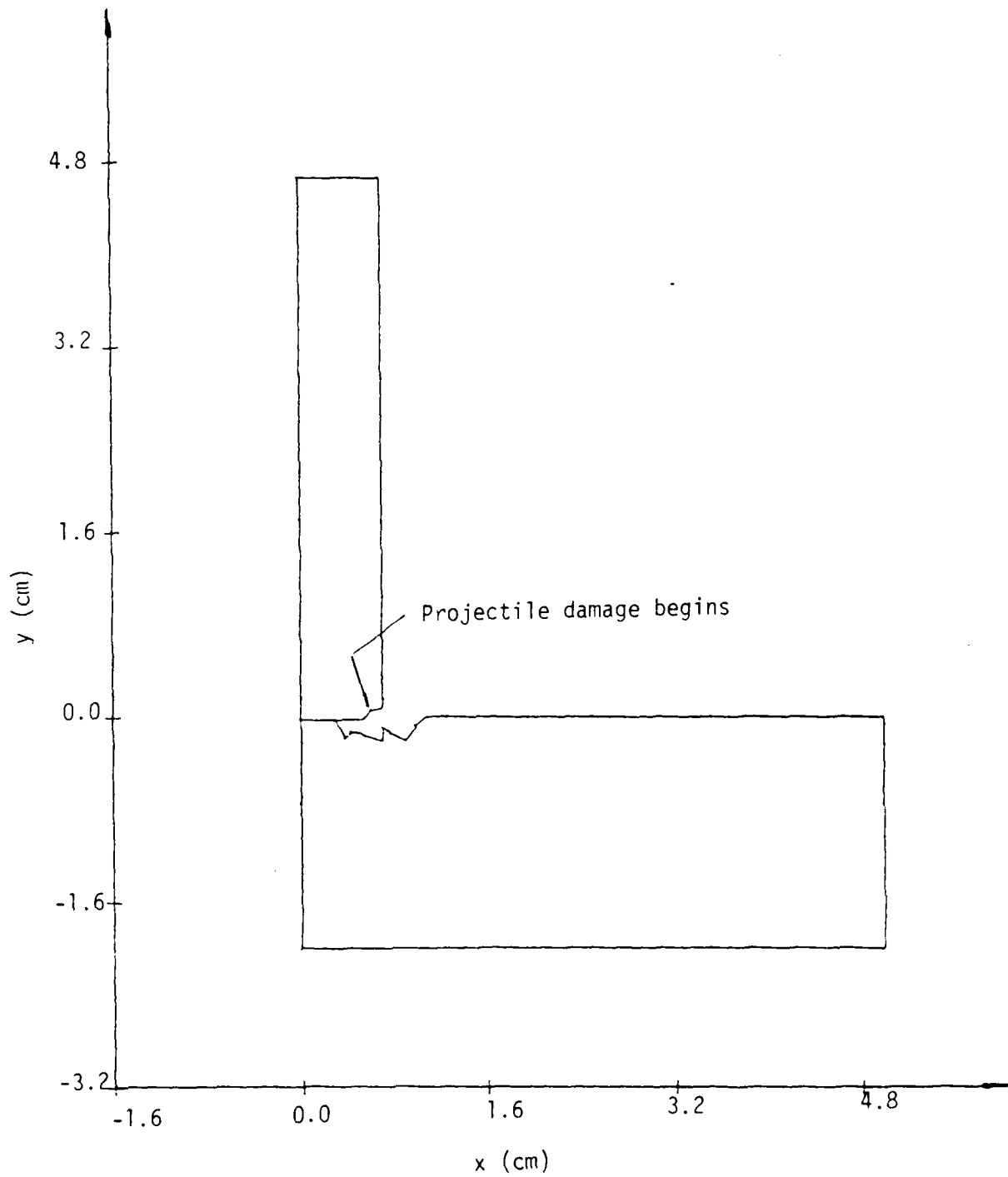


Figure 30. Projectile/target damage pattern after 0.345 μsec.



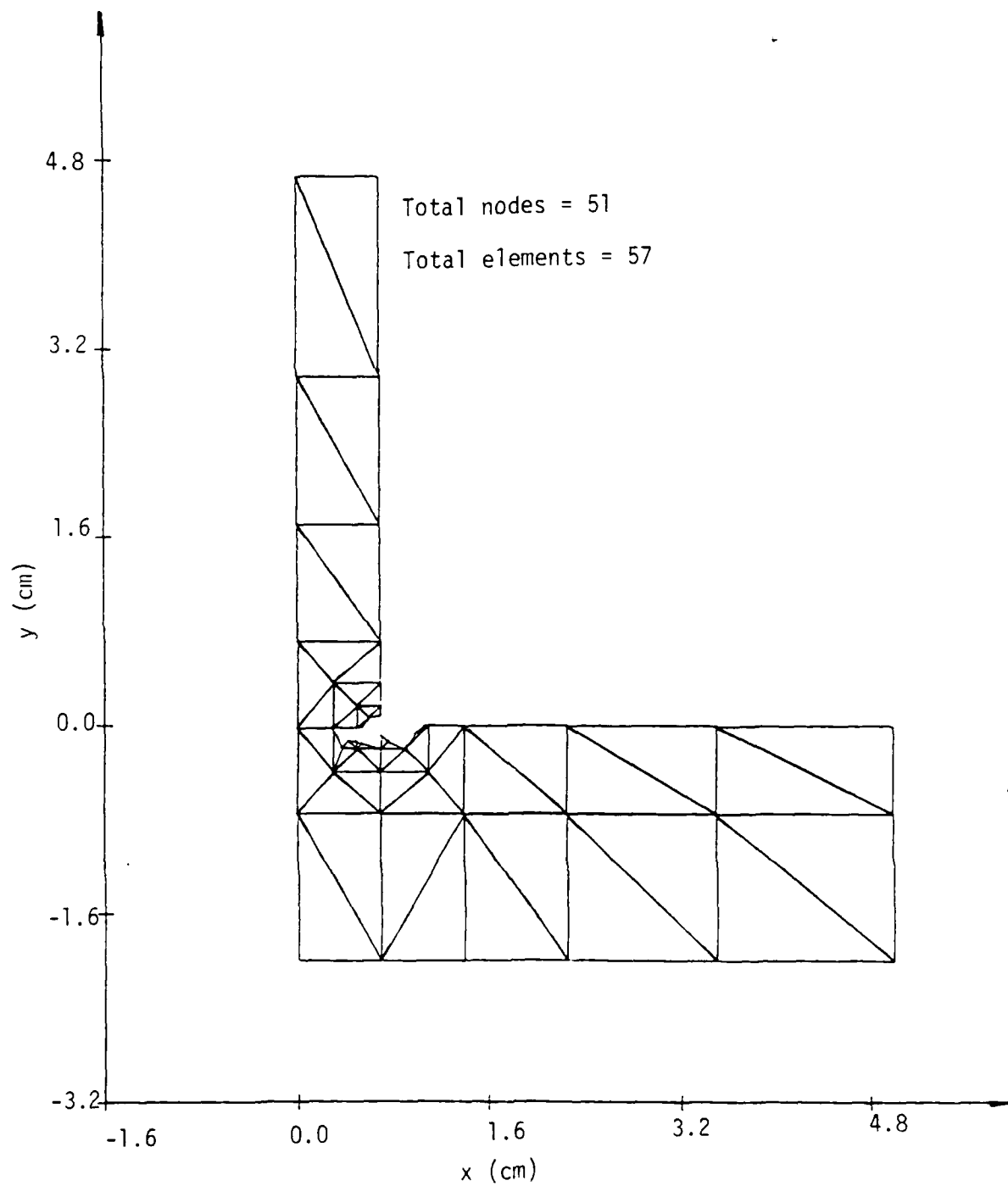


Figure 31. Remeshing of damaged projectile/target system after 0.345  $\mu$ sec.

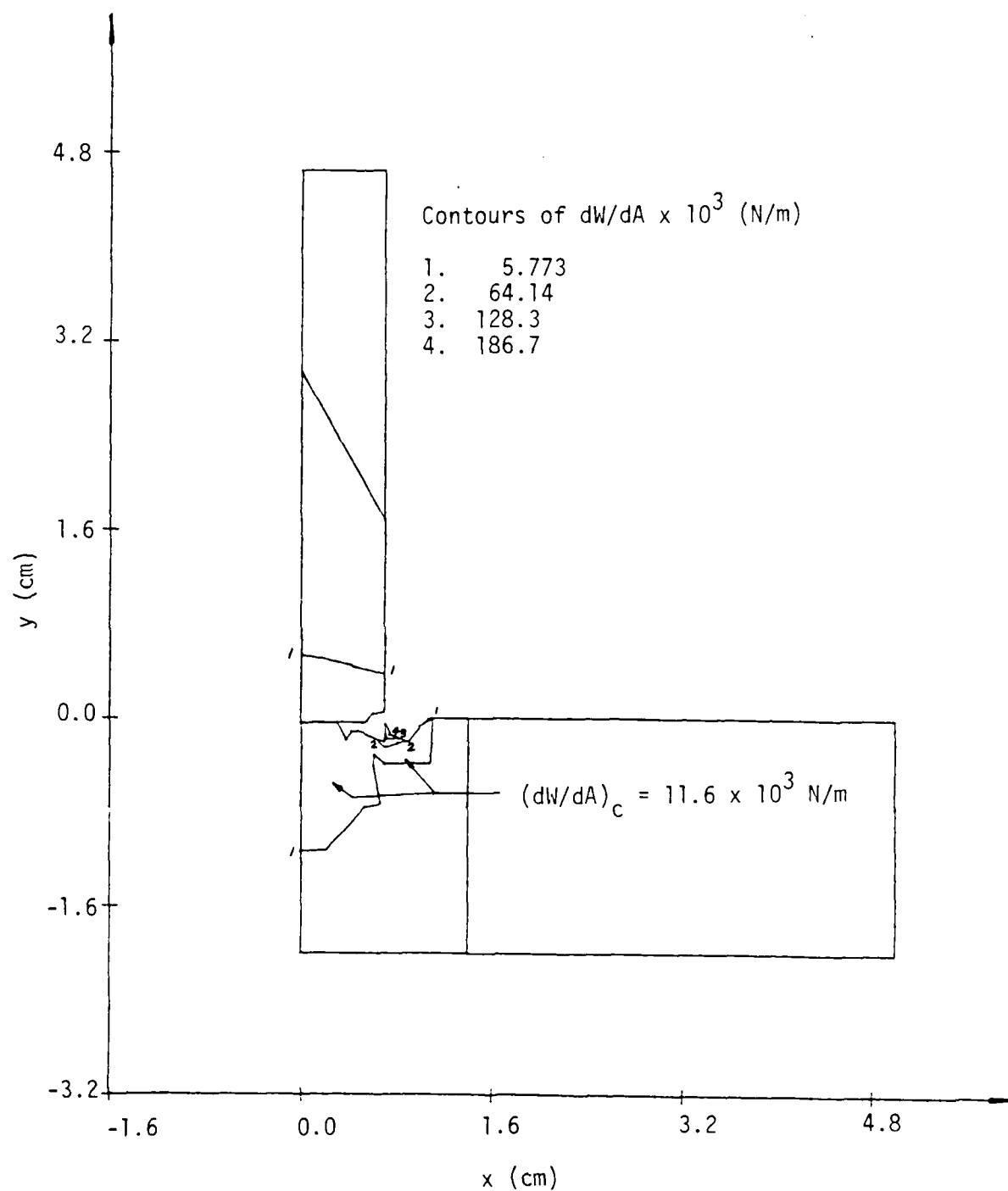


Figure 32. Contours of constant  $dW/dA$  at  $t = 0.480$  usec.

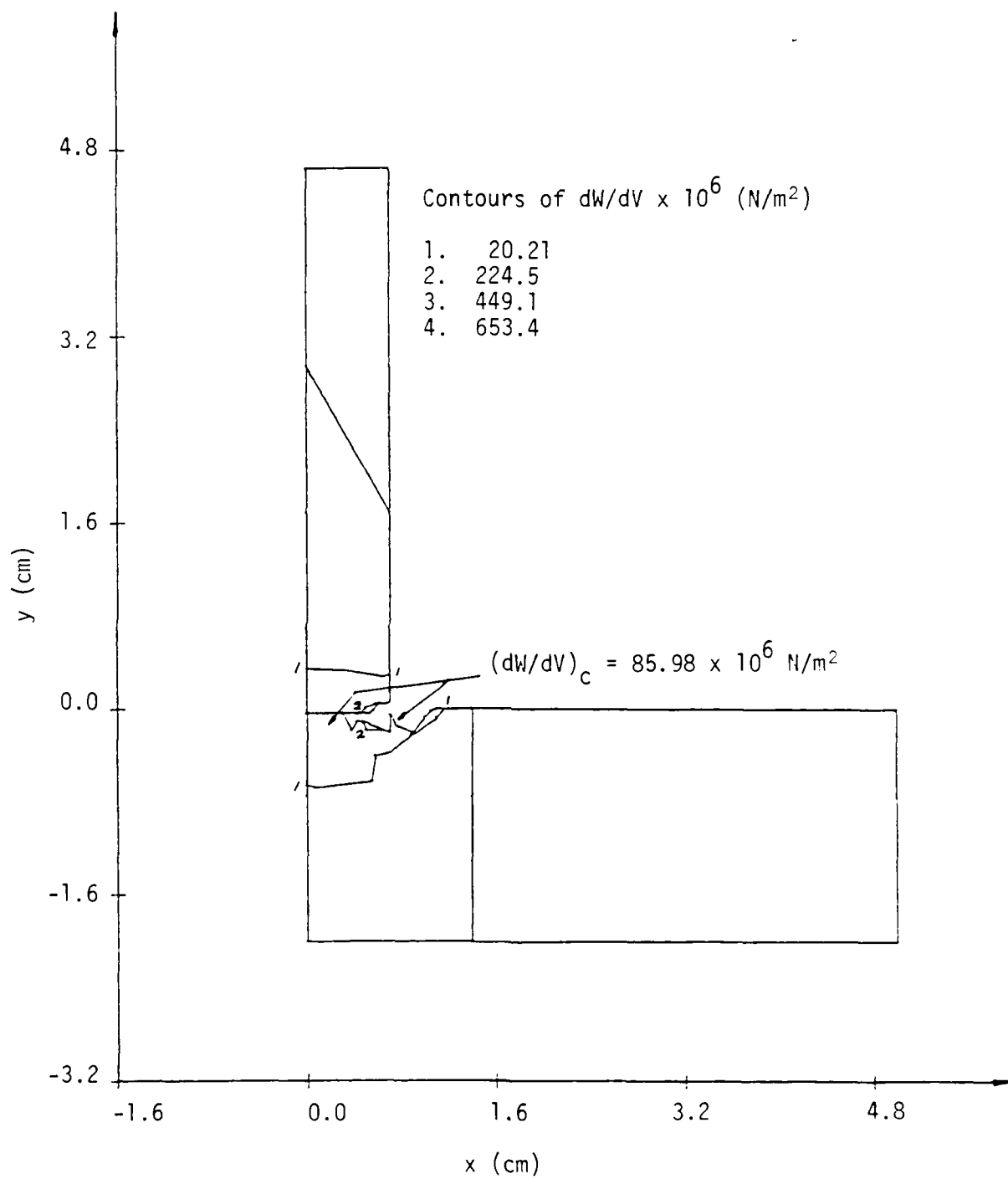


Figure 33. Contours of constant  $dW/dV$  at  $t = 0.480 \mu\text{sec}$ .

failure pattern after 0.480  $\mu$ sec is shown in Figure 34. Three separate fragments are indicated which are in loose contact with the target. A gap following the  $(dW/dV)_c = 11.6 \times 10^3$  N/m critical contour is modelled in Figure 35 that contains 114 elements and 97 nodes. The largest block of loose material is near the center and is barely in contact with the projectile. The damage pattern at  $t = 0.501$   $\mu$ sec of the projectile/target system is virtually unchanged from that at  $t = 0.480$   $\mu$ sec. What has altered slightly is only the partial disintegration of one of the fragments as illustrated in both Figures 36 and 37. This minor correction is made in Figures 38 while Figure 39 gives the new grid pattern for the next time increment of computation. The results for  $t = 0.562$   $\mu$ sec are displayed in Figures 40 and 41. As the dynamic disturbances have now been well propagated into the system, the surface energy density  $dW/dA$  begins to be less dominant and remains below the damage threshold shown in Figure 40 while the volume energy density  $dW/dV$  starts to increase more readily. Further disintegration of the fragments occurred as the volume energy density intensified substantially beyond  $(dW/dV)_c = 85.98 \times 10^6$  N/m<sup>2</sup>, Figure 41. Modified in Figures 42 and 43 are the fragmented configuration after 0.562  $\mu$ sec.

Damage continues to accumulate as  $t$  is increased to 0.663  $\mu$ sec due to the increase in the local values of  $dW/dA$  and  $dW/dV$ . The sites of failure owing to excessive surface energy are identified in Figure 44 with the different values of  $(dW/dA)_c$  in the target and projectile. Figure 45 gives the corresponding critical values of  $dW/dV$ . The large fragment that was originally in contact with the projectile has now been broken into two resulting in a total of four pieces and leaving a space between the projectile and target. This is shown in Figure 46 with the corresponding grid pattern in Figure 47 that employed 100 elements and 89 nodes. Multiple fragmentation after 0.633  $\mu$ sec created a wide space such

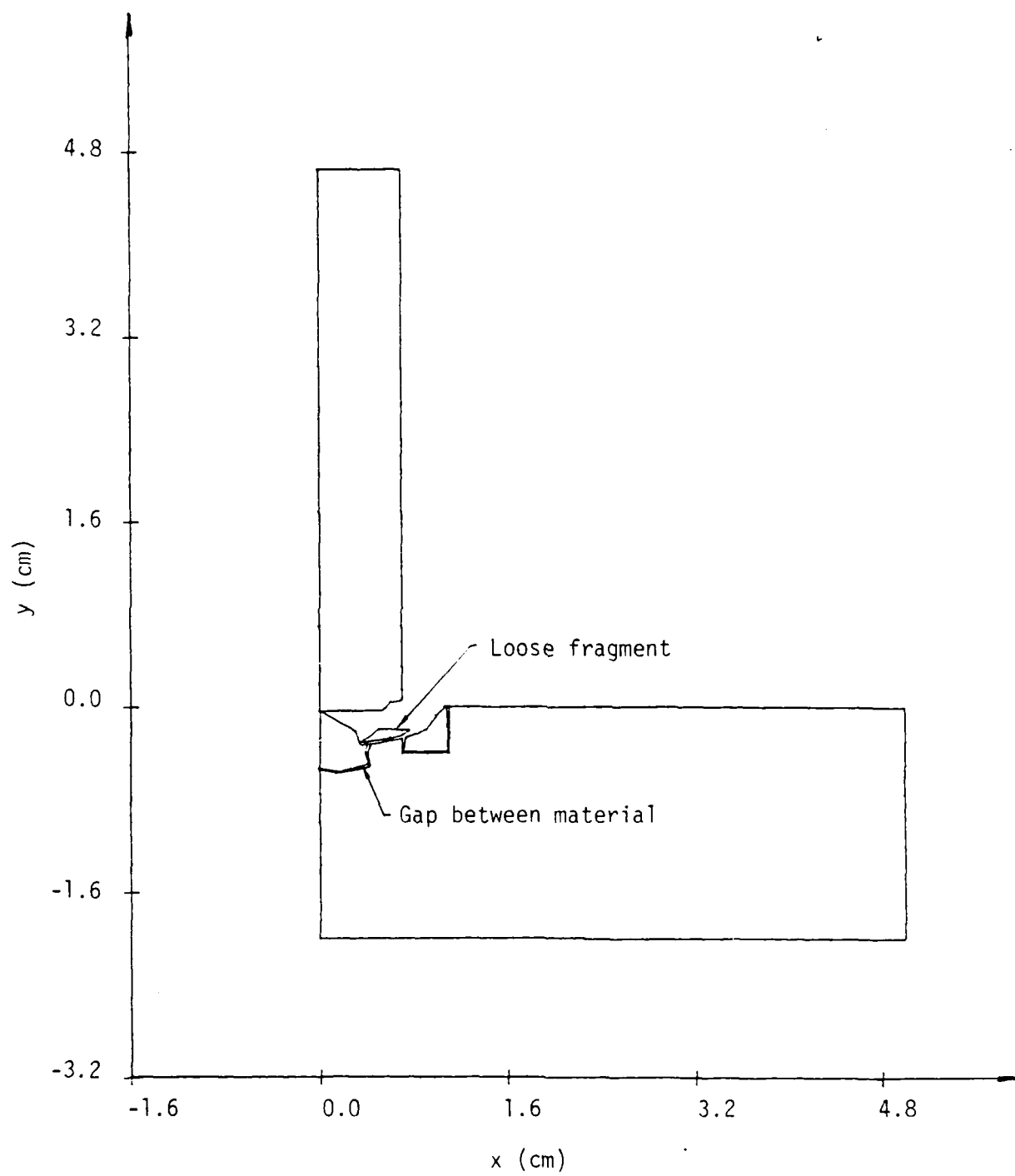


Figure 34. Damage of projectile/target system after 0.480  $\mu\text{sec}$ .

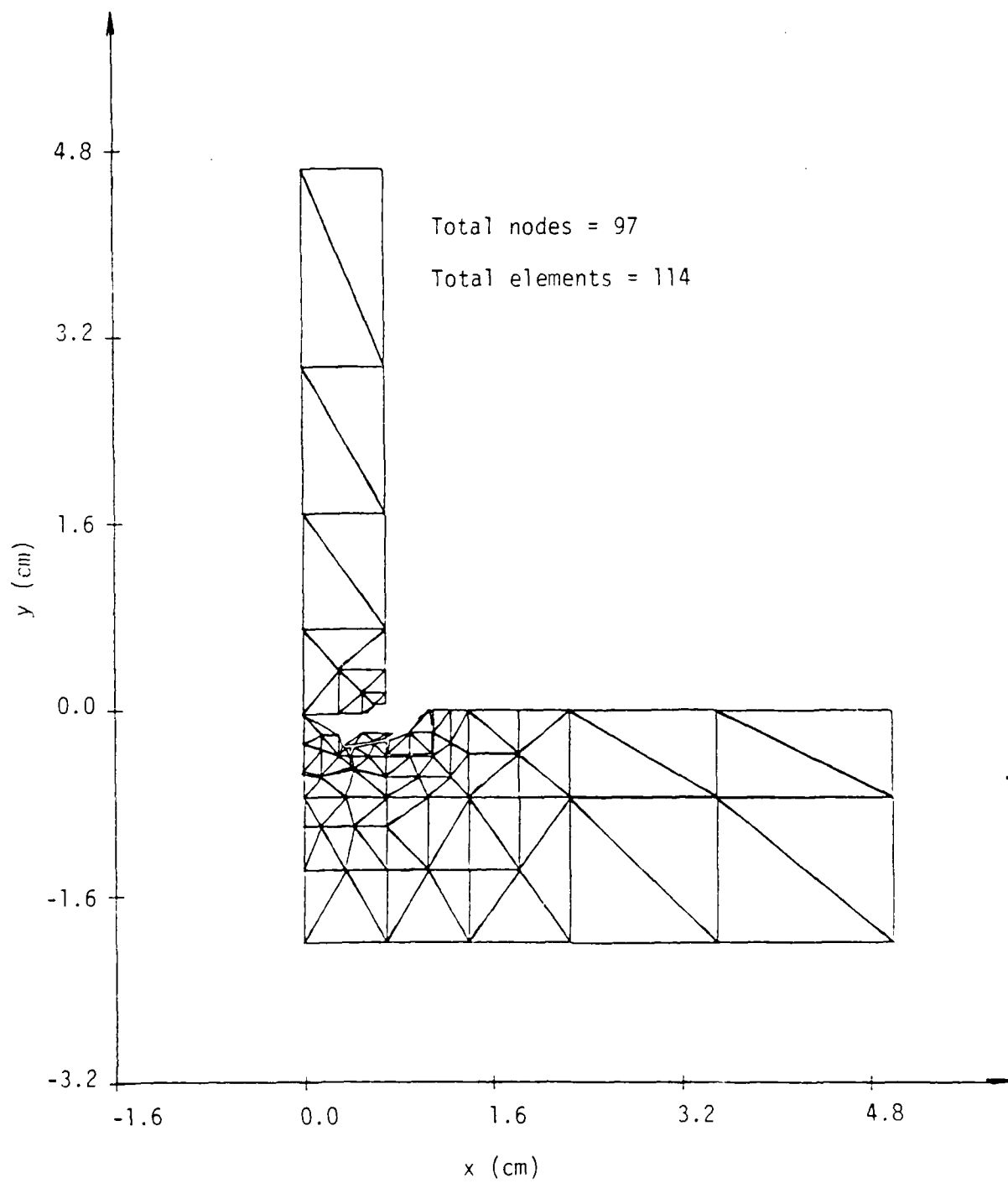


Figure 35. Grid pattern of damaged system after 0.480 sec.

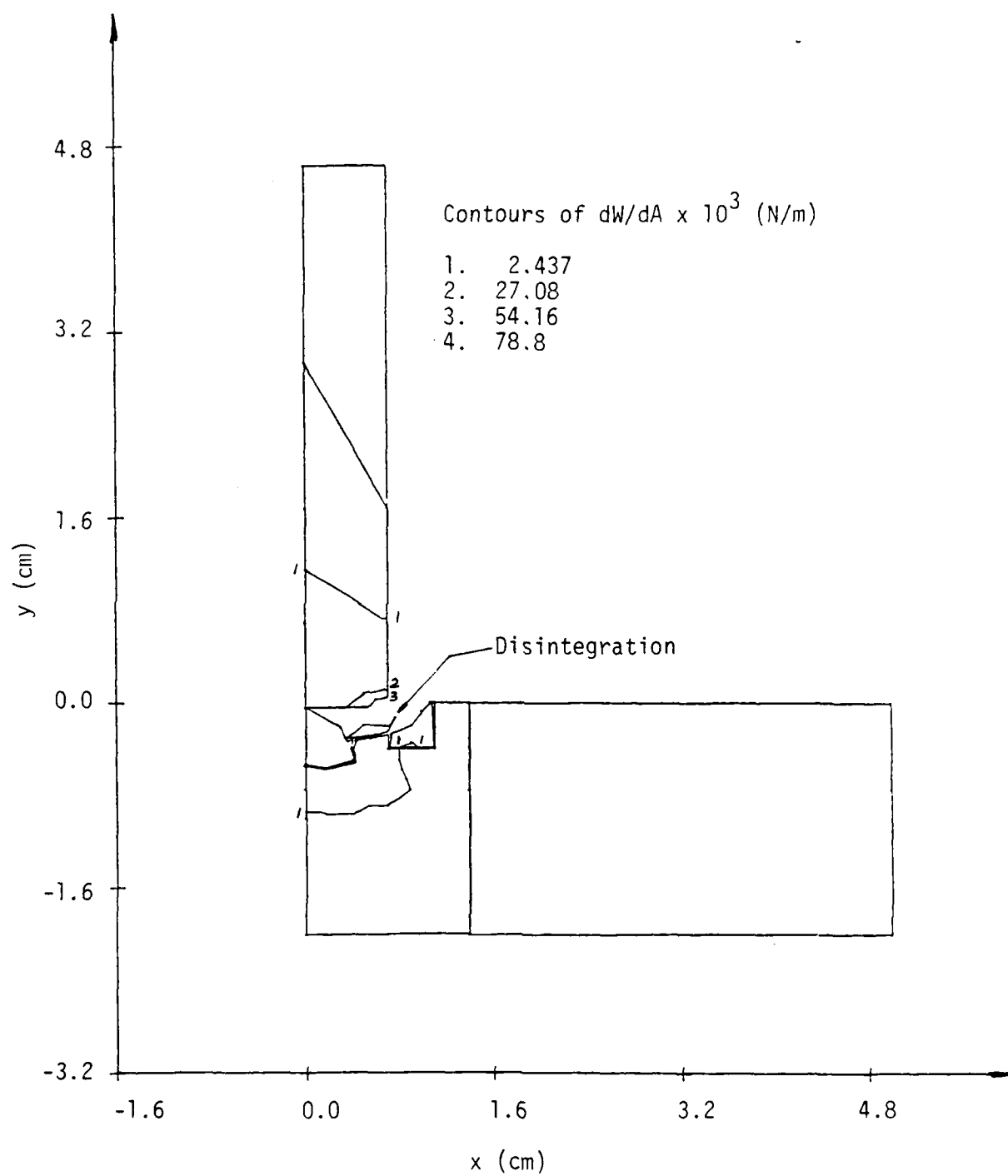


Figure 36. Contours of constant  $dW/dA$  at  $t = 0.501$  usec.

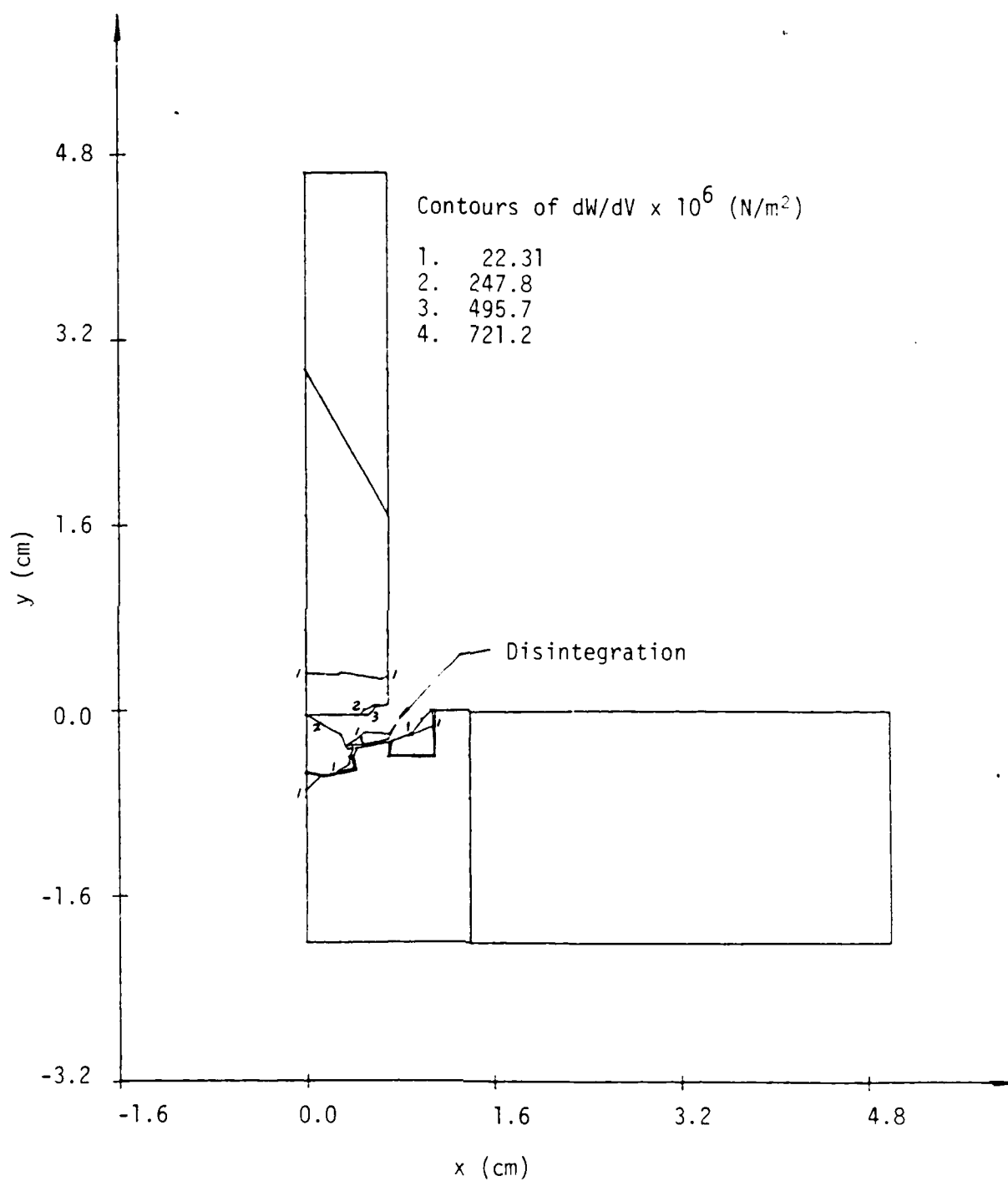


Figure 37. Contours of constant  $dW/dV$  at  $t = 0.501 \mu\text{sec}$ .



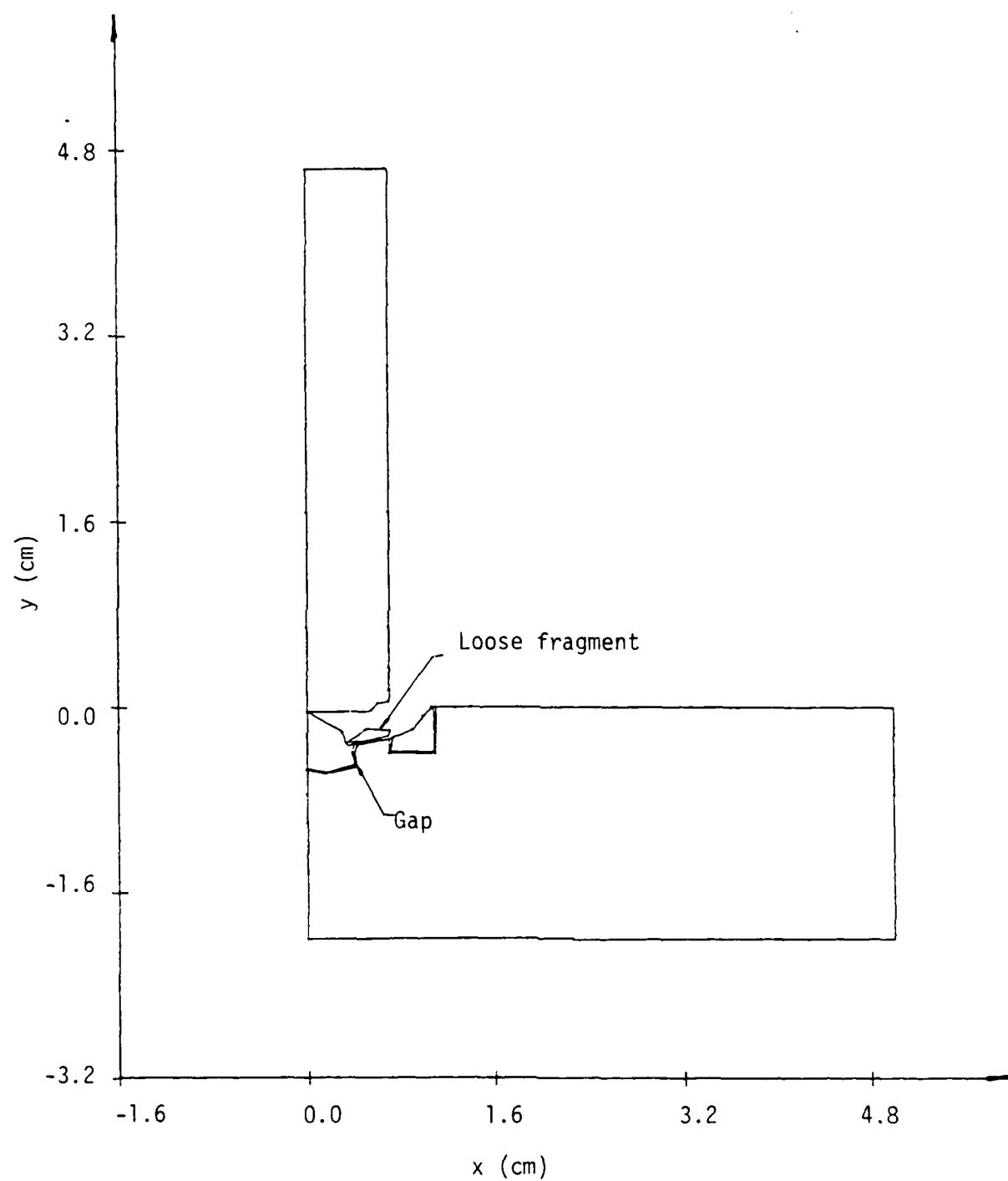


Figure 38. Damage pattern after 0.501  $\mu\text{sec}$ .

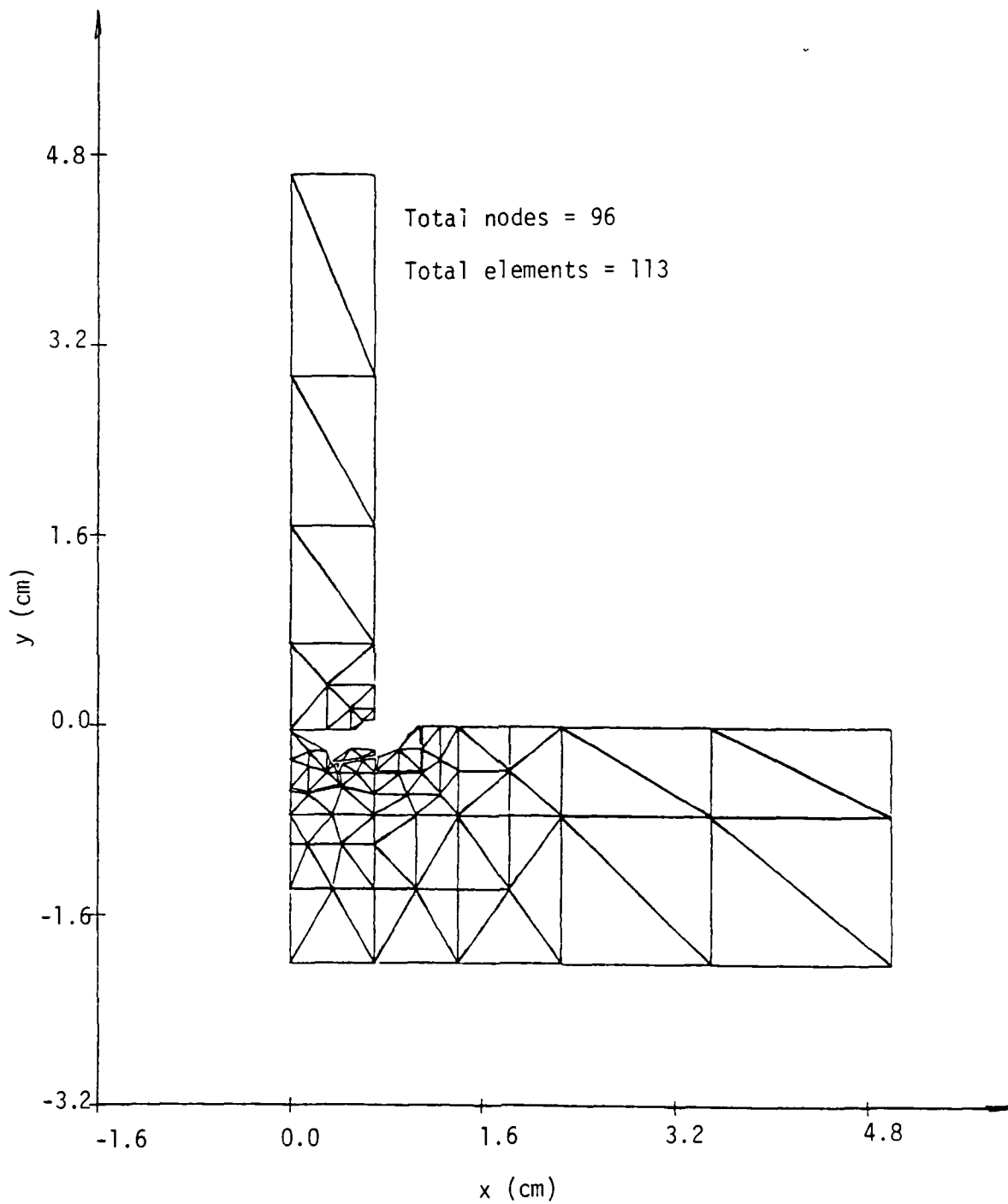


Figure 39. Grid pattern of projectile/target system after 0.501  $\mu$ sec.

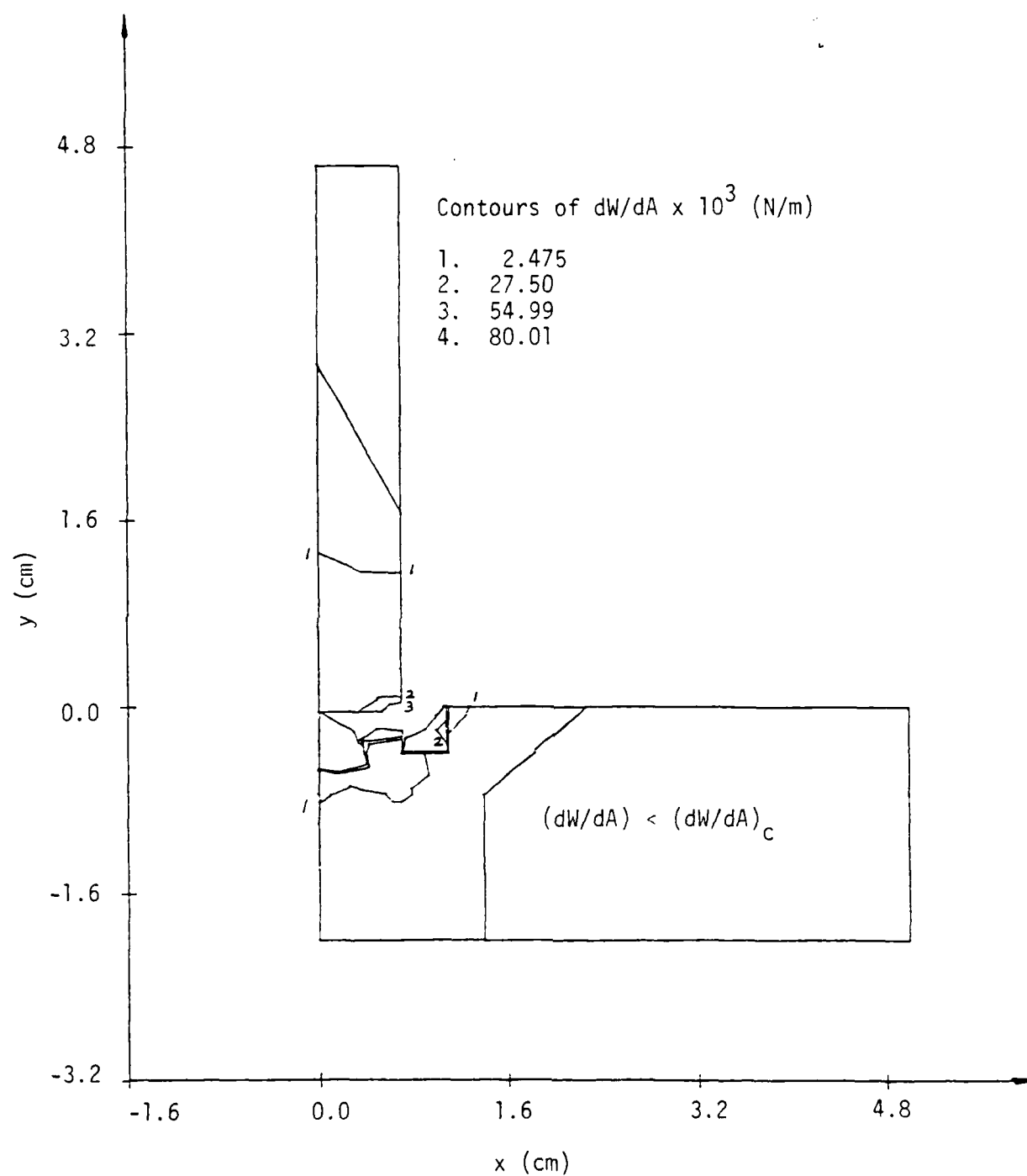


Figure 40. Contours of constant  $dW/dA$  at  $t = 0.562 \mu\text{sec}$ .

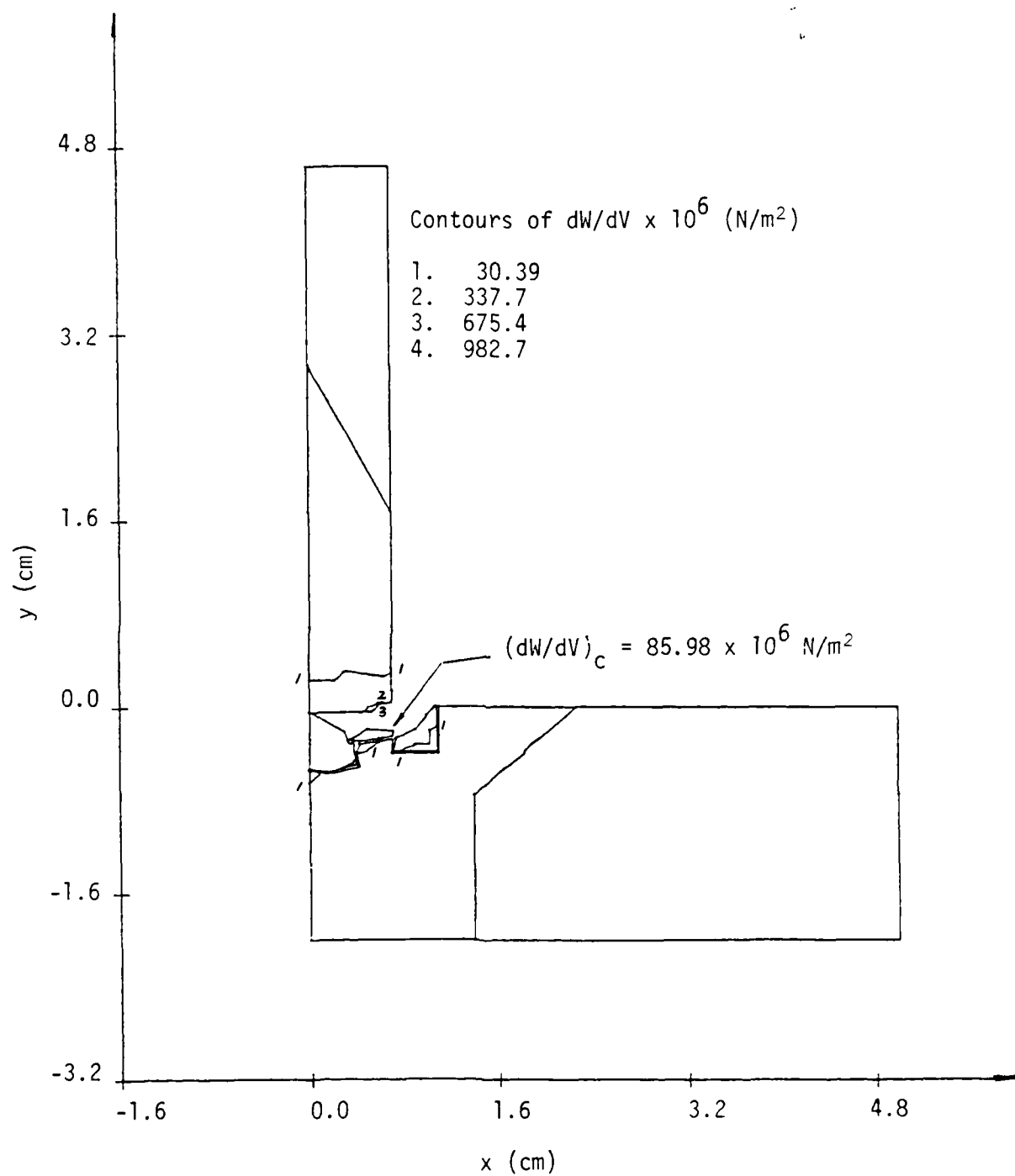


Figure 41. Contours of constant  $dW/dV$  at  $t = 0.562$   $\mu$ sec.

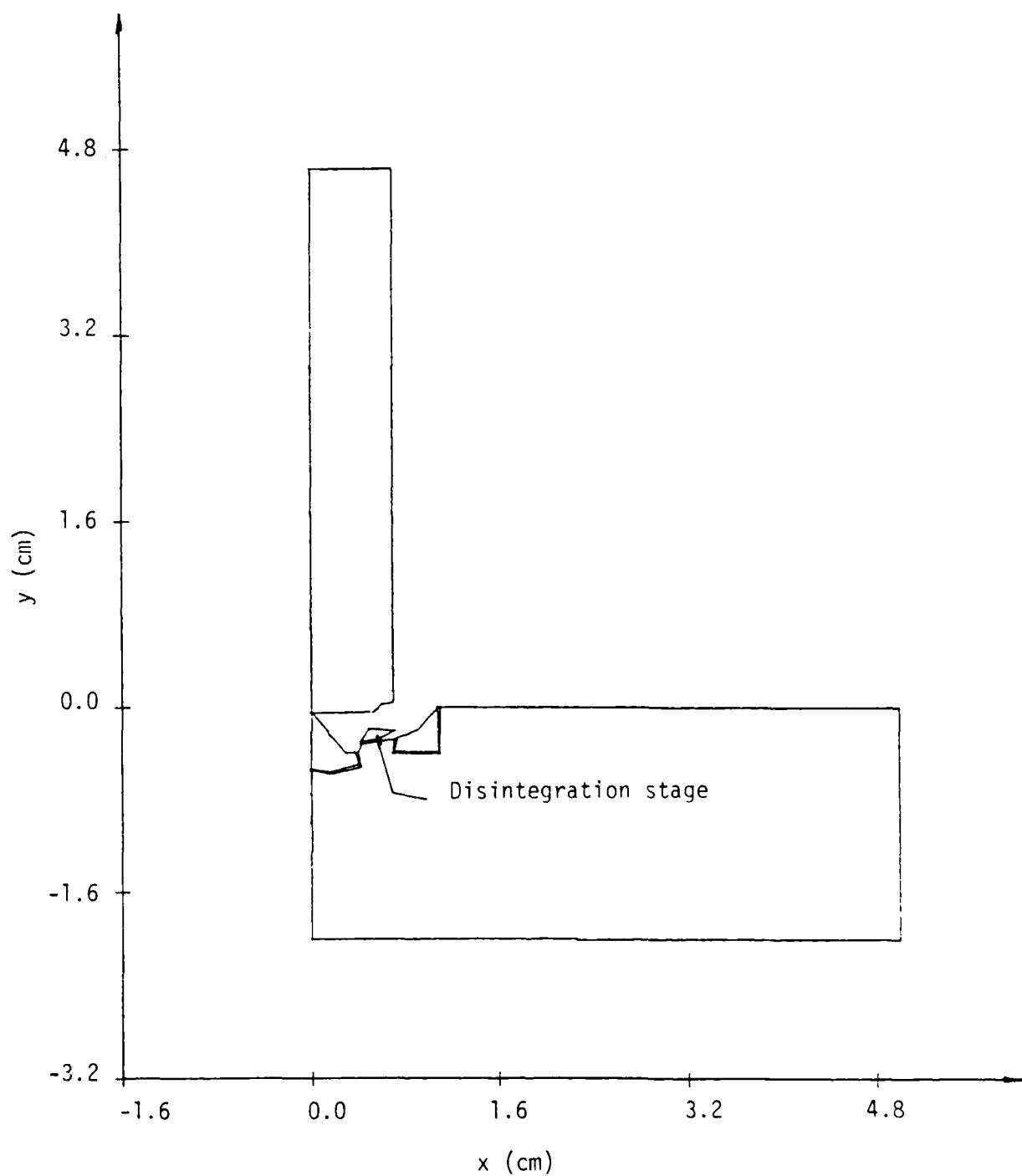


Figure 42. Damage of projectile/target after 0.562  $\mu$ sec.

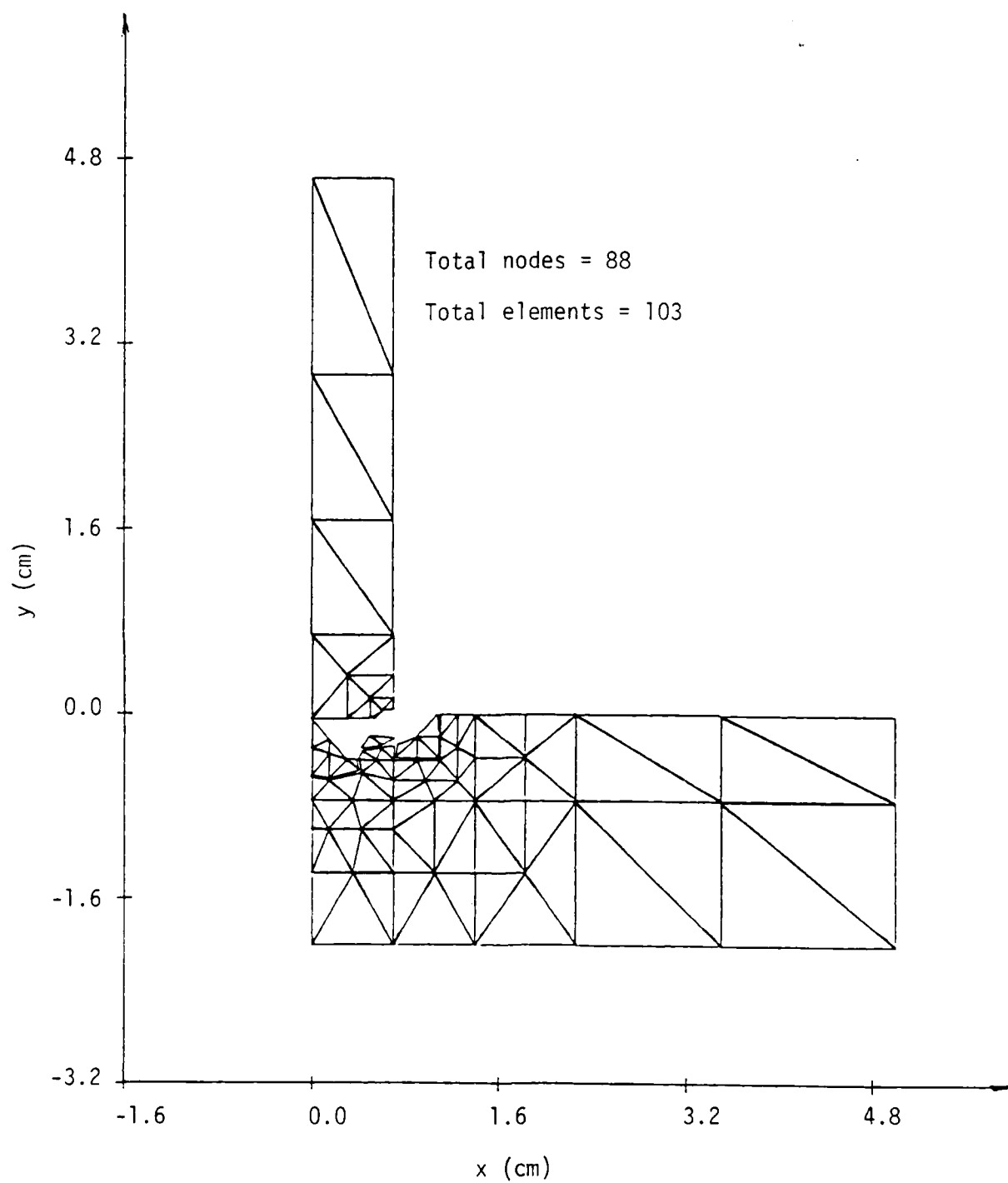


Figure 43. Modified grid pattern after 0.562  $\mu$ sec.

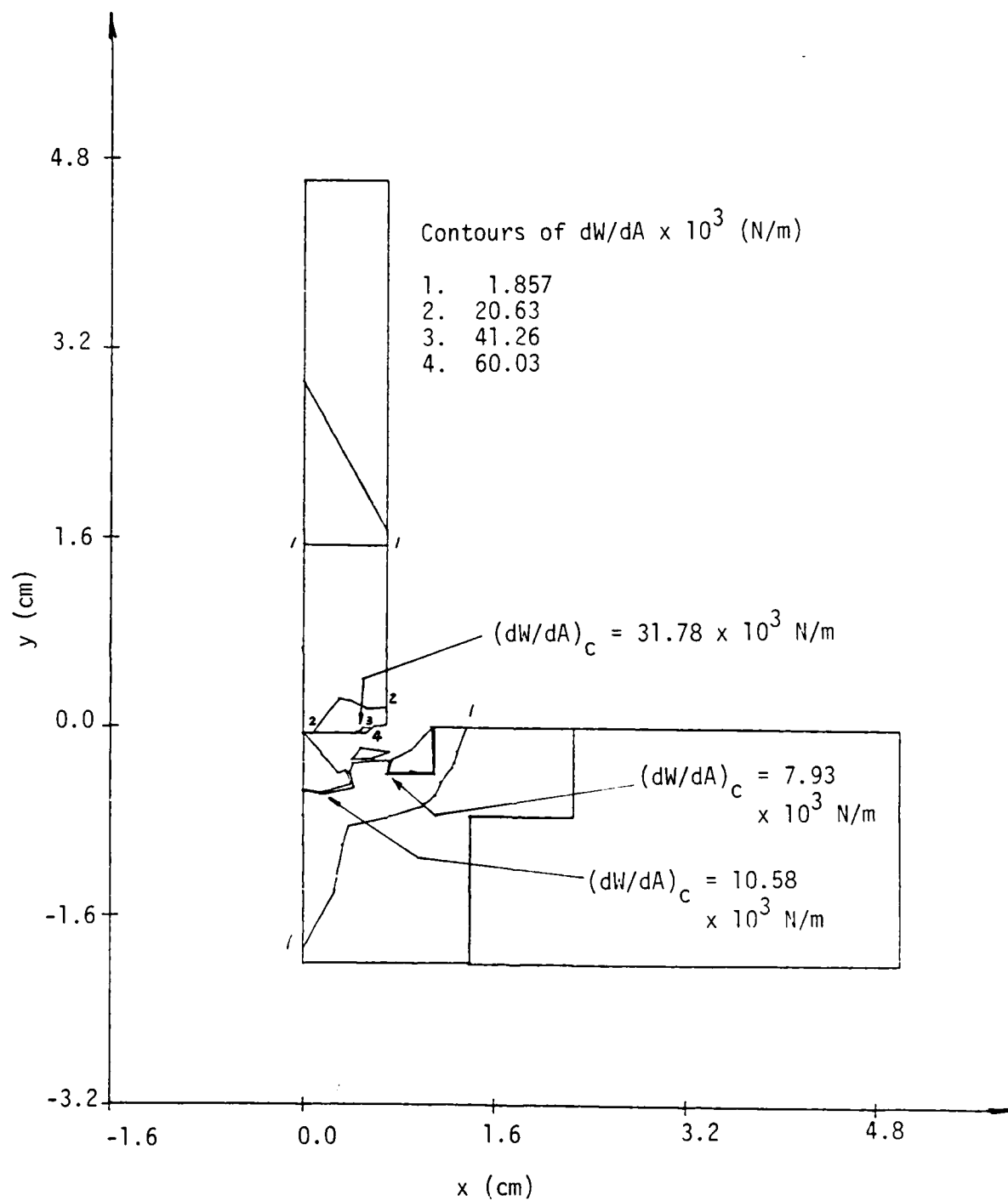


Figure 44. Contours of constant  $dW/dA$  at  $t = 0.663$  usec.

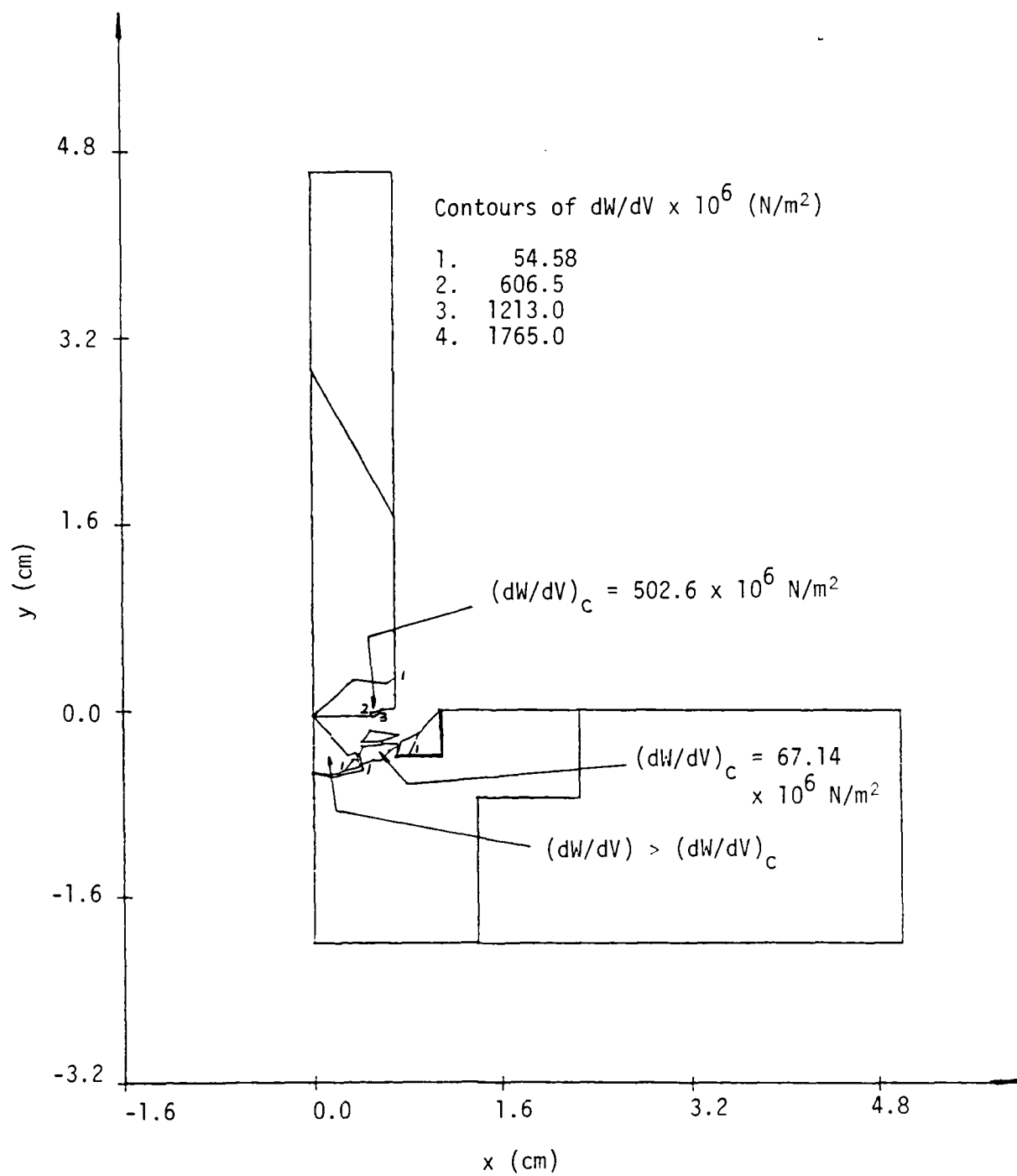


Figure 45. Contours of constant  $dW/dV$  at  $t = 0.663$  usec.



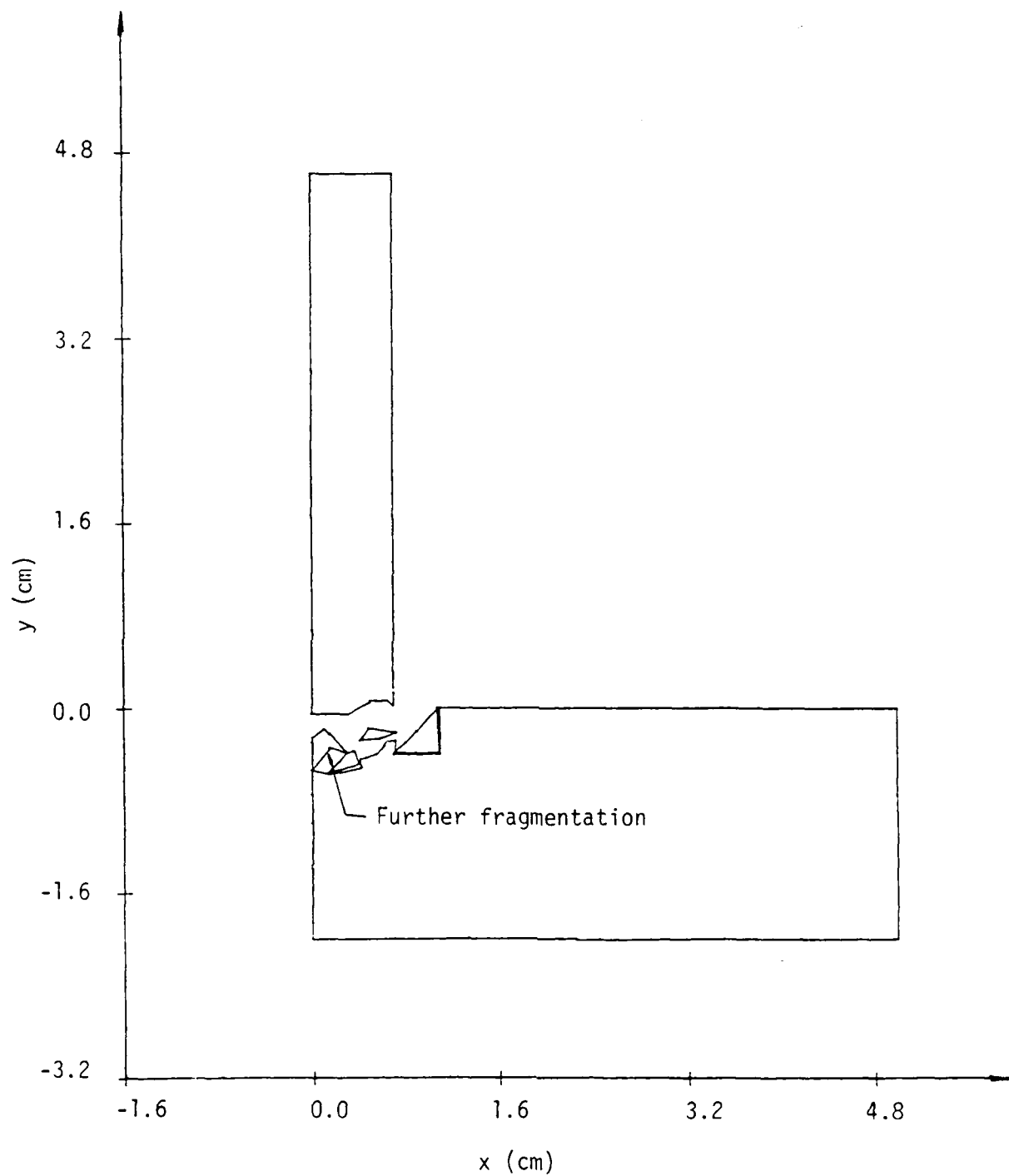


Figure 46. Fragmentation at 0.663 usec.

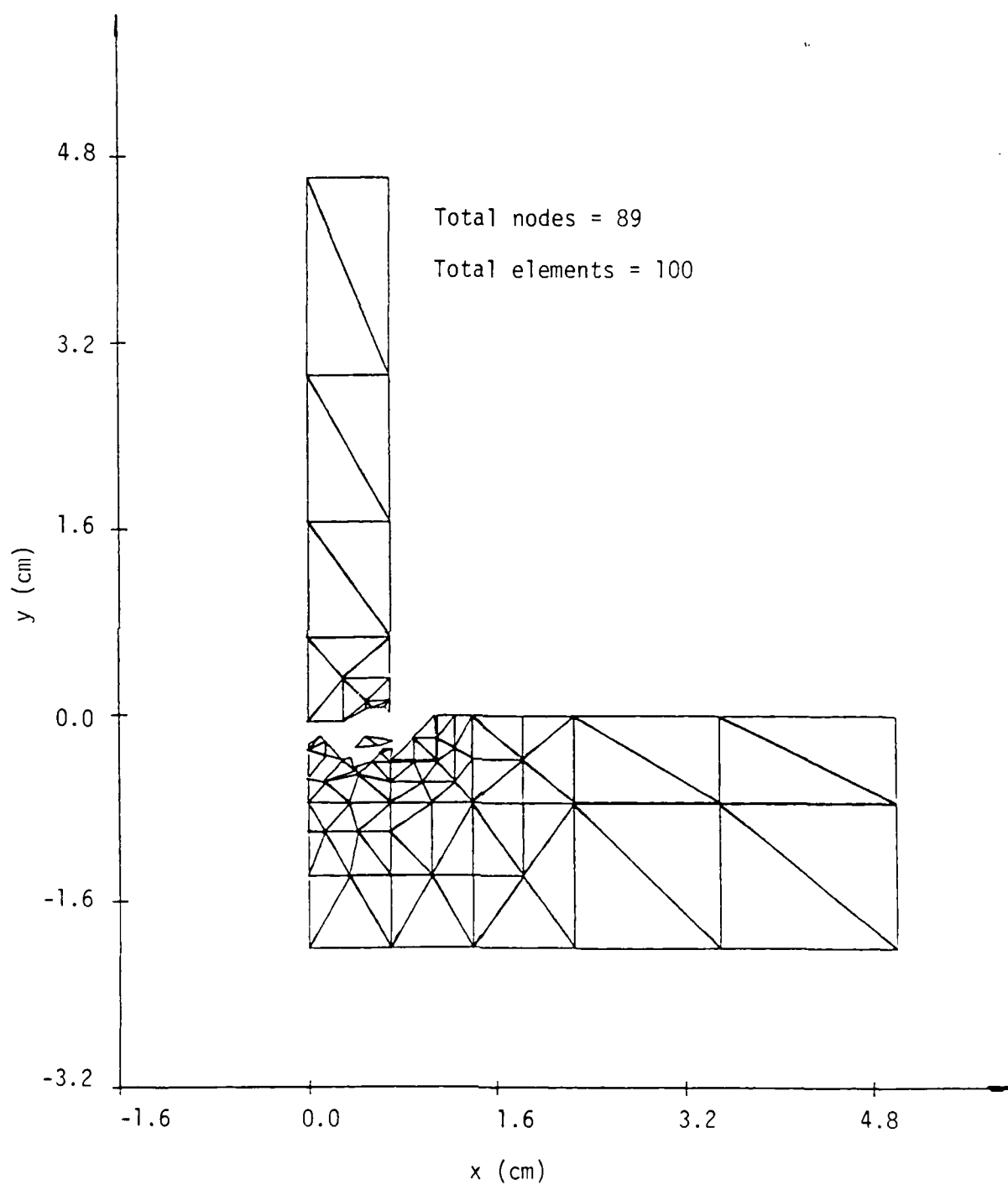


Figure 47. Remeshing of fragmented projectile and target after 0.663  $\mu$ sec.

that the projectile is not in contact with the target. The local surface and volume energy density as shown in Figures 48 and 49 continue to elevate leading to an increase in the cavity size and further disintegration of the fragments. The smaller debris has little or no influence on the dynamic behavior of the system and can be removed. This leads to the configuration in Figure 50 whose grid pattern is given in Figure 51. A glance at the results in Figures 52 to 55 show that almost the entire projectile is now under stress or strain. However, change in the failure pattern during the time interval of  $t = 0.764 \mu\text{sec}$  and  $0.869 \mu\text{sec}$  involves only the disintegration of one fragment near the center. There remains only two loose fragments as indicated in Figures 54 and 55. Even though the projectile is not in direct contact with the target at  $t = 0.924 \mu\text{sec}$ , damage continues to occur because of the increase in  $dW/dA$  and  $dW/dV$ . Separation of a layer of material or fracture is predicted near the projectile end in Figures 56 and 57 because both the surface and volume energy density have exceeded the respective critical values of  $25.86 \times 10^3 \text{ N/m}$  and  $180.5 \times 10^6 \text{ N/m}^2$ . The volume energy density in two fragments is also much greater than  $(dW/dV)_c = 48 \times 10^6 \text{ N/m}^2$ . At this instance, all fragments have disintegrated leaving a large cavity between the projectile and target. This configuration is modelled in Figures 58 and 59.

Since the projectile is still not in contact with the target, there is time for the surface energy density near the cavity boundary to decrease below the critical value, Figure 60. The volume energy density inside the surface given in Figure 61, however, remains large and causes further fracture. A zig-zag fracture surface is predicted at  $t = 1.024 \mu\text{sec}$ . Refer to Figure 62 and the grid pattern in Figure 63. Again, the surface energy density near the fractured area in the target remained below critical while only that in the projectile as shown

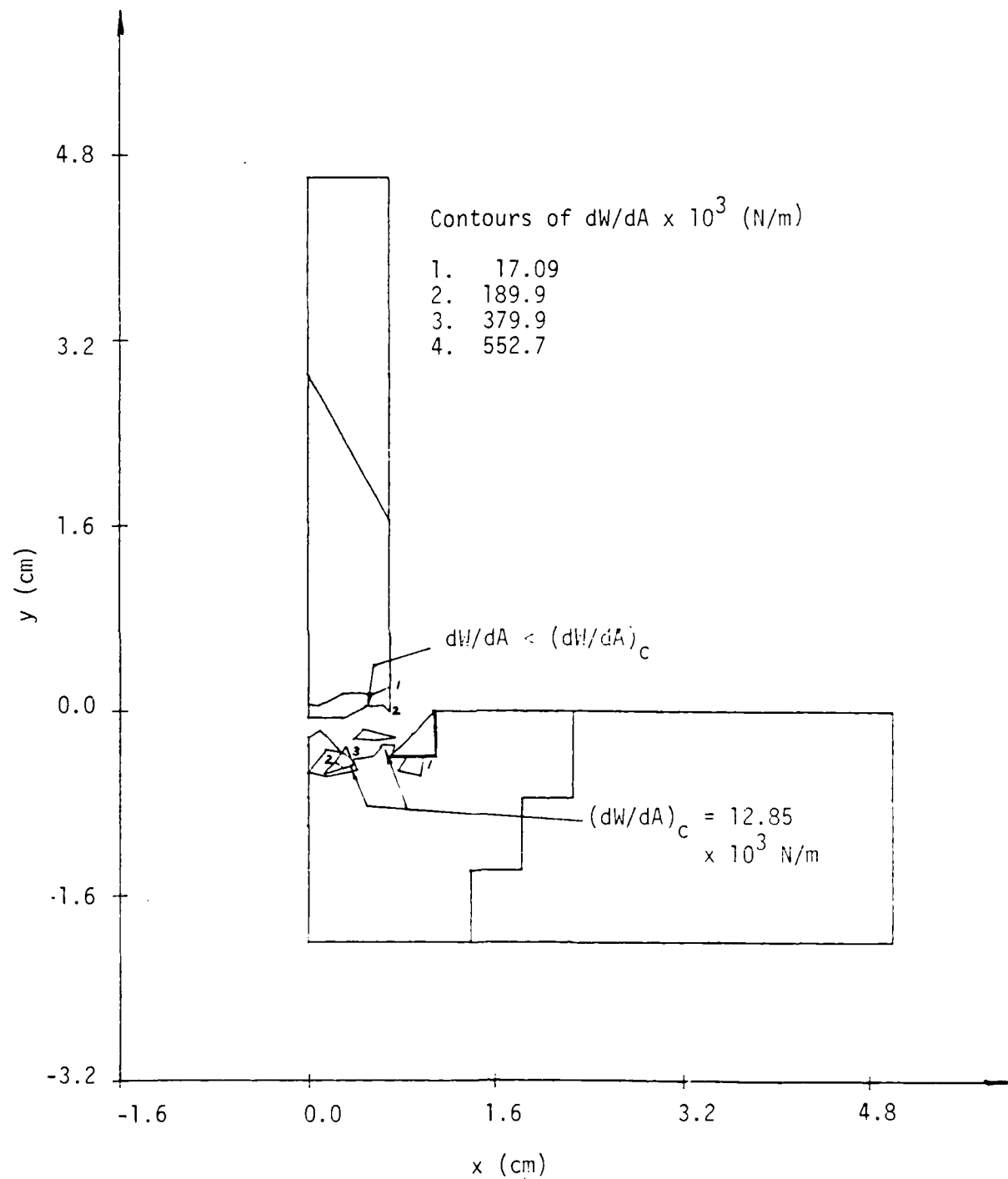


Figure 48. Contours of constant  $dW/dA$  at  $t = 0.764 \mu\text{sec}$ .

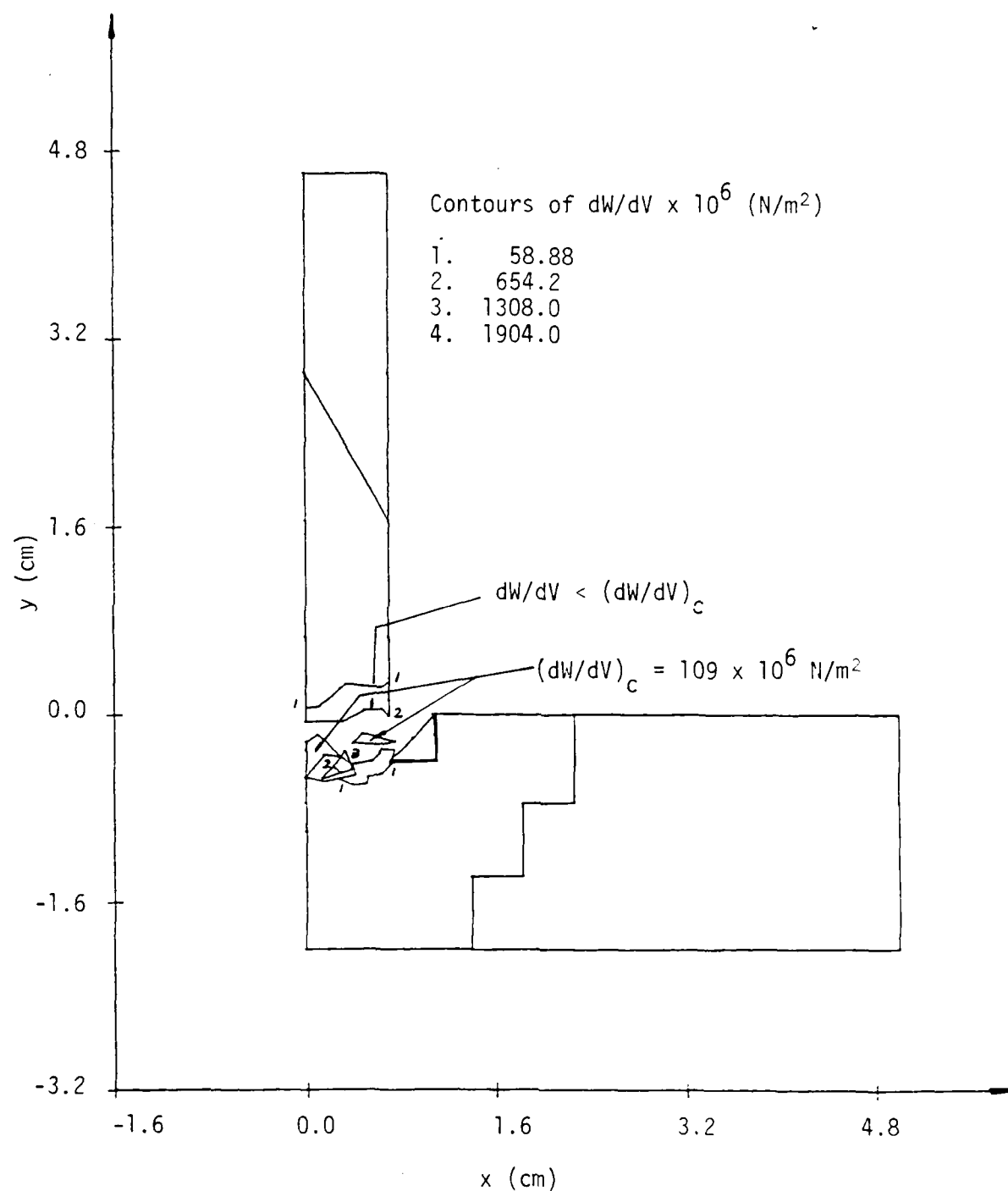


Figure 49. Contours of constant  $dW/dV$  at  $t = 0.764$   $\mu$ sec.

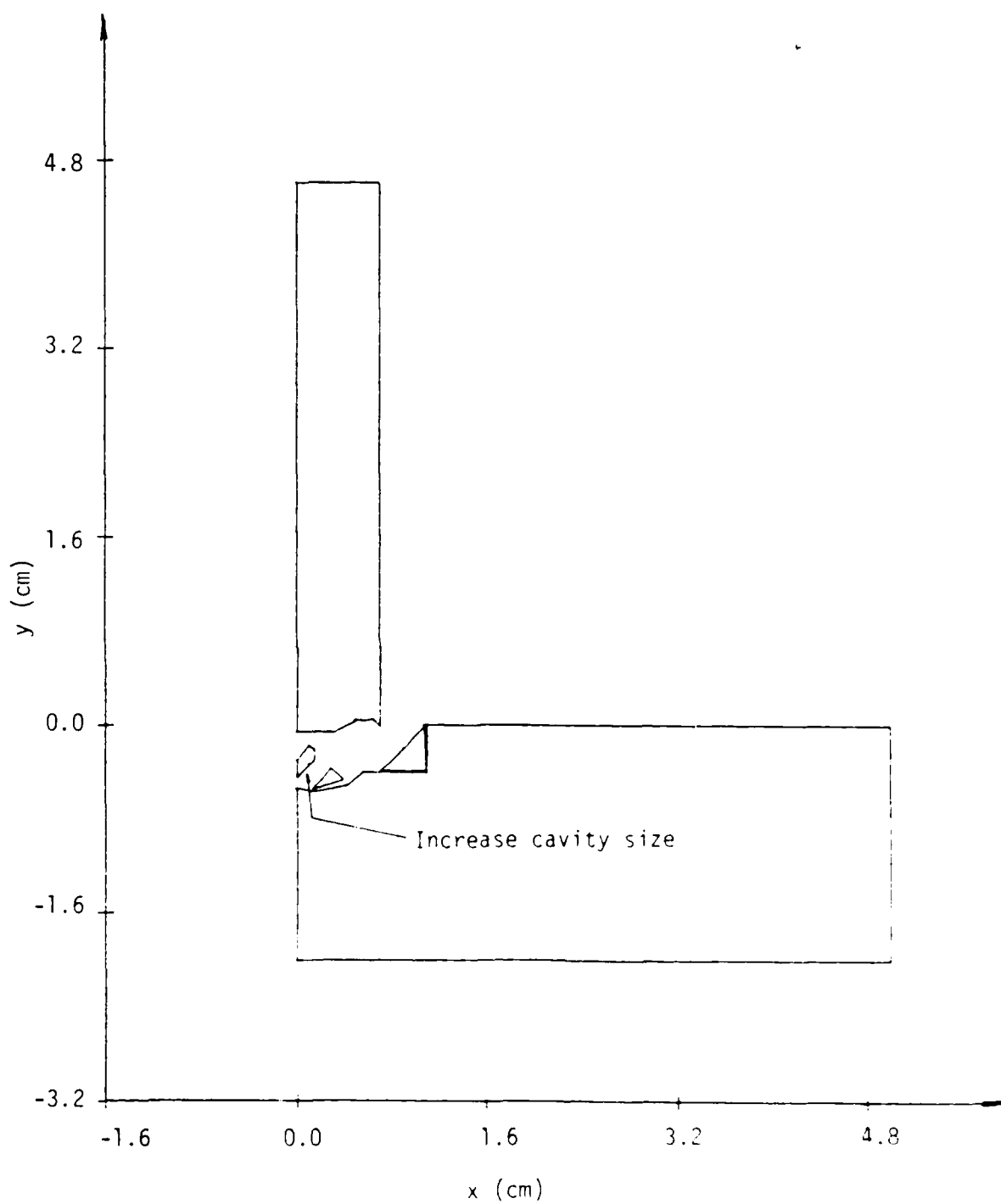


Figure 50. Damage configuration after 0.764 sec.

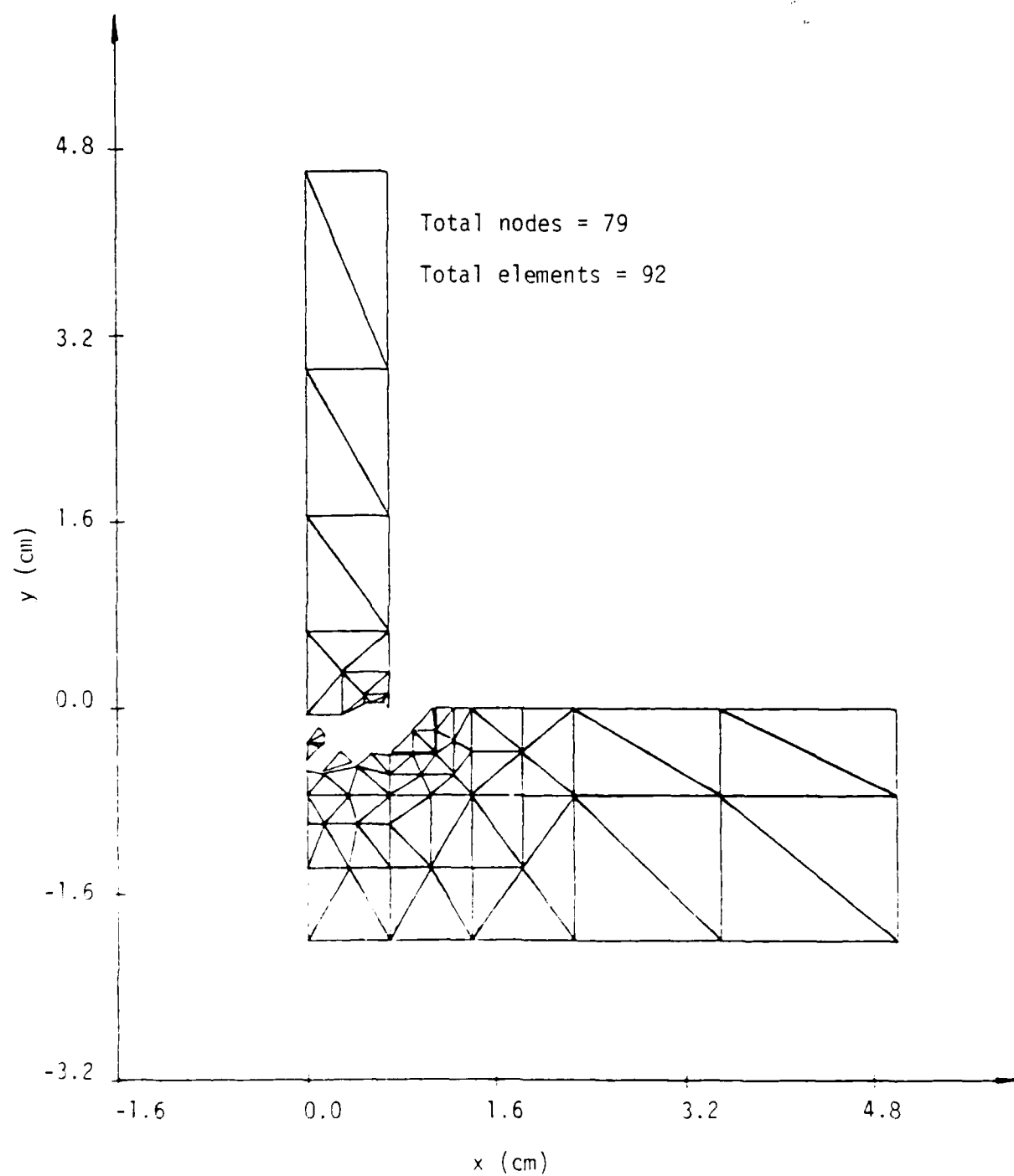


Figure 51. Modified grid pattern after 0.764 .sec.

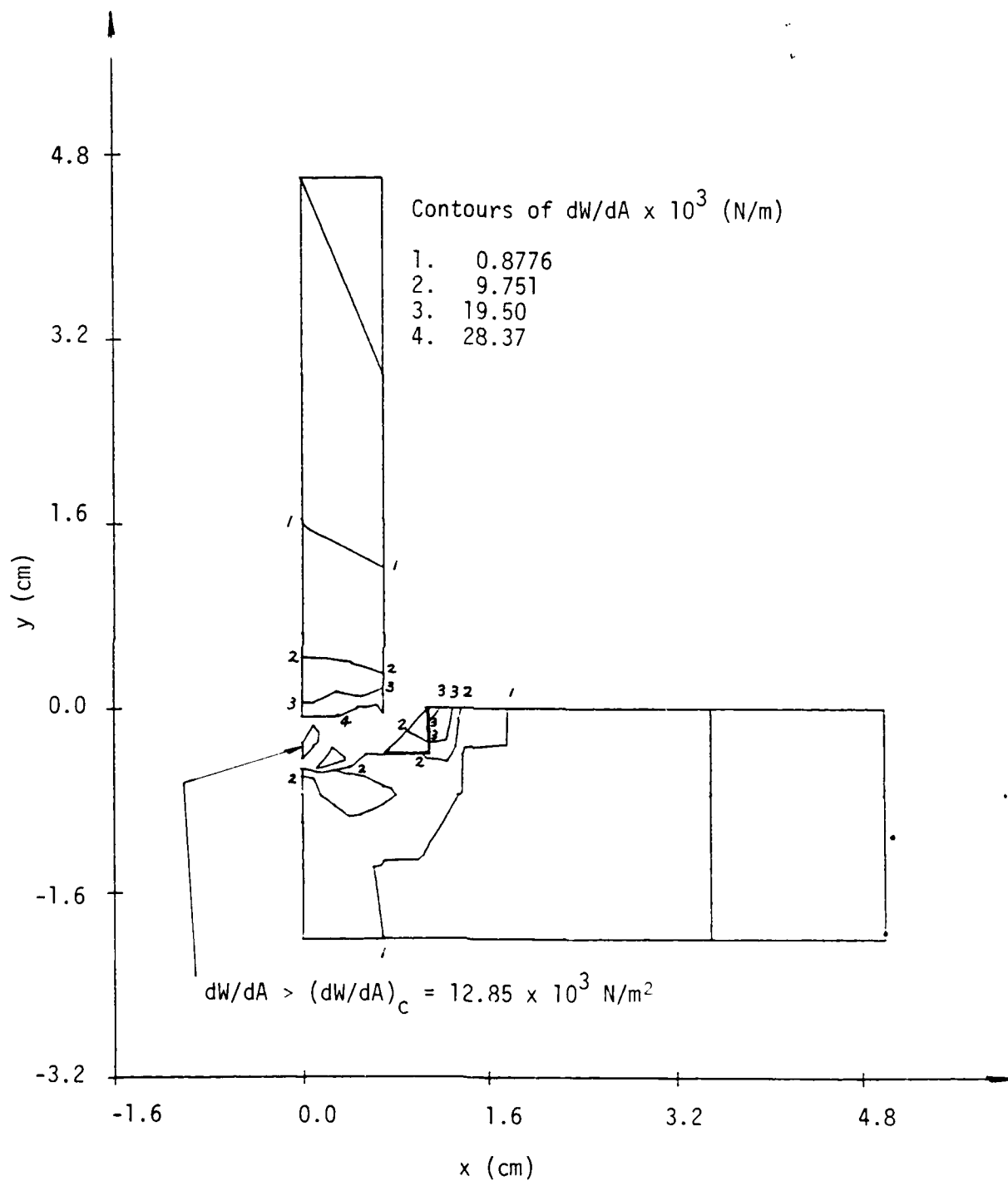


Figure 52. Contours of constant  $dW/dA$  at  $t = 0.869 \text{ usec.}$



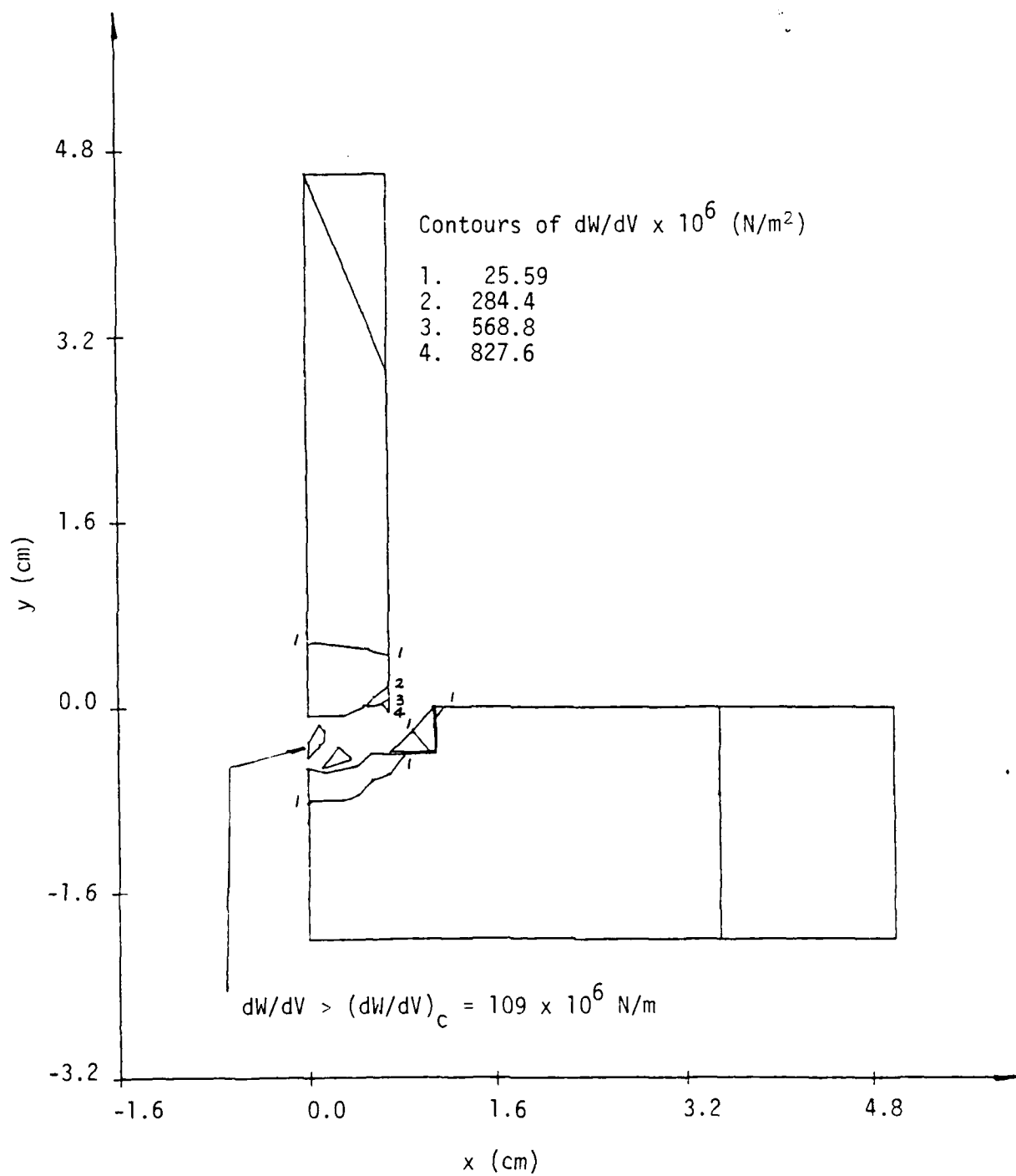


Figure 53. Contours of constant  $dW/dV$  at  $t = 0.869$   $\mu$ sec.

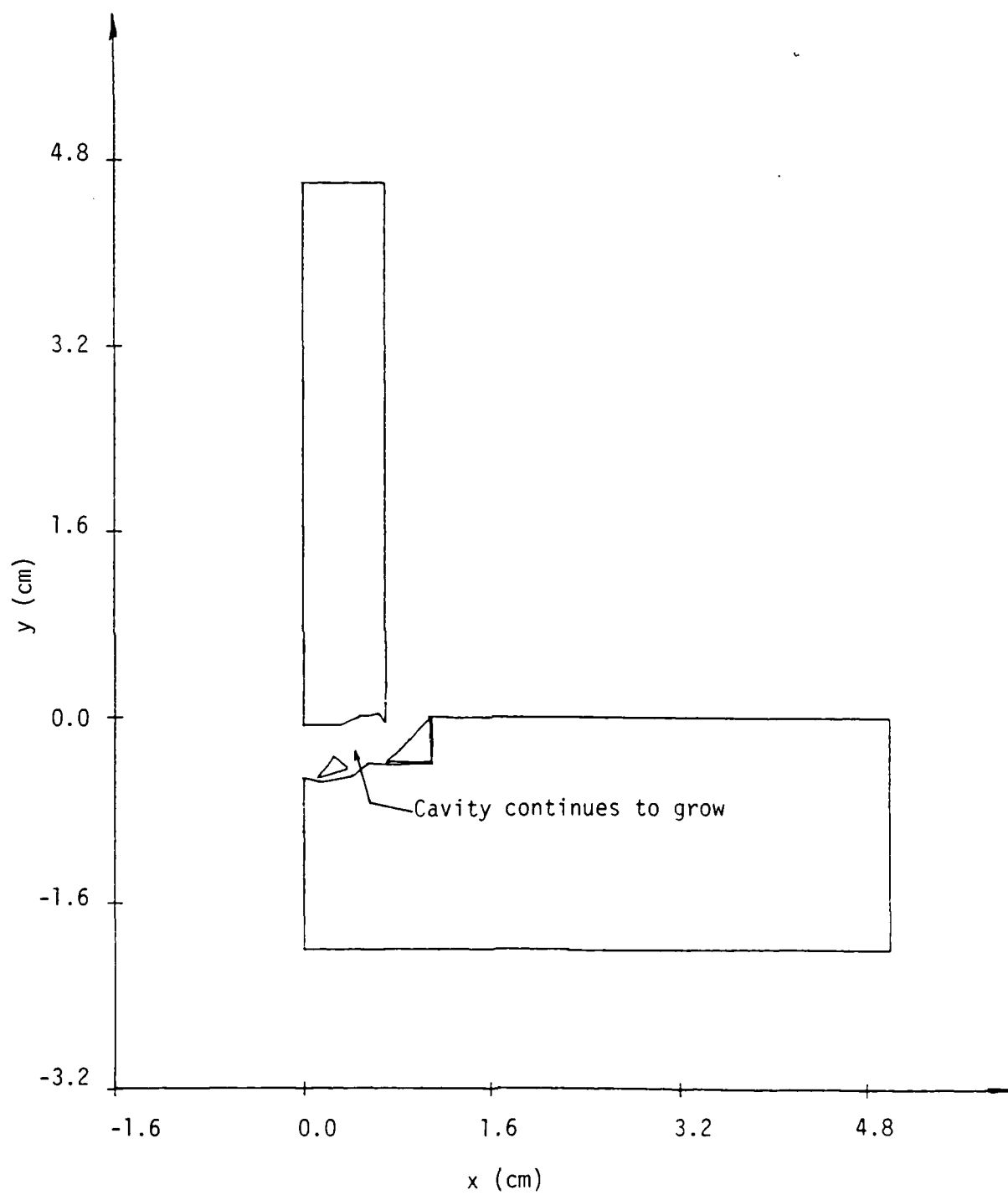


Figure 54. Fragmentation pattern after 0.869  $\mu$ sec.

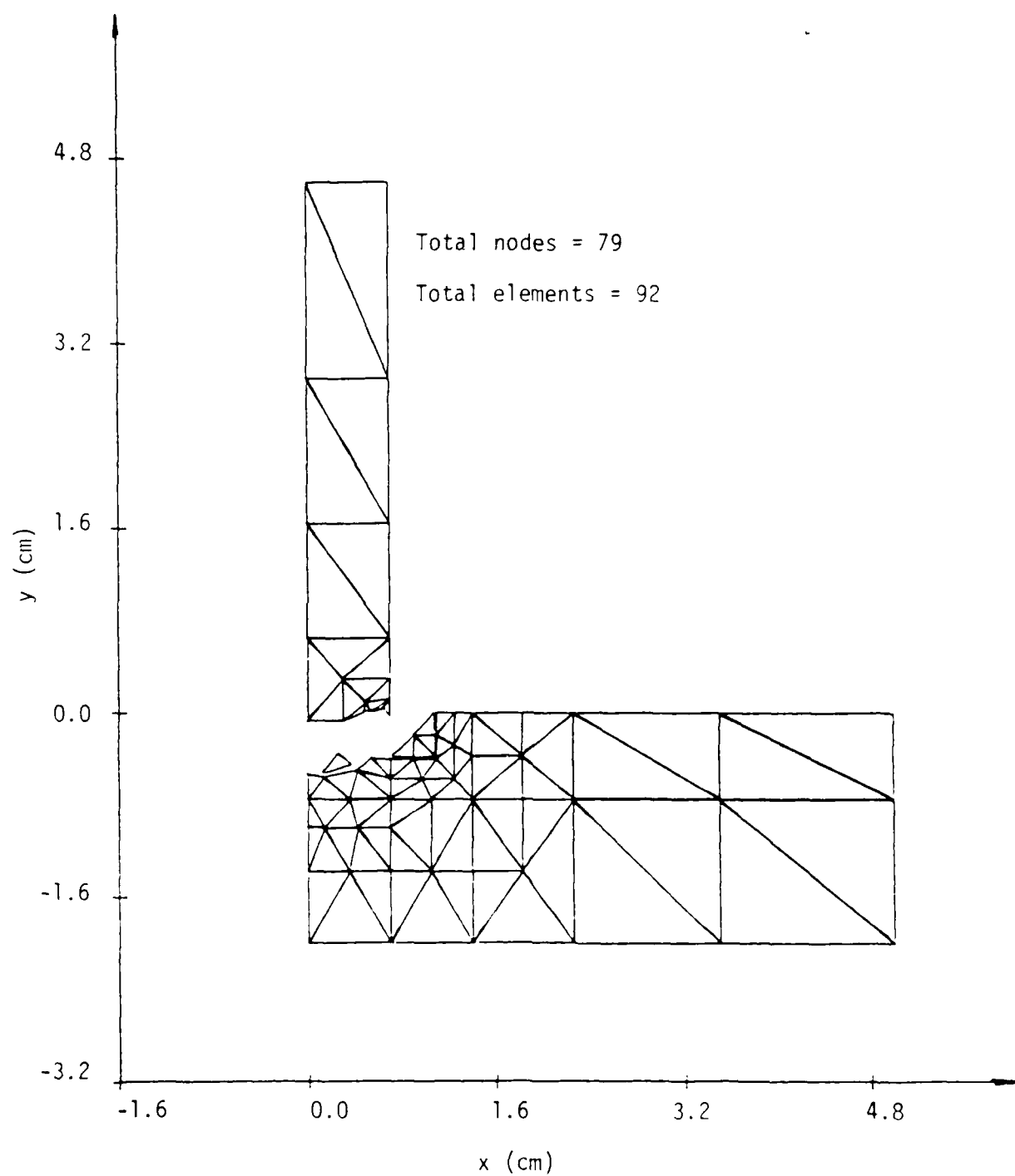


Figure 55. Damage pattern regrided after 0.869 msec.

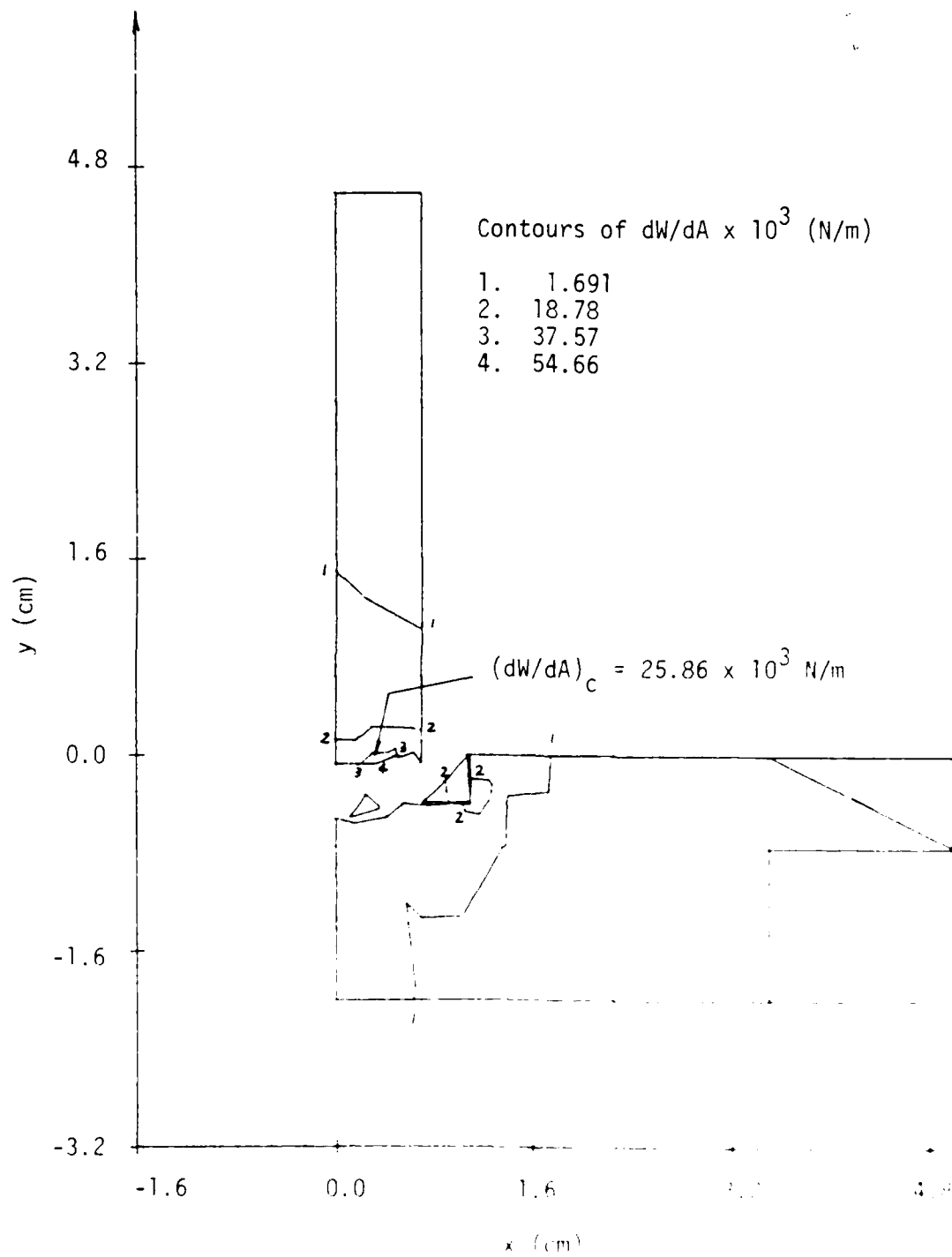


Figure 56. Contours of constant  $dW/dA$  at  $t = 0.1$  sec

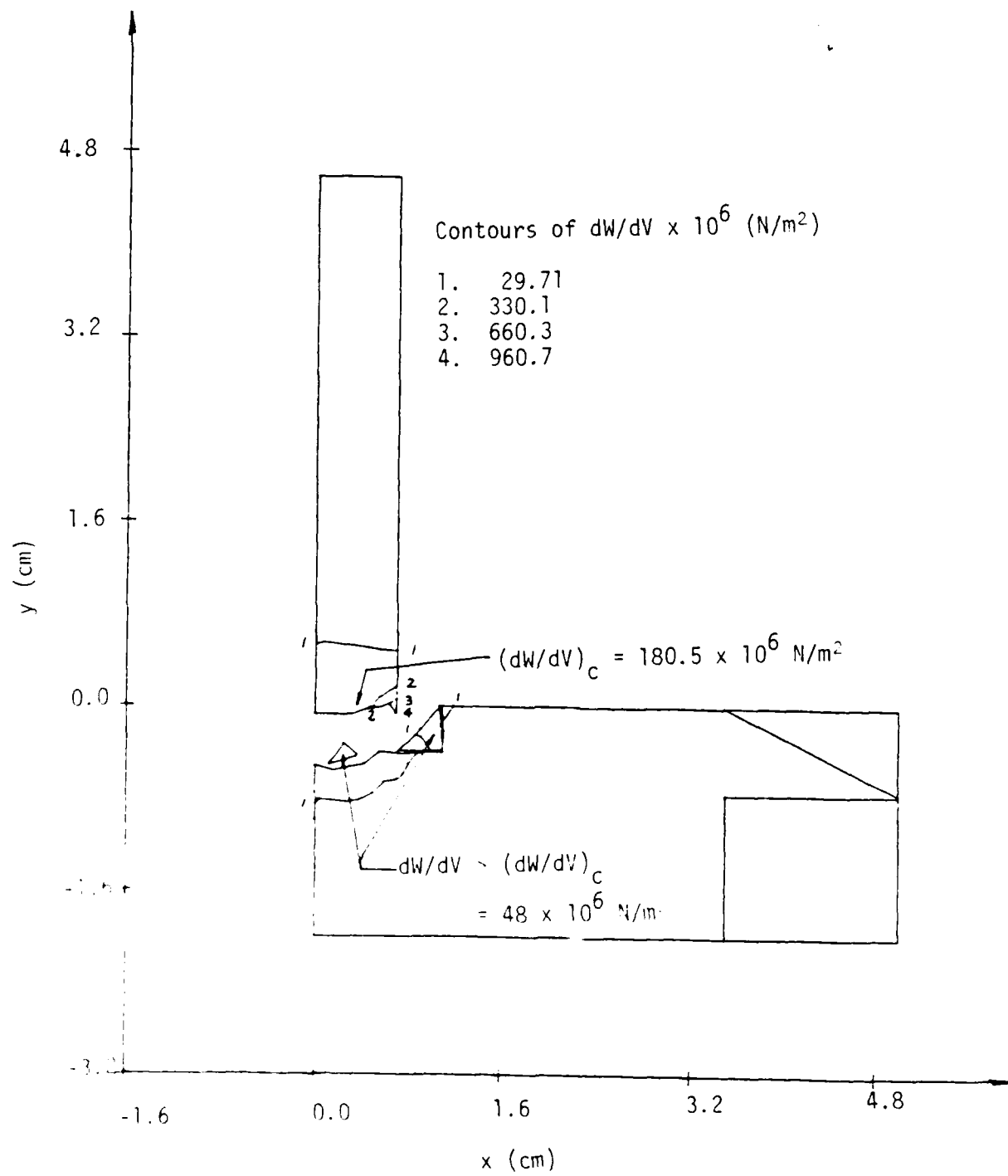


Figure 57. Contours of constant  $dW/dV$  at  $t = 0.924$   $\mu$ sec.

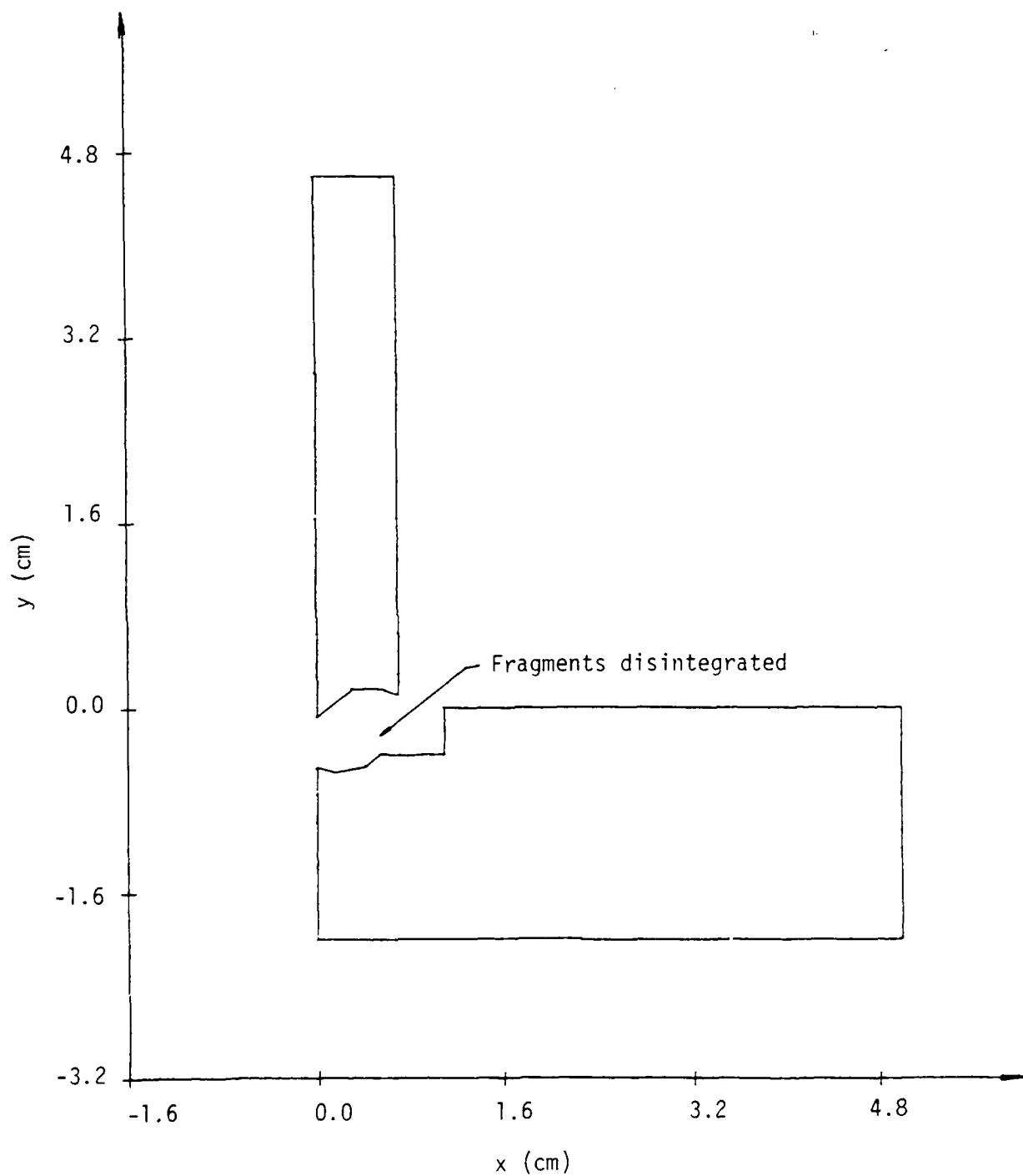


Figure 58. Cavity configuration after 0.924  $\mu\text{sec}$ .

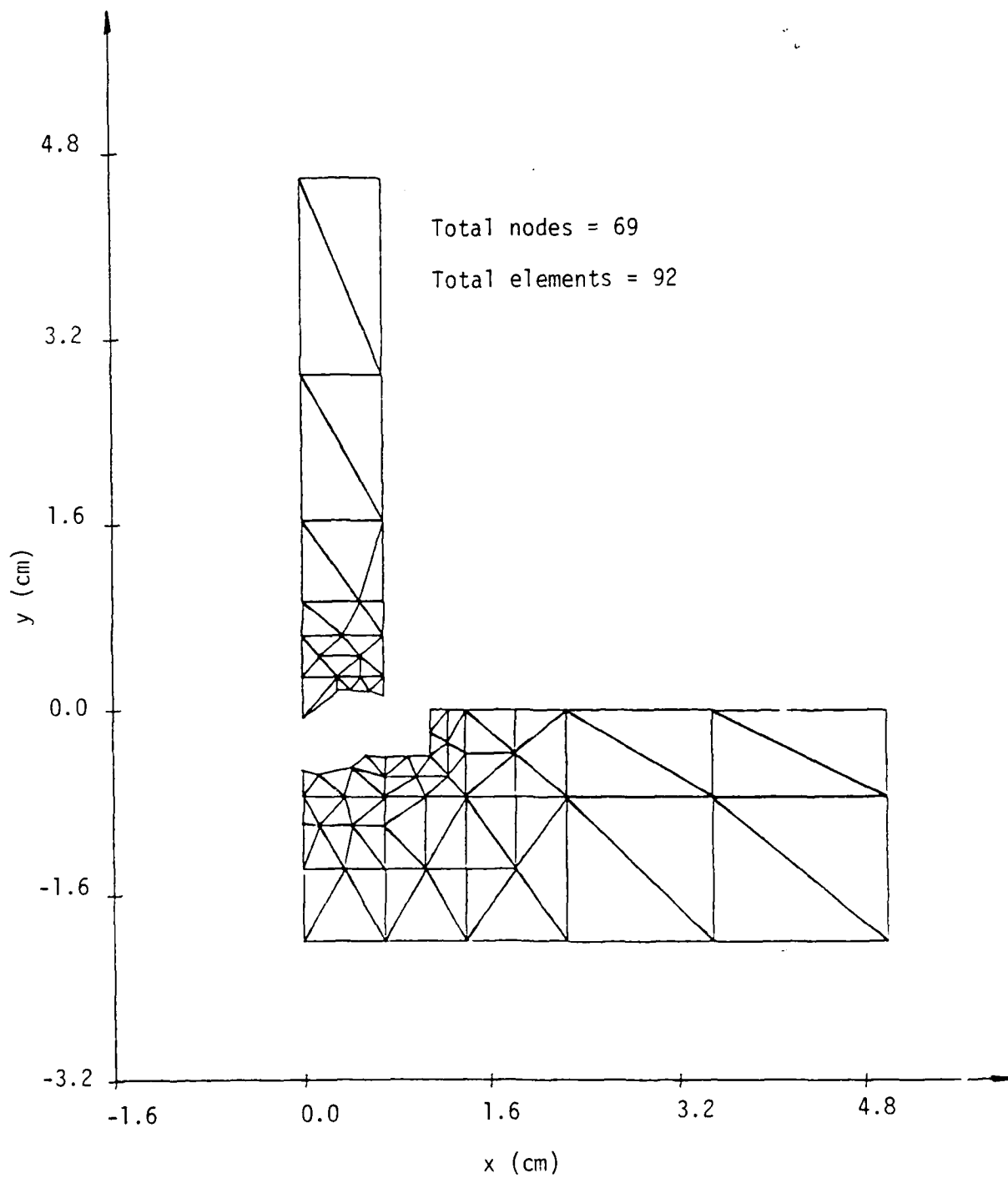


Figure 59. Projectile and target grid pattern at  $t = 0.924 \mu\text{sec}$ .

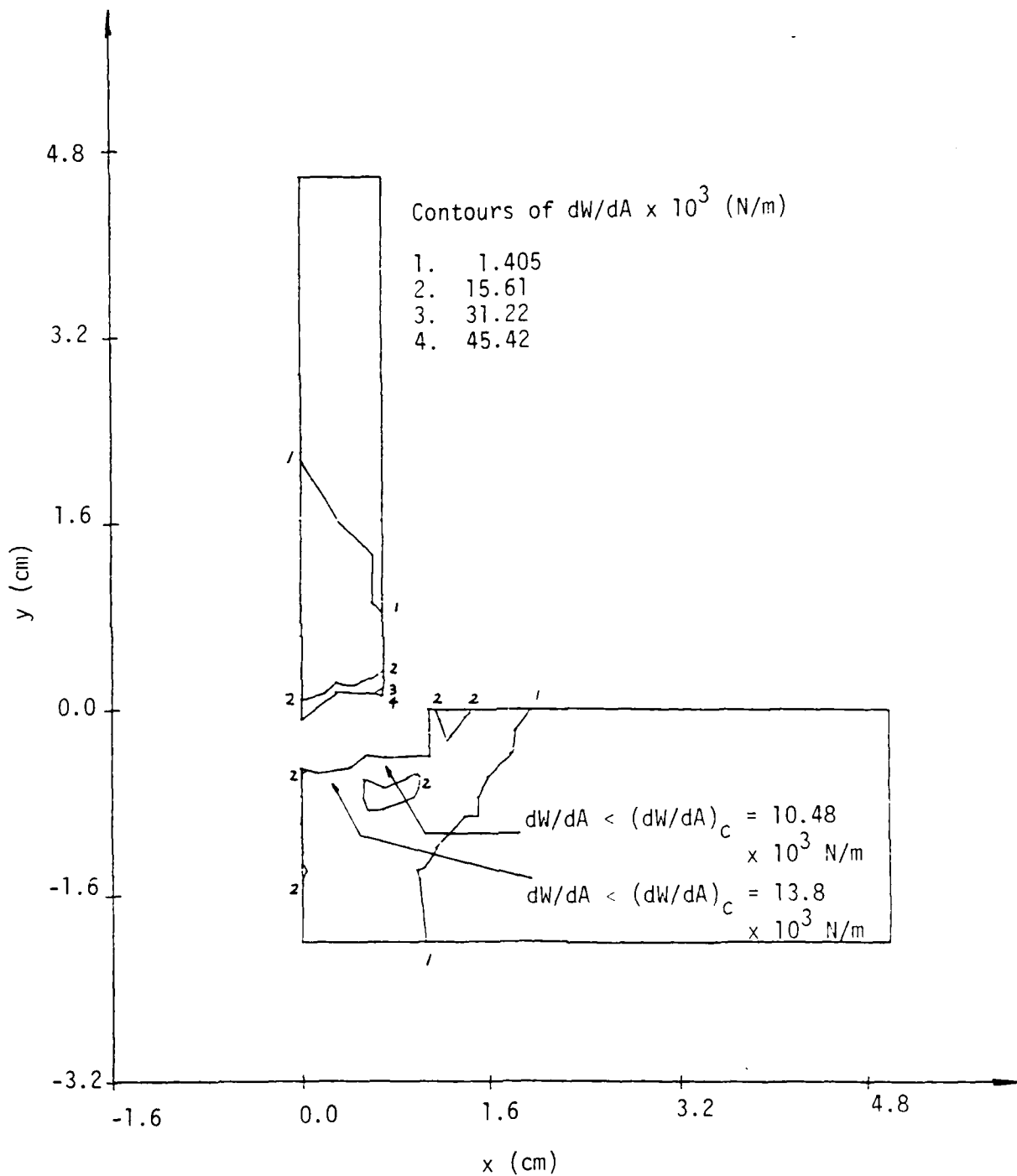


Figure 60. Contours of constant  $dW/dA$  at  $t = 1.024 \mu\text{sec}$ .



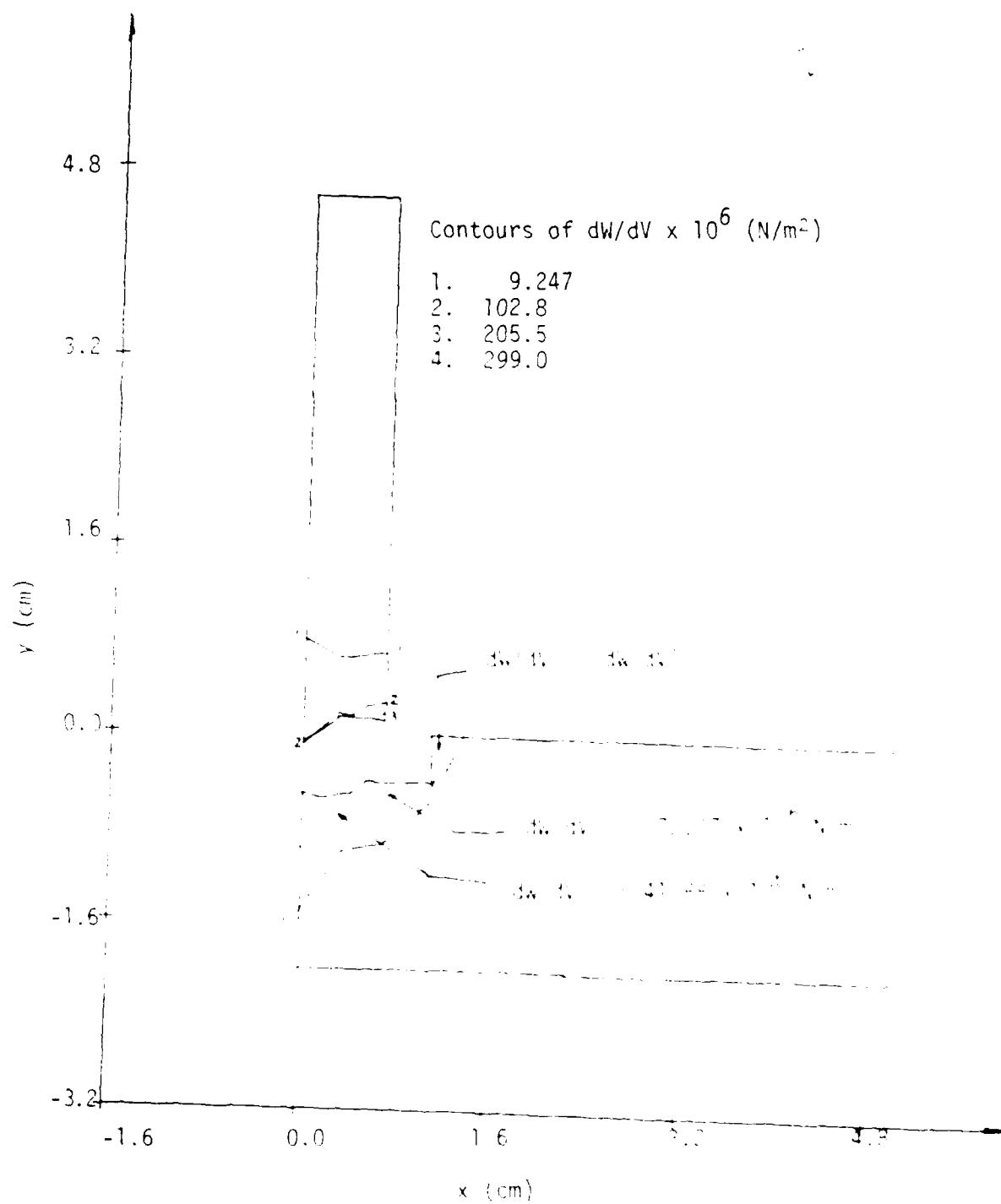


Figure 61. Contours of constant  $dW/dV$  at  $t = 1.024$  sec.

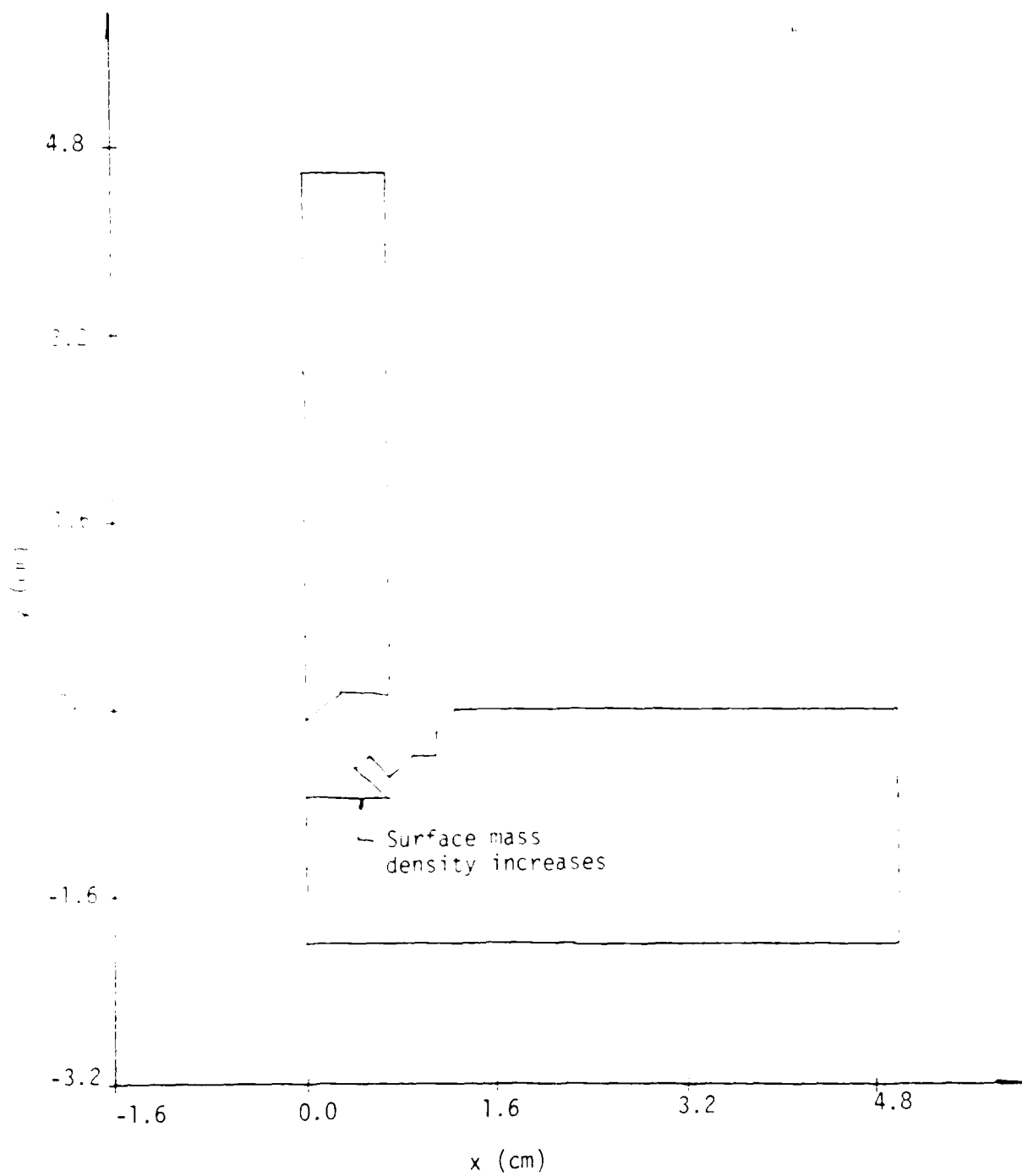


Figure 62. Zig-zag cavity configuration at 1.024  $\mu\text{sec}$ .

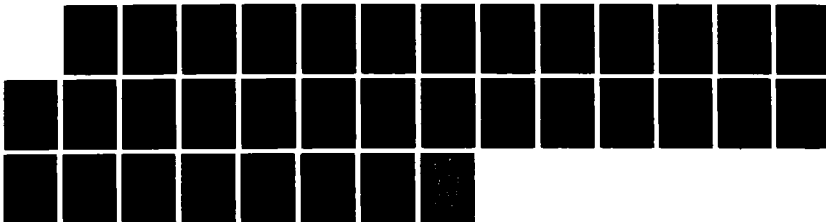
NO-A191 182

FRAGMENTATION AND PLUGGING FAILURE OF PROJECTILE/TARGET 2/2  
SYSTEM(U) LEHIGH UNIV BETHLEHEM PA INST OF FRACTURE AND  
SOLID MECHANICS G C SIM ET AL. MAR 87 MTL-TR-87-18

UNCLASSIFIED DAAG46-85-K-0011

F/G 15/10

NL





1.0



1.1



1.25



2.8



3.15



3.5



4.0



4.5



5.0



5.6



6.3



7.1



8.0

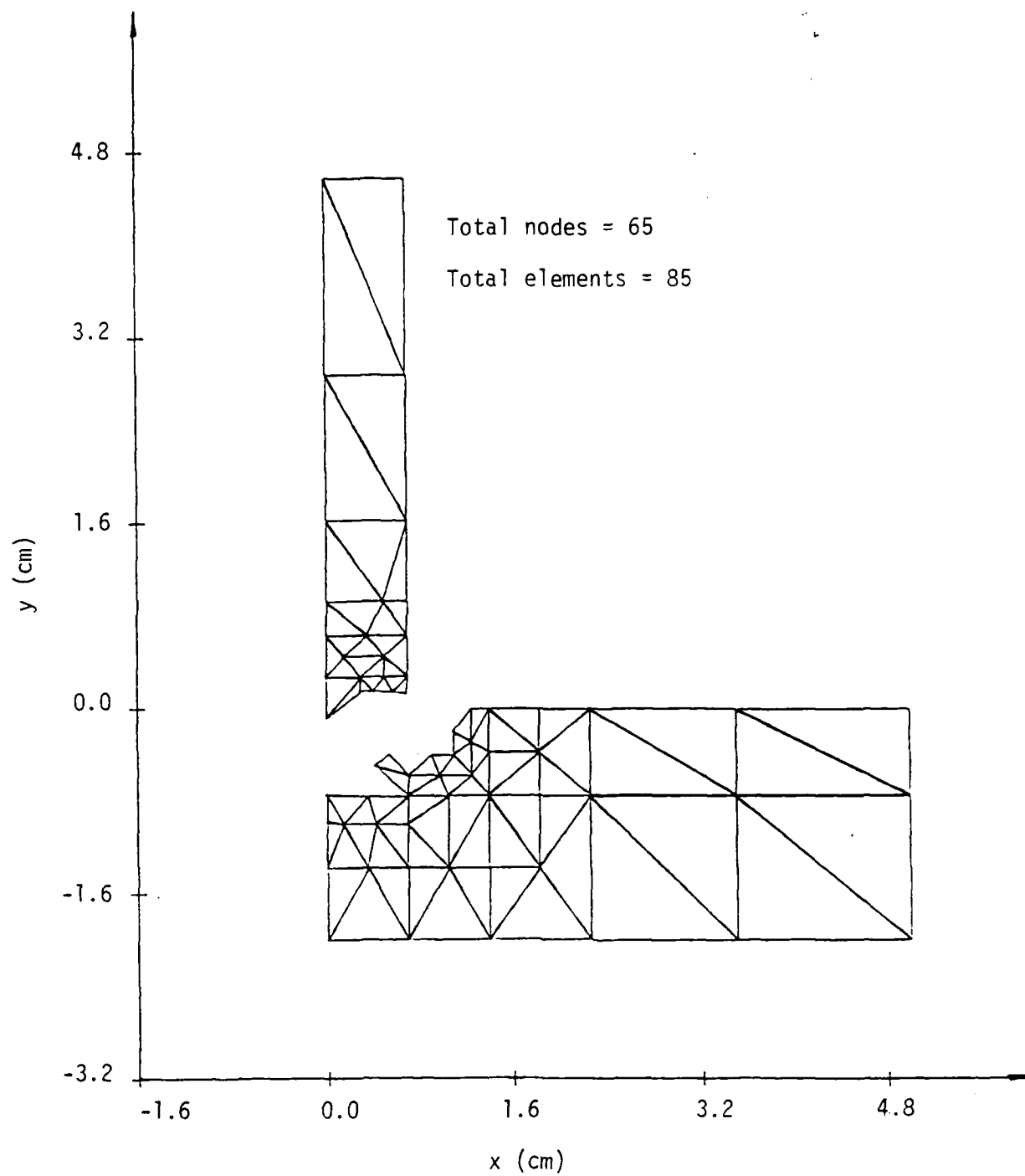


Figure 63. Grid pattern of fractured surfaces at  $t = 1.024 \mu\text{sec}$ .

in Figure 64 exceeded  $(dW/dV)_c$ . The volume energy density contours at  $t = 1.224$   $\mu\text{sec}$  in Figure 65, however, have increased beyond  $(dW/dV)_c$  at several locations. This results in additional fragmentation as displayed in Figures 66 and 67. Further calculations made for  $t = 1.245$   $\mu\text{sec}$  revealed no significant change except for the disintegration of the fragment that is in point contact with the fractured surface.

The cavity depth in the target at  $t = 1.259$   $\mu\text{sec}$  is approximately one-half of the total thickness. Even though  $dW/dA$  is relatively low as indicated in Figure 68, the volume energy density  $dW/dV$  in several places is still above critical. Failure by fracture occurs at  $(dW/dV)_c = 32.22 \times 10^6$   $\text{N/m}^2$  in the target and  $(dW/dV)_c = 288.37 \times 10^6$   $\text{N/m}^2$  in the projectile as shown in Figure 69. A large portion of the material breaks away from the projectile which continues to travel toward the target as a rigid body. This is illustrated in Figure 70. Figure 71 displays the revised grid pattern for the next time increment of calculation. As the projectile comes in contact with the trapped fragment at the interface,  $dW/dA$  remained relatively low everywhere. This is illustrated in Figure 72 for  $t = 1.264$   $\mu\text{sec}$ . The fragment is crushed as a result of the high volume energy density surpassing the critical value of  $129.46 \times 10^6$   $\text{N/m}$  indicated in Figure 73. A gap between the projectile and target is again created and shown in Figure 74. The corresponding finite element grid pattern in Figure 75 is now simplified and contains only 61 elements and 49 nodes. Once the projectile catches up to the cavity in Figure 76, the local surface energy density intensifies and rises above  $(dW/dV)_c = 29.59 \times 10^3$   $\text{N/m}$ . The local volume energy density contours in Figure 77 also attain high values but they are localized. It can be easily seen from the computer output that there exists a  $(dW/dA)_c$  critical path extending from the reentrant corner of the cavity in Figures 76 or 77 to the back side of the target plate. This event is normally referred to as "plugging" where a block of



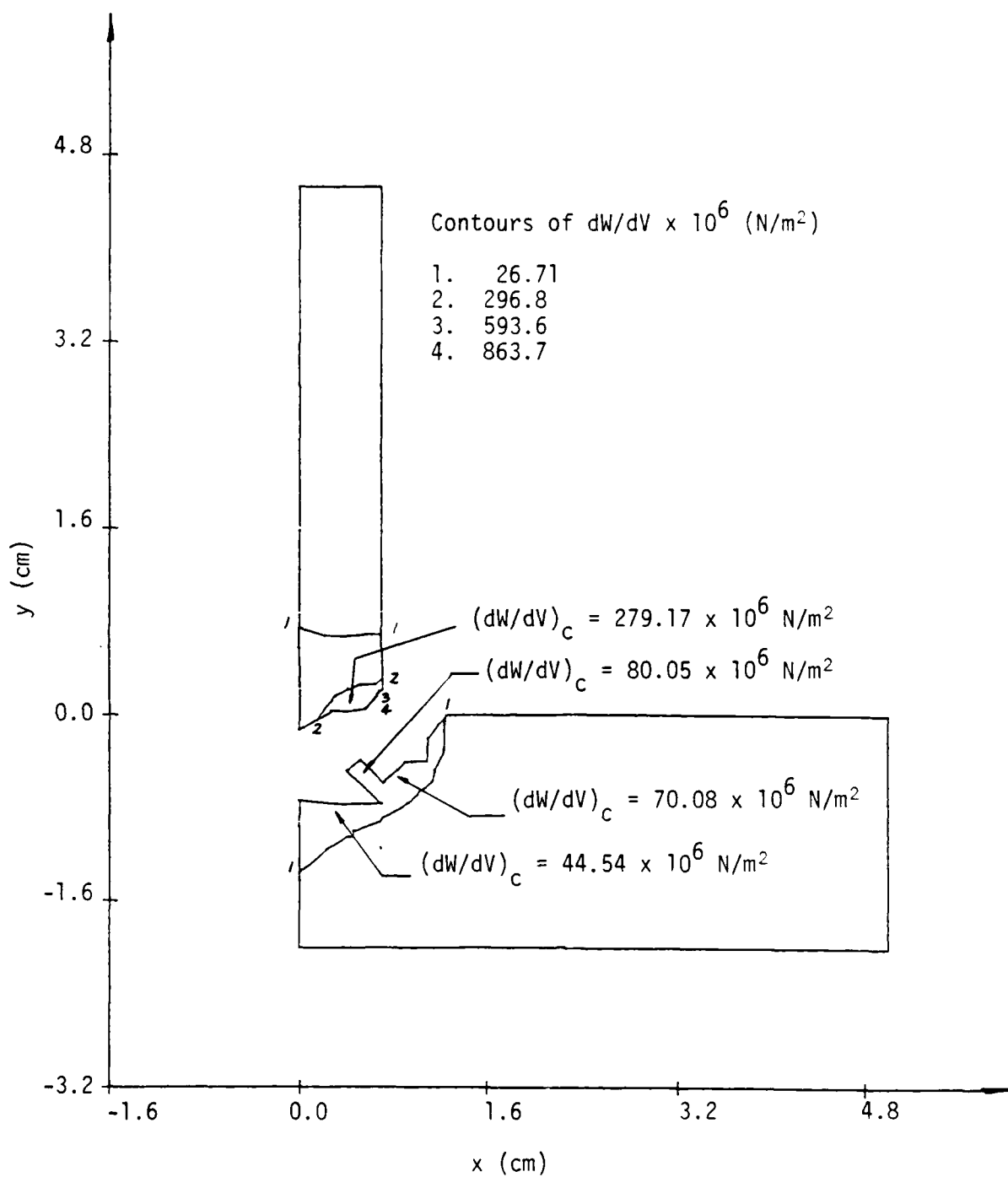


Figure 65. Contours of constant  $dW/dV$  at  $t = 1.224$  usec.



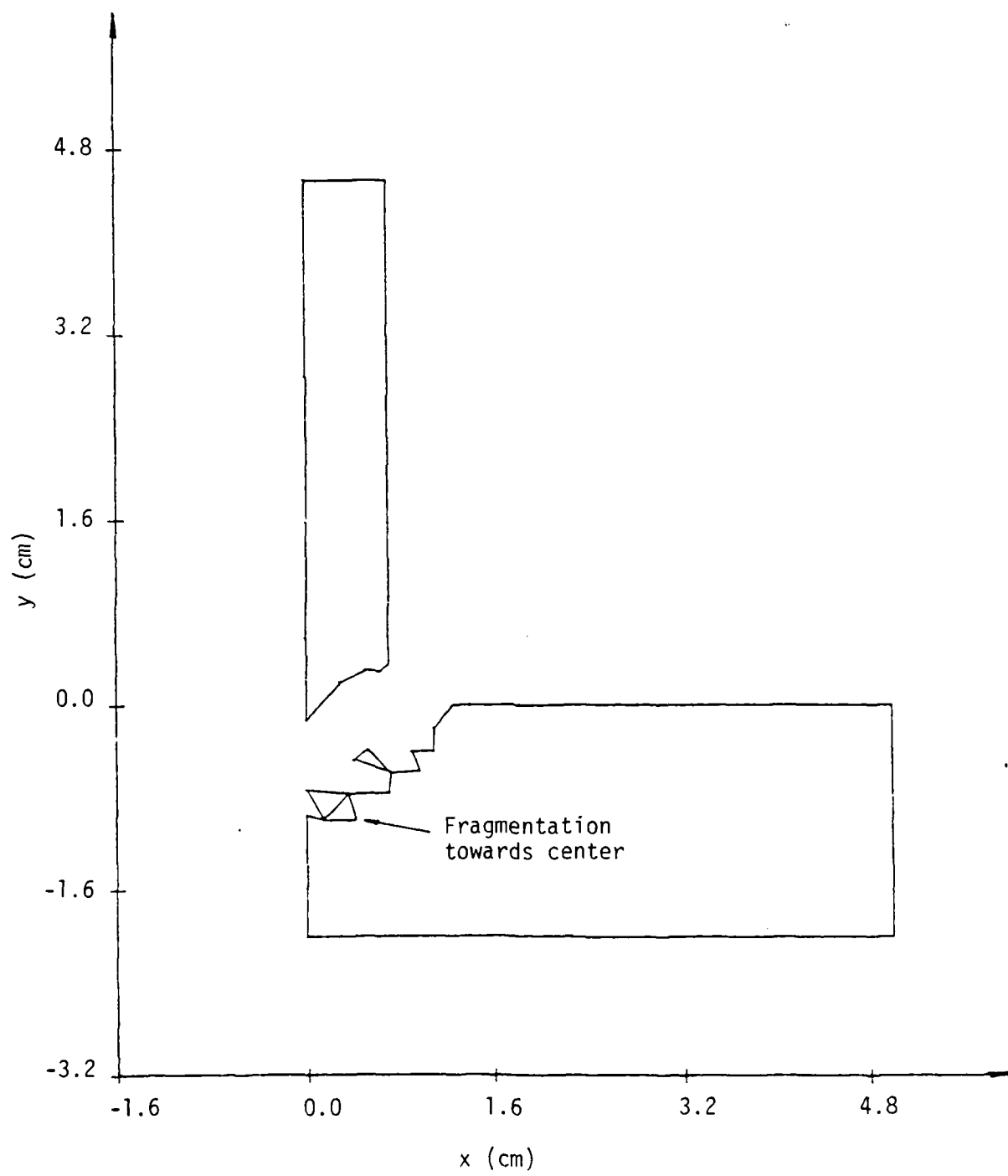


Figure 66. Additional fragmentation at  $t = 1.224 \mu\text{sec}$ .

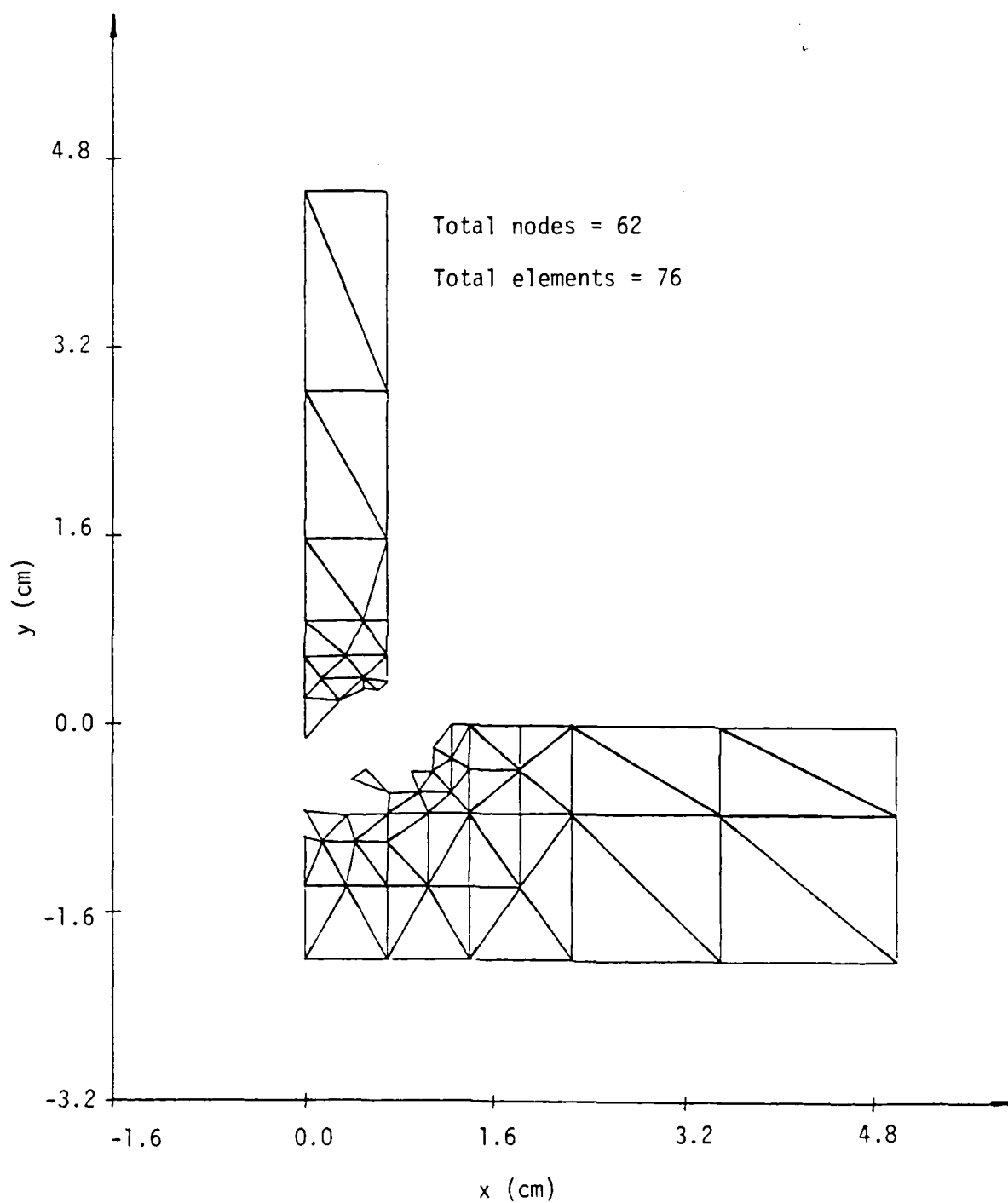


Figure 67. Fragmentation pattern at  $t = 1.224 \mu\text{sec}$ .

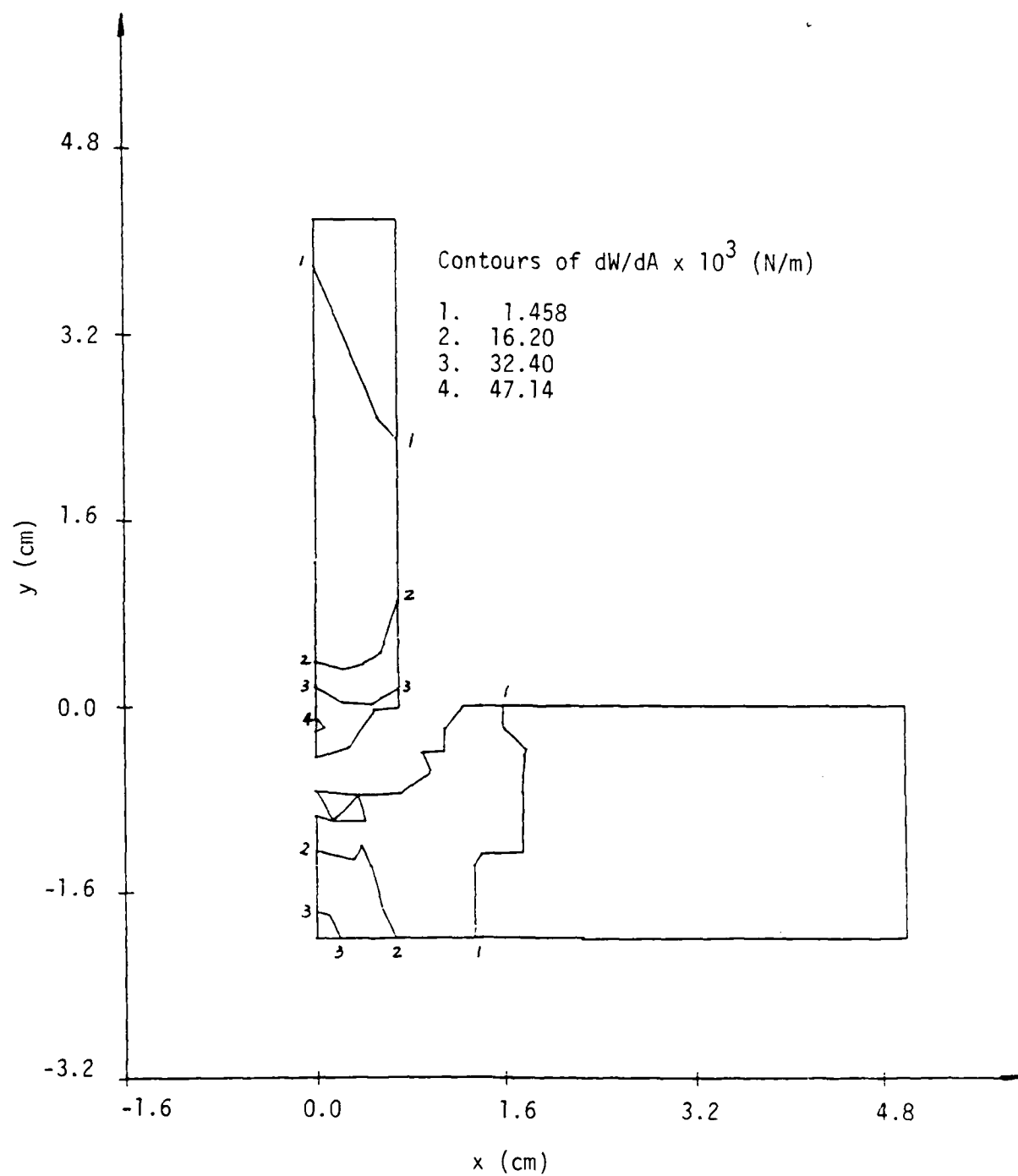


Figure 68. Contours of constant  $dW/dA$  at  $t = 1.259 \mu\text{sec}$ .

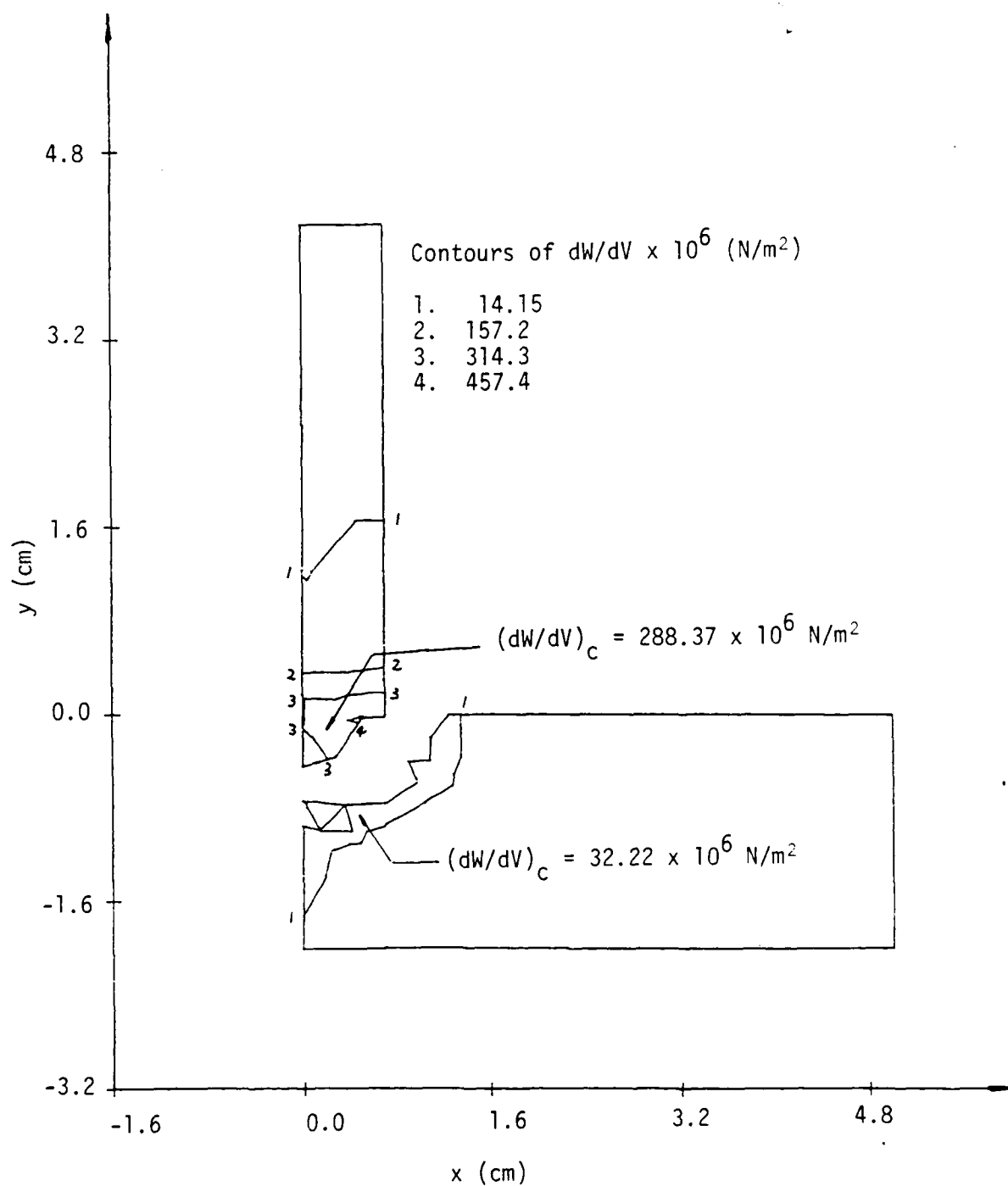


Figure 69. Contours of constant  $dW/dV$  at  $t = 1.259 \mu\text{sec}$ .

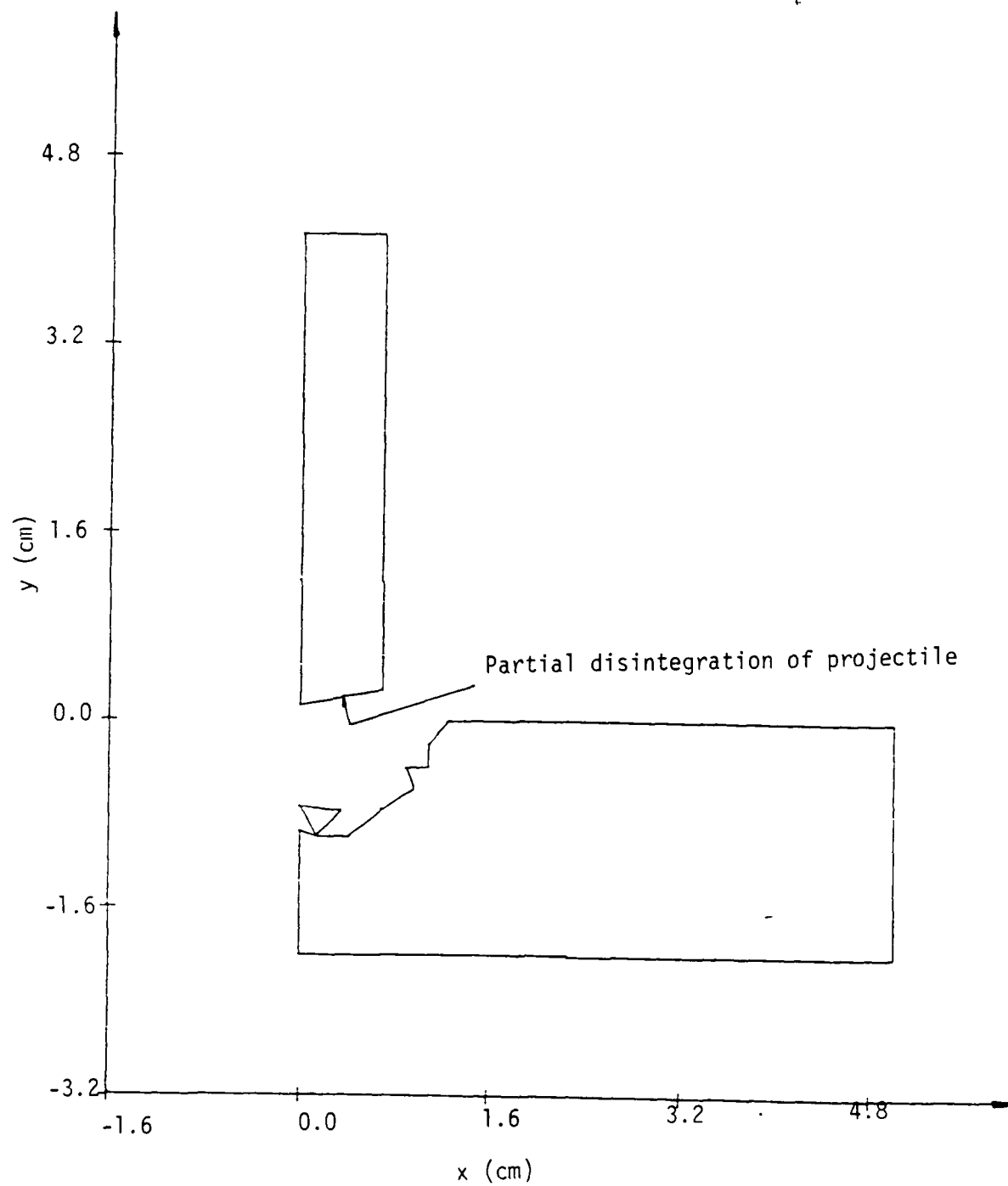


Figure 70. Fragmented projectile/target system at  $t = 1.259 \text{ usec}$ .

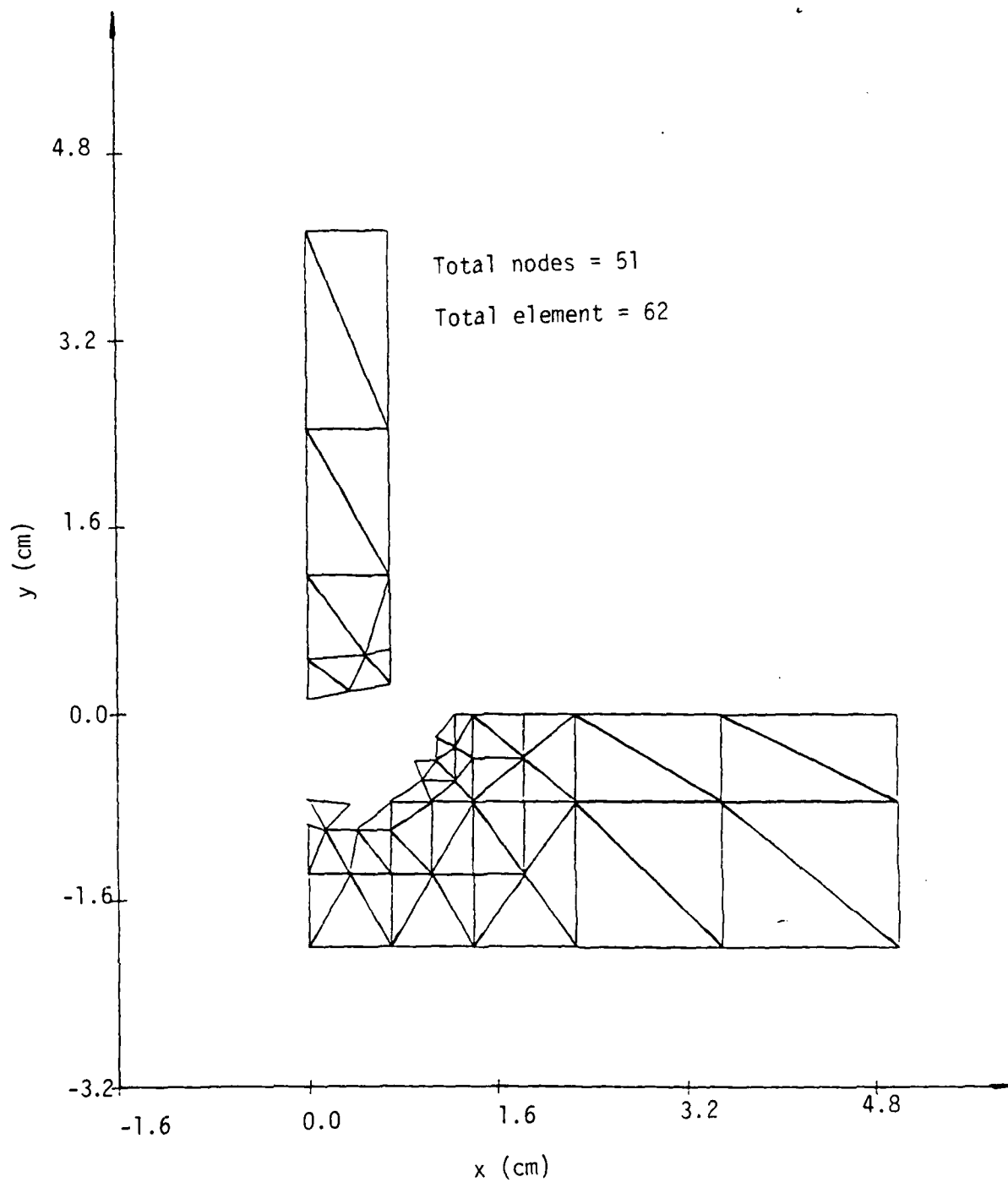


Figure 71. Grid pattern at  $t = 1.259 \text{ } \mu\text{sec.}$

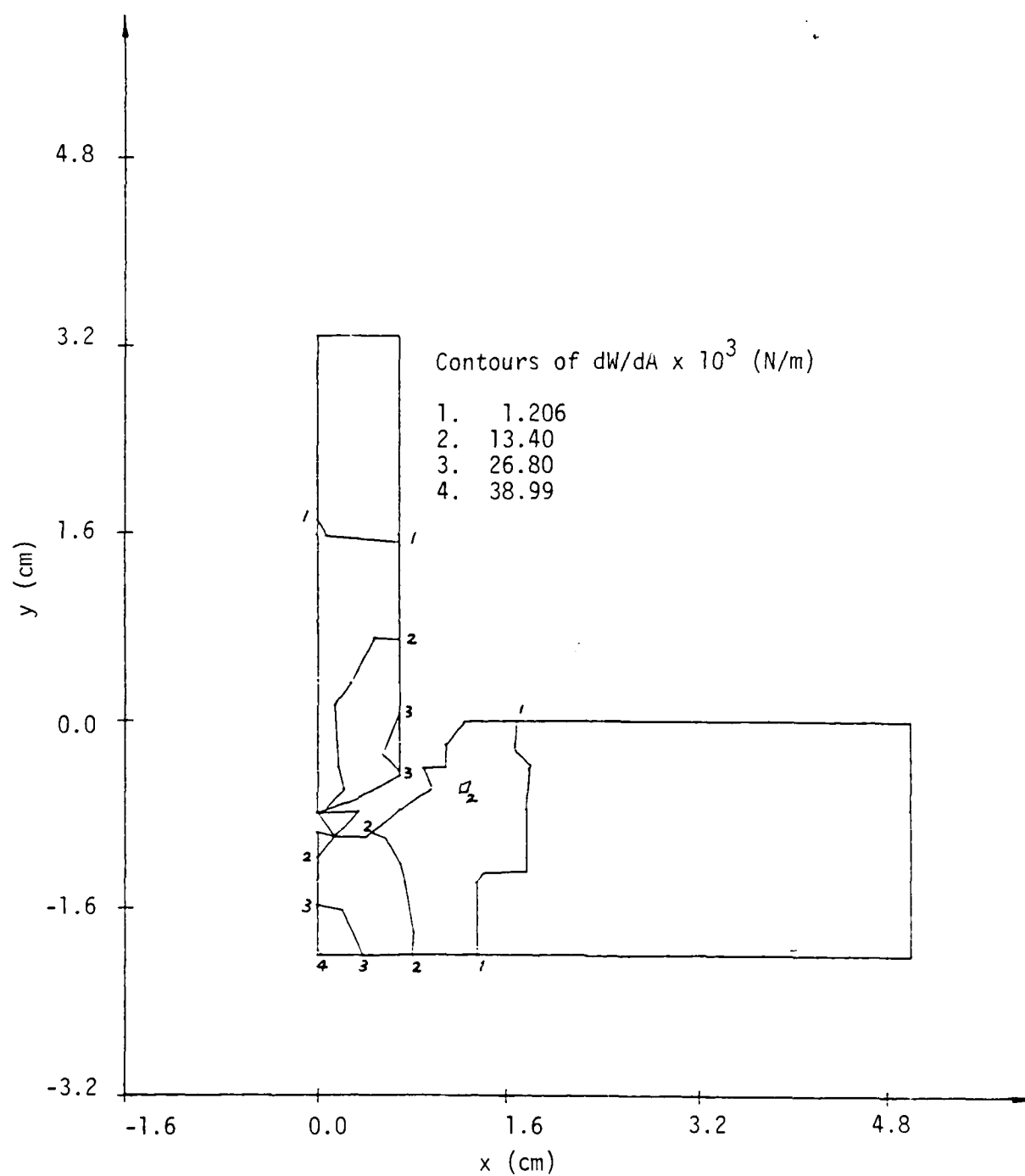


Figure 72. Contours of constant  $dW/dA$  at  $t = 1.264$  usec.

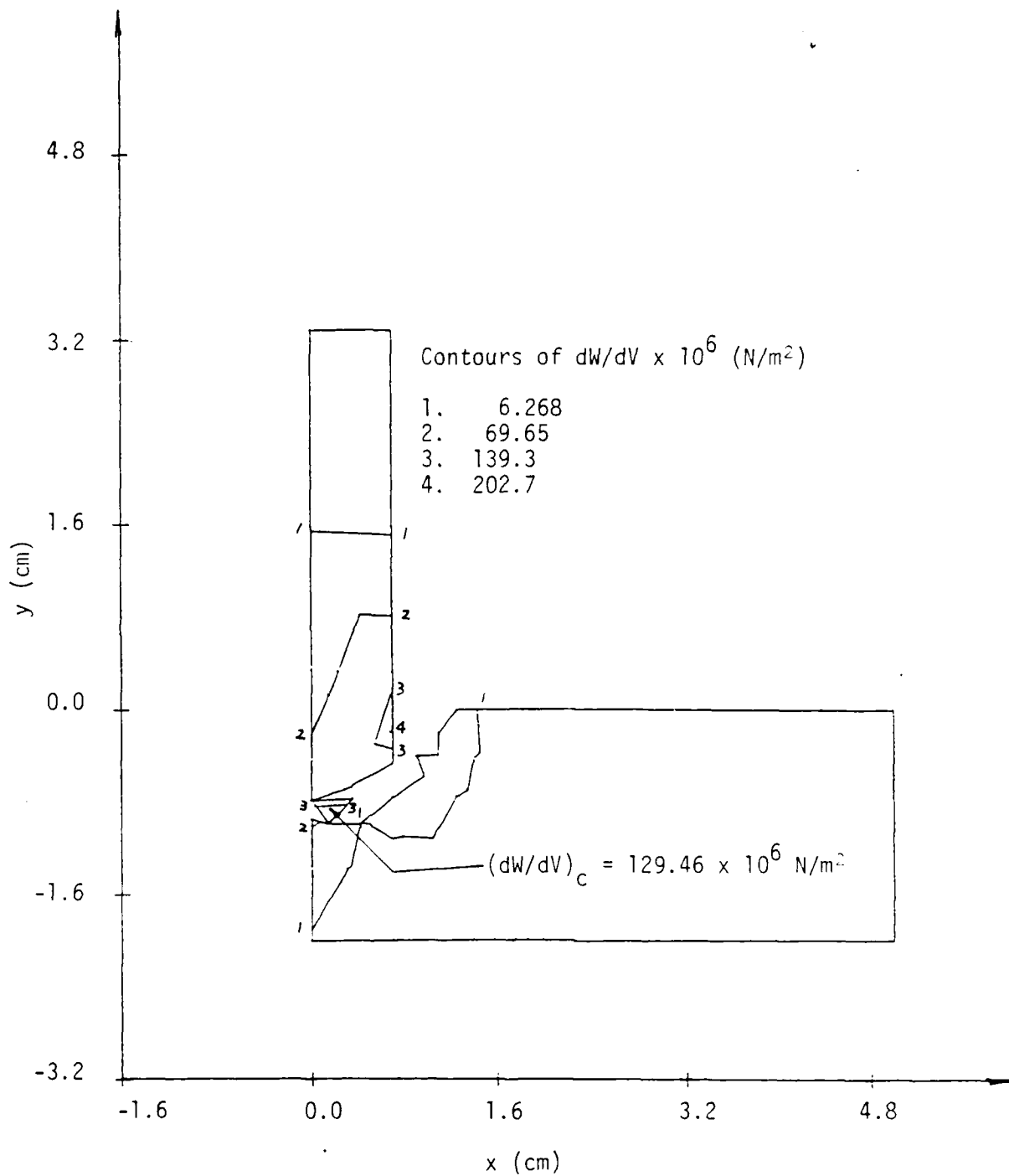


Figure 73. Contours of constant  $dW/dV$  at  $t = 1.264$   $\mu$ sec.



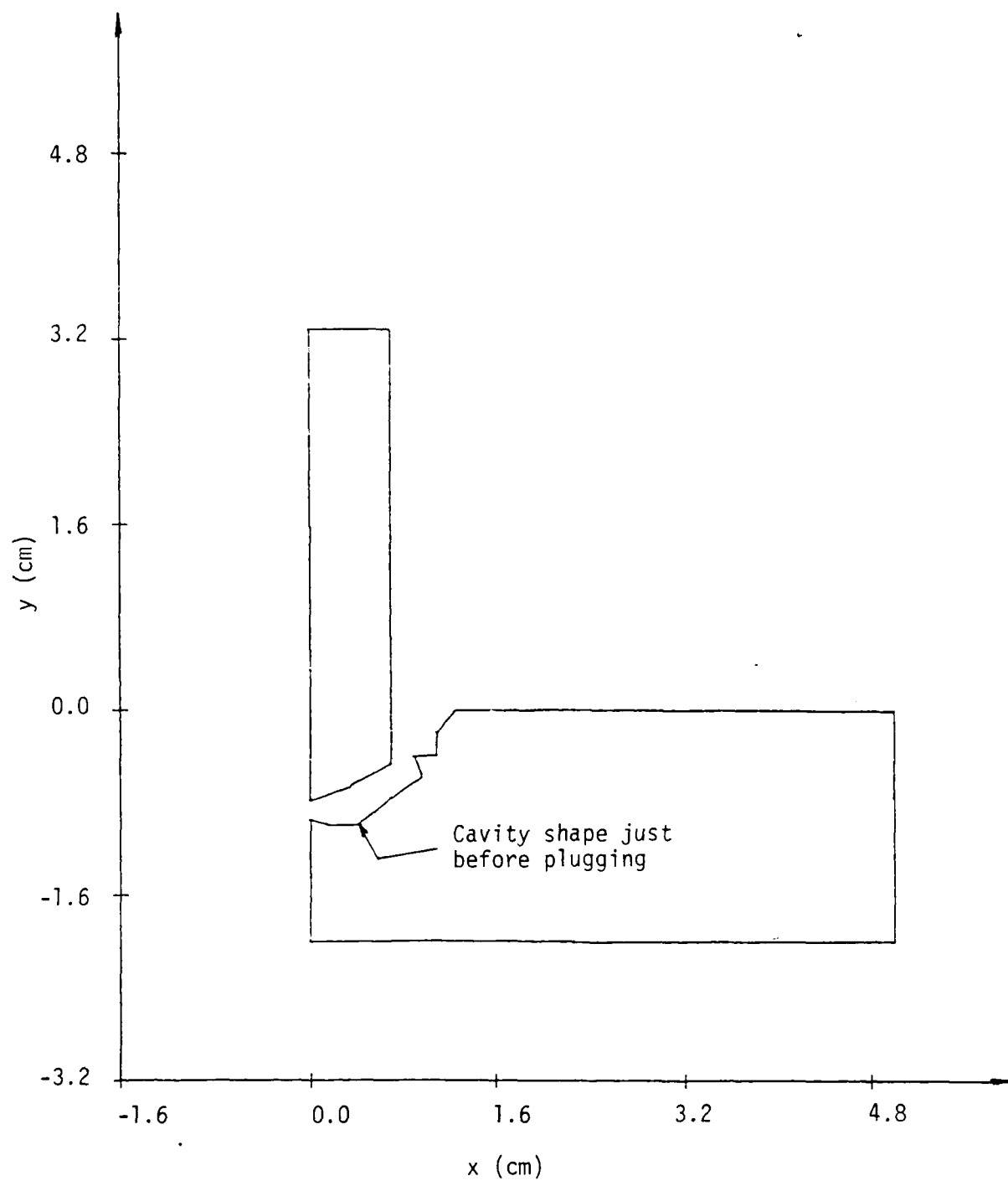


Figure 74. Damage pattern at  $t = 1.264 \mu\text{sec}$ .

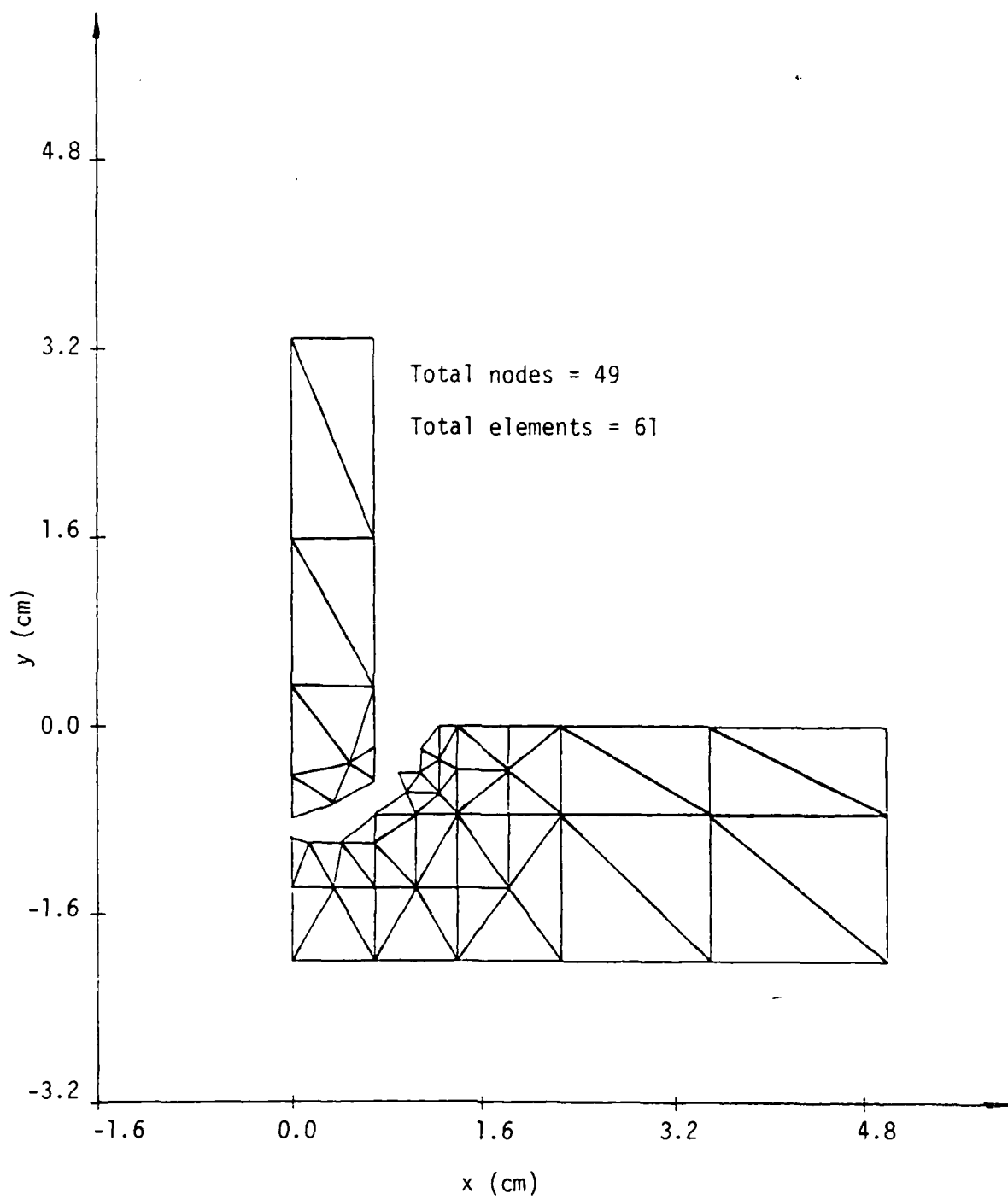


Figure 75. Finite element grid pattern at  $t = 1.264 \text{ usec.}$

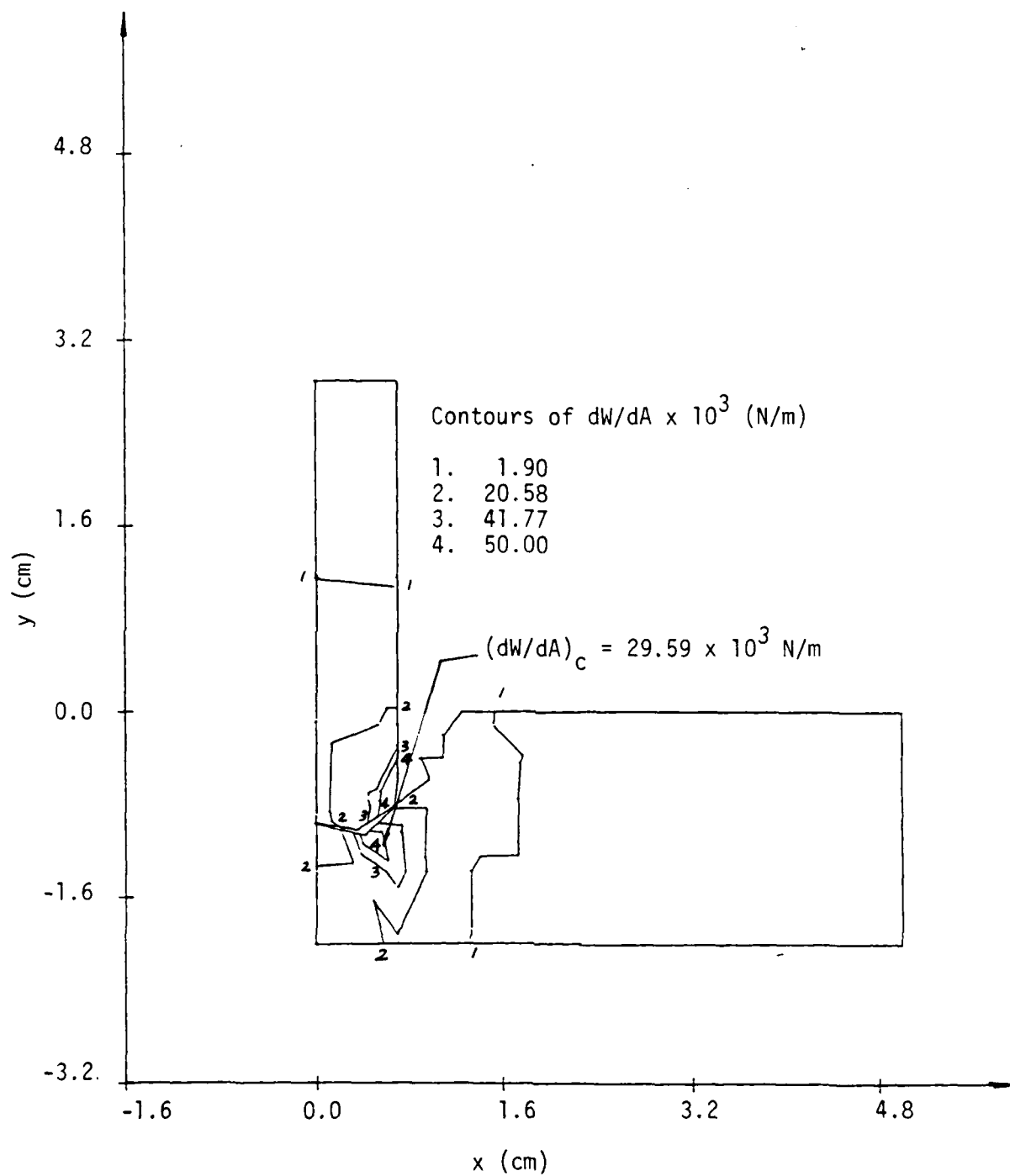


Figure 76. Contours of constant  $dW/dA$  at  $t = 1.265 \mu\text{sec}$ .

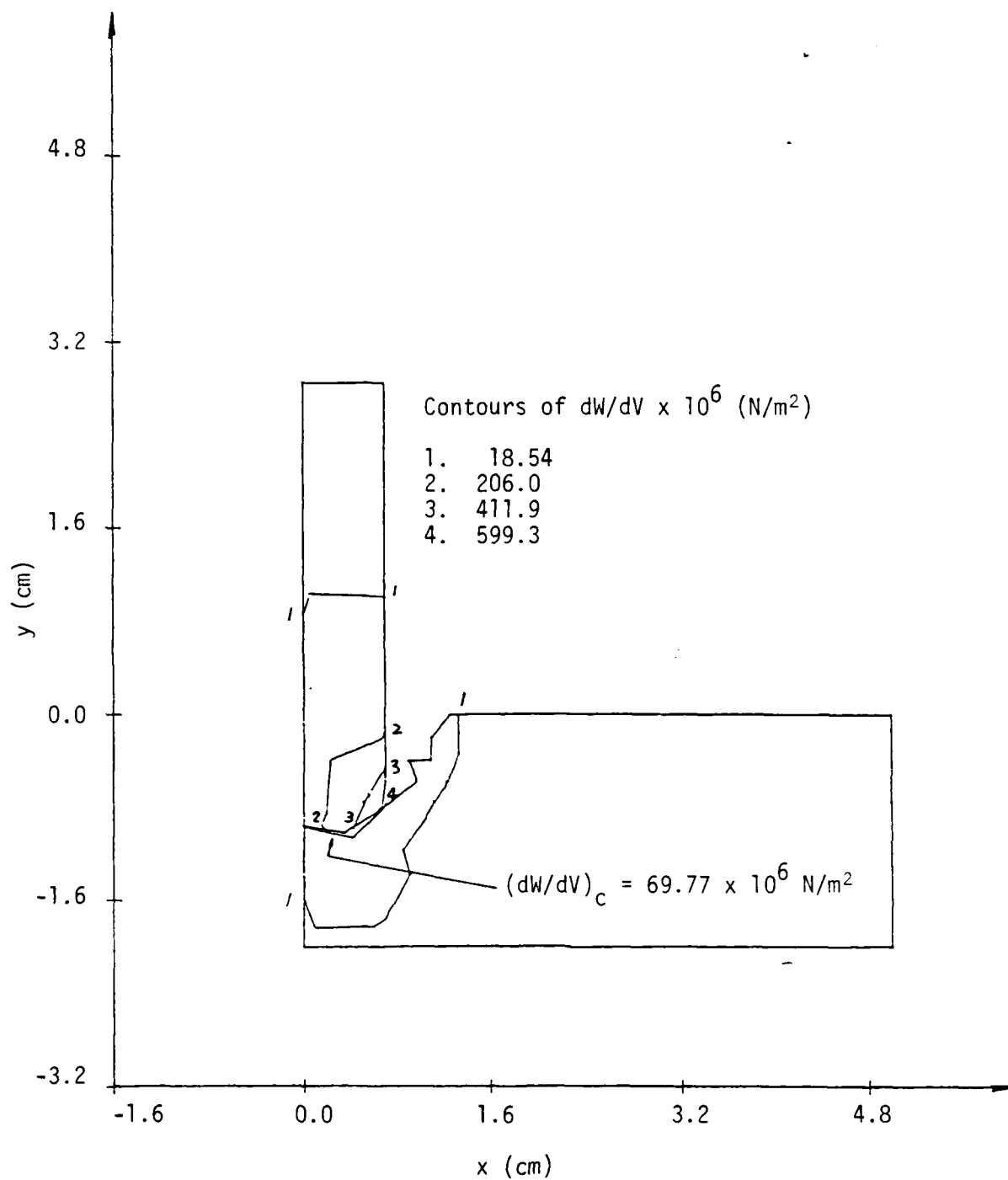


Figure 77. Contours of constant  $dW/dV$  at  $t = 1.265 \mu\text{sec}$ .

target material is dislodged and leaves with the projectile. The final damage configuration of the projectile/target system is shown schematically in Figure 78.

#### CONCLUDING REMARKS

Prediction on the progressive failure of a projectile/target system leading up to plug formation has been presented by application of the energy density theory. No a priori assumption were made on the constitutive relations of the materials that are not only highly stressed but their strain rates change with location and time. Each time interval was carefully chosen such that a complete sequence of the damage pattern is obtained capturing all of the failure modes including permanent deformation, fragmentation, fracture and plug formation. This corresponds specifically to a tungsten projectile with an aspect ratio of 1:3.36 impacting on a 4340 steel target with an aspect ratio of 1:5 at an initial velocity of 1,200 m/sec. The sequence of failure modes depend sensitively on the combination of material type, projectile/target geometry and size and the initial impact velocity. For the problem at hand, the following main sequence of events may be summarized:

- (1) Time t up to 0.480  $\mu$ sec: Owing to the strain and/or energy concentration around the projectile periphery, a cavity is created in the target. This shifts the load transfer to the target material at the center which is still in contact with the projectile.
- (2) Time from t = 0.480 to 0.663  $\mu$ sec: Because of the high load transfer over a small portion of the contacting target material, fragmentation and disintegration of debris occurred leaving a large void or cloud of small fragments between the projectile and target.

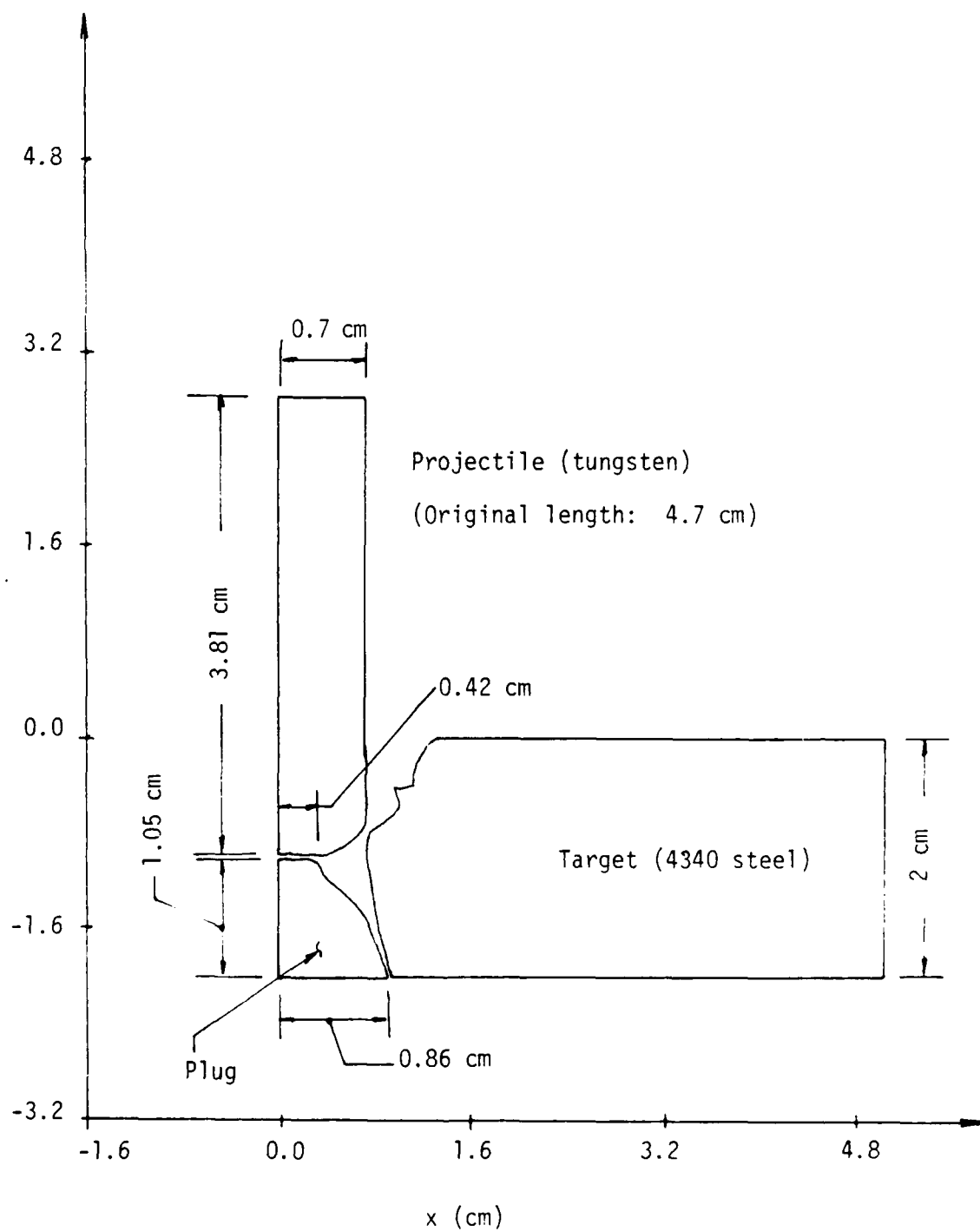


Figure 78. Schematic of failure by plugging.

- (3) Time from  $t = 0.663$  to  $0.924 \mu\text{sec}$ : The projectile although strained and disturbed dynamically travels essentially as a rigid body to close the gap created by fragmentation.
- (4) Time from  $t = 0.924$  to  $1.224 \mu\text{sec}$ : As the projectile catches up to the partially damaged target that is still highly strained, the impact again results in local fragmentation which is not as severe as that which occurred during the time interval from  $t = 0.480$  to  $0.663 \mu\text{sec}$ .
- (5) Time from  $t = 1.224$  to  $1.265 \mu\text{sec}$ : During this time interval, all fragmentation is completed and the remaining energy from the projectile is concentrated along a path that outlines a plug. Its formation represents the onset of complete penetration.

*Penetration Time and Exit Velocity.* An estimate on the time for the projectile to penetrate completely through the target can be made by considering both the time consumed in the damage progress in addition to that required for the projectile to travel as a rigid body. The result must necessarily be greater than  $16.67 \mu\text{sec}$  which corresponds to the time of the original projectile traveling at  $1,200 \text{ m/sec}$  through a distance of  $2 \text{ cm}$ , the thickness of the target plate. Table 8 summarizes the time increments elapsed for a total of 18 steps such that the rigid body time for the projectile is also included beyond step no. 19. Note that the total time up to the onset of plug formation is  $20.085 \mu\text{sec}$ . The additional time required for the projectile and plug to leave the target is  $11.249 \mu\text{sec}$ . This gives a value of  $31.325 \mu\text{sec}$  at which time the plug exits with a velocity of  $802.3 \text{ m/sec}$ . The time history of the projectile velocity is displayed graphically in Figure 79.

Table 8. Time increments leading up to plugging in  $\mu\text{sec}$ .

Step No.	Time Increment	Rigid Body	Total Time
1	0.075		0.075
2	0.045 (0.120)*		0.120
3	0.055 (0.175)		0.175
4	0.065 (0.240)		0.240
5	0.105 (0.345)		0.345
6	0.135 (0.480)		0.480
7	0.021 (0.501)		0.501
8	0.061 (0.562)		0.562
9	0.101 (0.663)		0.663
10	0.101 (0.764)	0.003	0.767
11	0.105 (0.869)	0.008	0.880
12	0.055 (0.924)	0.006	0.941
13	0.100 (1.024)	0.014	1.056
14	0.200 (1.224)	0.348	1.604
15	0.021 (1.245)**	0.764	2.389
16	0.014 (1.259)	3.619	6.023
17	0.005 (1.264)**	9.644	15.671
18	0.001 (1.265)	4.912	20.085

\* Time increment excluding rigid body motion.

\*\* Time step not presented in text.

*Change in Local Strain Rate.* As mentioned earlier, each element in the projectile/target system experiences a different strain rate. The local values depend on the area over which the averages are taken. As an example, consider the grid pattern in Figure 80 for  $t = 1.265 \mu\text{sec}$  that corresponds to the instant of plug initiation. The values of  $\sigma_{\xi}$  and  $\epsilon_{\xi}$  on the damage plane are averaged over the elements no. 220, 221, ---, 247 covering the region where failure is anticipated. Their values are given in Table 9 and plotted in Figure 81 for some typi-



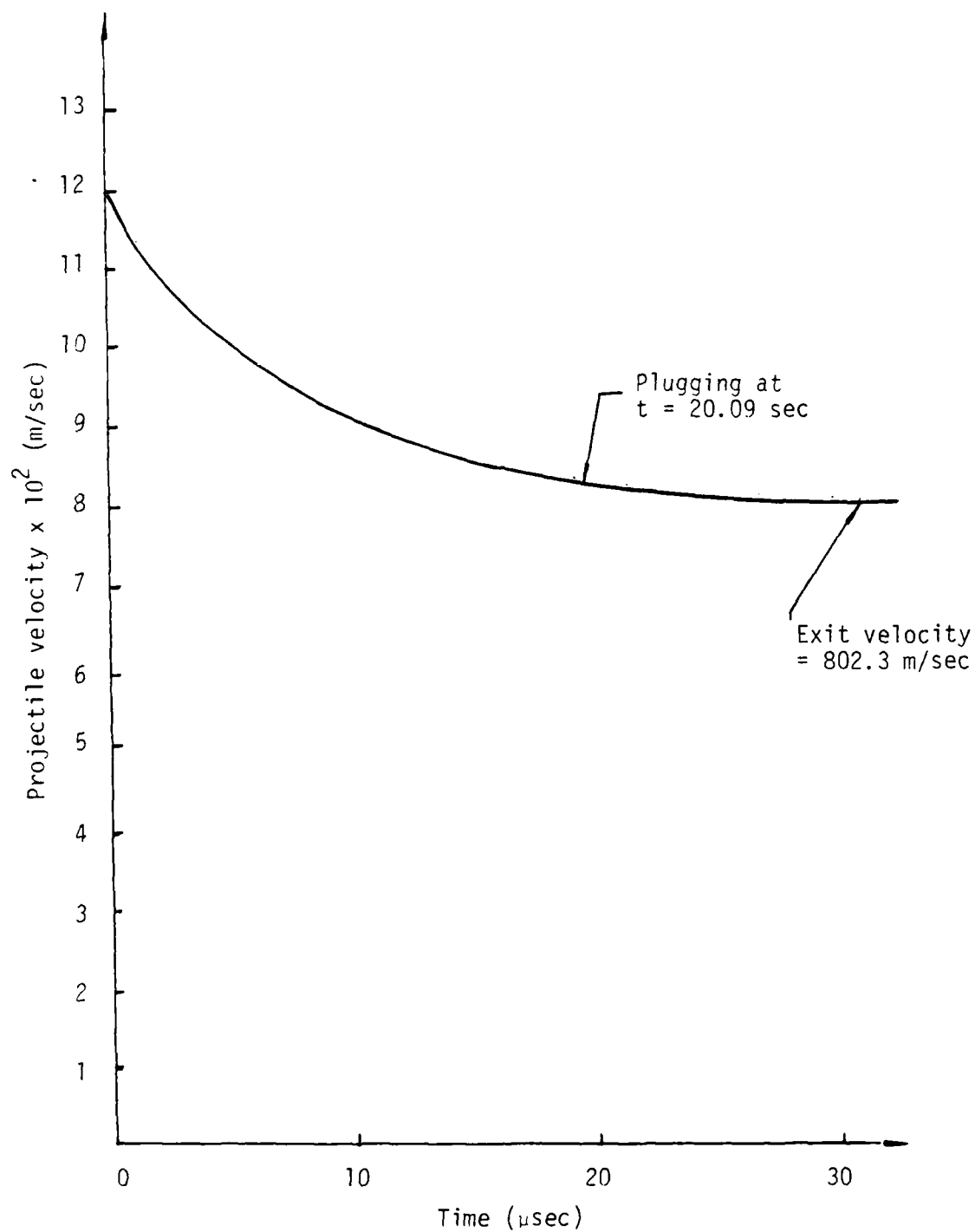


Figure 79. Projectile velocity as a function of time.

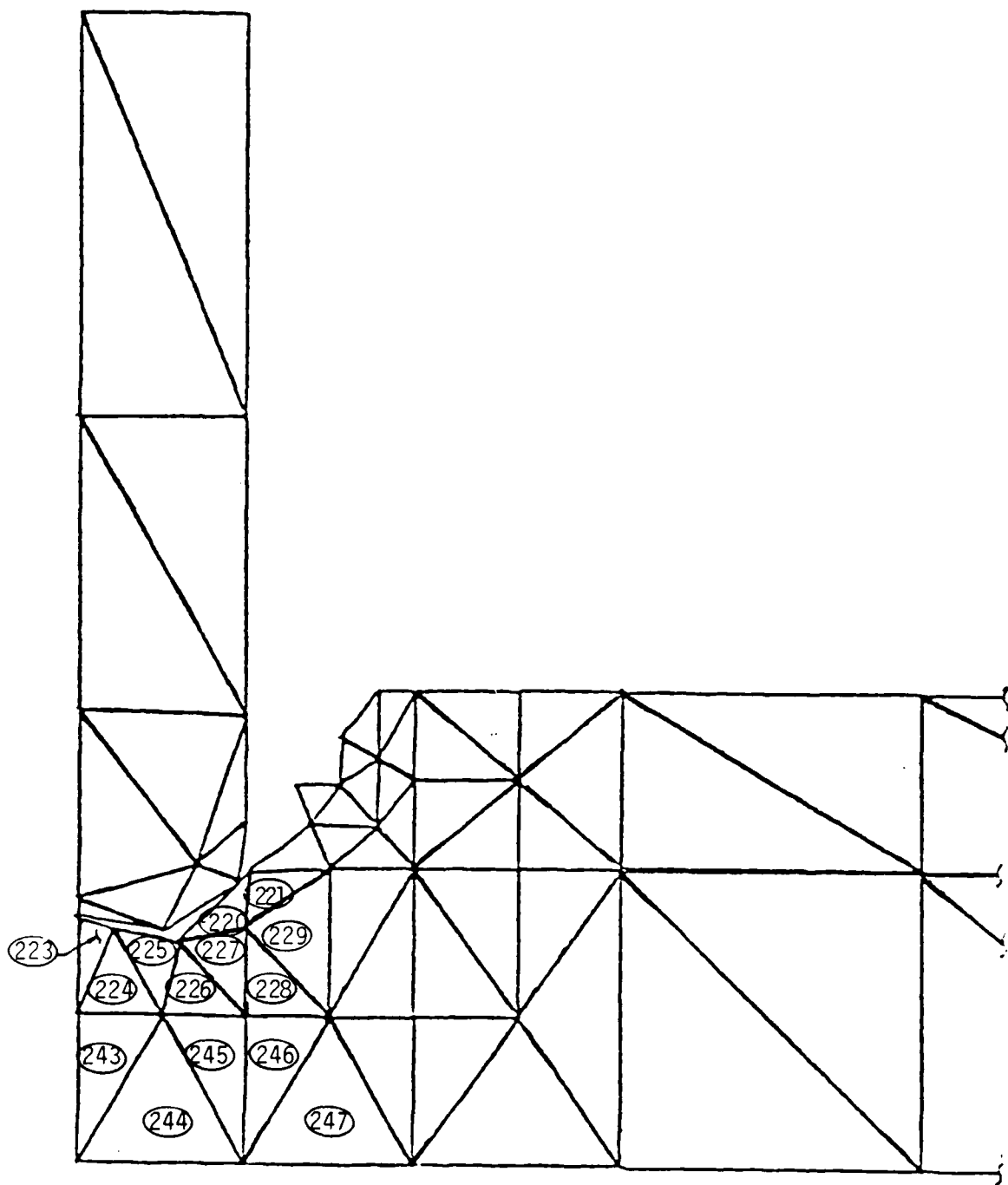


Figure 80. Grid pattern and element numbers at instance of plugging with  $t = 1.265 \text{ } \mu\text{sec.}$

Table 9. Equivalent stress and strain on damage plane for time near plug formation.  
(Refer to Table 8 for the definition of time increment).

Element No.	$t = 2.389 \text{ } \mu\text{sec}$		$t = 6.023 \text{ } \mu\text{sec}$		$t = 15.671 \text{ } \mu\text{sec}$		$t = 20.085 \text{ } \mu\text{sec}$	
	$\sigma_{\xi}$ (GPa)	$\epsilon_{\xi}$ $\times 10^{-2}$ (cm/cm)	$\sigma_{\xi}$ (GPa)	$\epsilon_{\xi}$ $\times 10^{-2}$ (cm/cm)	$\sigma_{\xi}$ (GPa)	$\epsilon_{\xi}$ $\times 10^{-2}$ (cm/cm)	$\sigma_{\xi}$ (GPa)	$\epsilon_{\xi}$ $\times 10^{-2}$ (cm/cm)
220	-1.887	-0.958	-1.895	-1.006	-1.898	-1.022	-1.988	-3.780
221	-1.394	-1.934	-1.400	-2.029	-1.403	-2.063	-1.590	-6.593
225	-0.809	-0.217	-0.900	-0.240	-0.936	-0.249	-1.897	-9.605
226	1.287	0.487	1.289	0.514	-1.290	-0.524	-2.701	-11.700
227	1.016	0.333	1.090	0.357	-1.118	-0.367	-4.057	-0.428
228	-0.383	-0.114	-0.391	-0.116	-0.393	-0.117	-0.394	-0.117
245	-0.353	-0.111	-0.375	-0.118	-0.384	-0.120	-0.385	-0.121
246	-1.062	-0.342	-1.124	-0.362	-1.147	-0.369	-1.151	-0.370
247	-0.116	-0.036	-0.122	-0.038	-0.124	-0.039	-0.124	-0.039

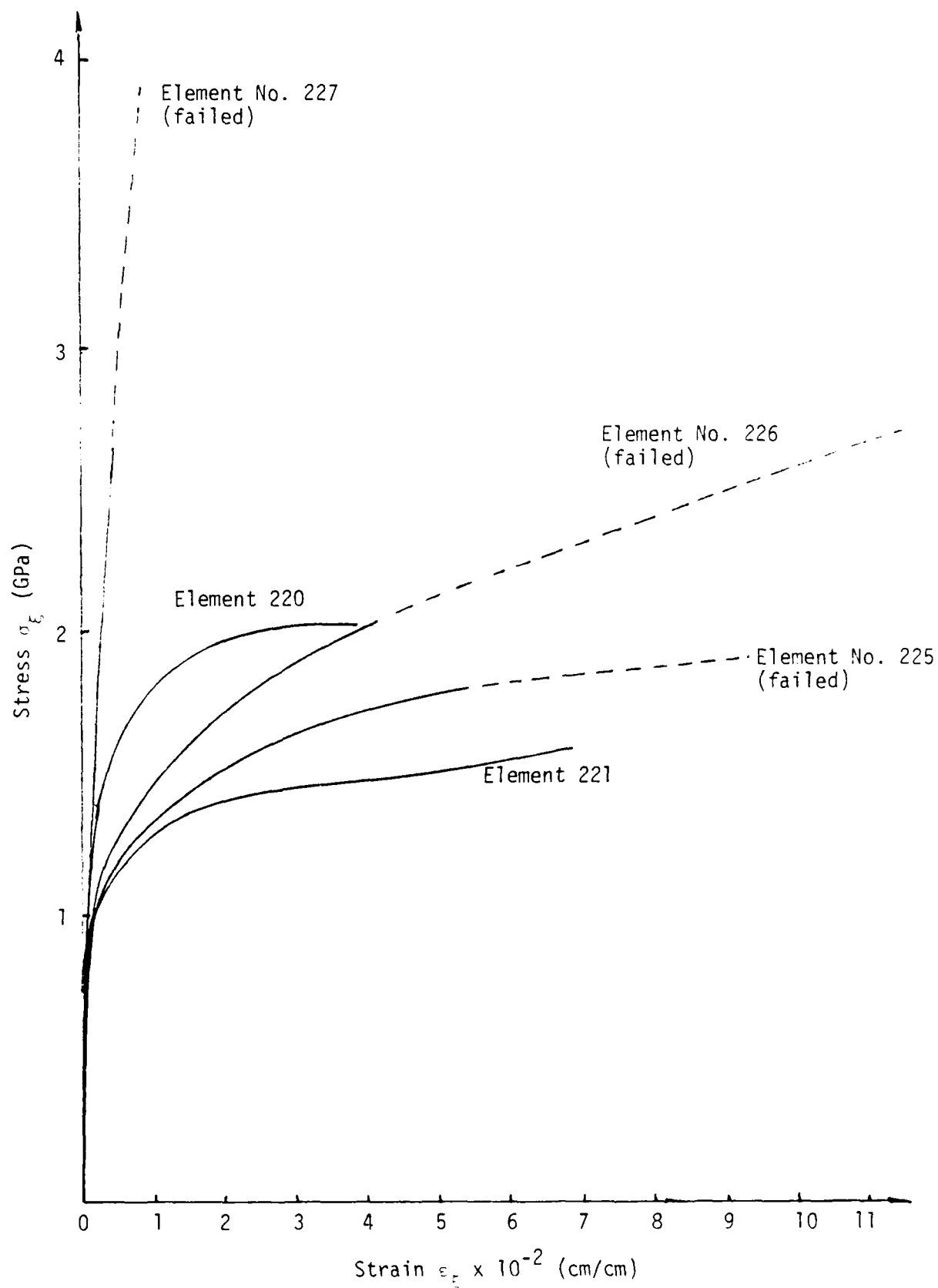


Figure 81. Equivalent uniaxial response in elements no. 220, 221, 225, 226 and 227.

cal elements. Refer to Table 8 for the definition of time elapsed. The difference in the dynamic stress and strain response in the elements near the prospective site of plug formation is obvious. The highest strain rate of  $10^4 \text{ sec}^{-1}$  occurred in element no. 220 and 227 whose sizes are large in comparison with the local region next to the so-called adiabatic shear band which has been observed experimentally [8,9].

A much higher local strain rate up to  $10^6 \text{ sec}^{-1}$  would result if the results are averaged over elements with linear dimensions of the same order as the shear band. Inaccuracy is also anticipated in the region near the backside of the target where local spallation may occur. This can be determined by resulting to smaller elements, a task that will be left for future investigation.

*Thermal/Mechanical Effects.* A salient feature of the energy density theory is that thermal/mechanical effects are automatically considered as inherent in the physical damage process. Because unloading is calculated rather than presumed, dissipation can be determined for each time increment or as a function of time. Without loss in generality, the volume energy density  $dW/dV$  in equation (1) or (26) can be divided into two parts denoted as  $(dW/dV)_p$  and  $(dW/dV)^*$ , i.e.,

$$\frac{dW}{dV} = \left(\frac{dW}{dV}\right)_p + \left(\frac{dW}{dV}\right)^* \quad (43)$$

in which  $D = (dW/dV)_p$  is the dissipation energy density and  $A = (dW/dV)^*$  the available energy density. Their sum represents the area under  $p$  as referred to the true stress and true strain diagram in Figure 82. Once  $D$  is known, the temperature  $\theta$  in each element can be found from [6,7]

$$\frac{\Delta \theta}{\theta} = - \frac{\Delta \sigma_E \Delta \epsilon_E}{\Delta D} \quad (44)$$

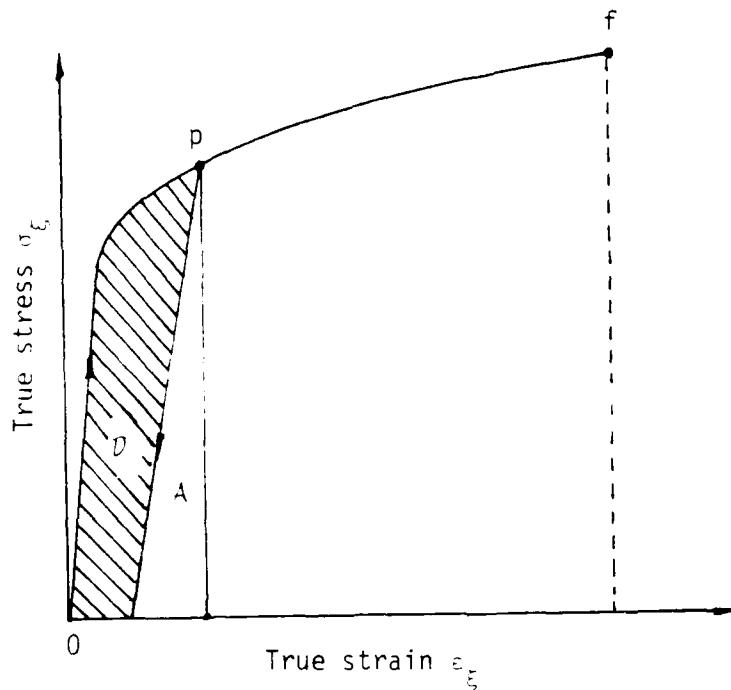


Figure 82. Dissipated and available energy density diagram.

where  $\sigma_\xi$  and  $\varepsilon_\xi$  are the equivalent uniaxial stress and strain on the damage plane. The quantity  $\Delta D / \Delta \varepsilon_\xi$  in equation (44) can be associated with the latent heat in classical thermodynamics for evaluating change in material microstructure or phase transformation, say the melting of solid or the evaporation of liquid. If dissipation takes place all in the form of heat, then  $D \rightarrow Q$  and  $\sigma \rightarrow T$ . It follows that

$$\frac{\Delta D}{\Delta \varepsilon_\xi} \rightarrow \frac{\Delta Q}{\Delta V} = T \frac{\Delta S}{\Delta V} \quad (45)$$

Here,  $\Delta Q$  is the heat required per unit mass of substance in changing the thermodynamic state from  $T$  to  $T + \Delta T$  and  $\Delta V$  is the change of specific volume. The corresponding change in entropy is  $\Delta S$ . Equation (45) can be used to calculate the

latent heat at a given rate and temperature in the 4340 steel near the site where the adiabatic shear band was formed when plugging occurred. A check can thus be available to verify whether the martensite microstructure indeed changes to the austenitic microstructure which was observed experimentally. Such a transformation is *rate dependent*, an effect that cannot be accounted for in classical thermodynamics.

There is no difficulty to include phase transformation in the energy density theory. Projectile/target failure behavior in the hypervelocity range, say 9,000 m/sec, can also be analyzed where the target material under the projectile can transform into liquid and/or gas. The damaged zone of the target may change drastically from the original configuration. Preliminary work on hypervelocity impact has been initiated at the Institute of Fracture and Solid Mechanics at Lehigh University.

## REFERENCES

- [1] L. J. Hageman and J. M. Walsh, "HELP, A Multi-Material Eulerian Program for Compressible Fluid and Elastic-Plastic Flow in Two Space Dimensions and Time", Systems, Science and Software Report 3SR-350, BRL Report BRL-CR-39, 1971.
- [2] G. R. Johnson, "Analysis of Elastic Plastic Impact Invoking Severe Distortion", J. of Appl. Mech., Vol. 98, pp. 439-444, 1976.
- [3] G. R. Johnson, "EPIC-2, A Computer Program for Elastic-Plastic Impact Computations in Two Dimensions Plus Spin", ARBRL-CR-00373, June 1978.
- [4] M. L. Wilkins, R. E. Blum, E. Cronshagen and P. Grantham, "A Method for Computer Simulation of Problems in Solid Mechanics and Gas Dynamics in Three Dimensions and Time", Lawrence Livermore Laboratory, Report UCRL-51574, Rev. 1, 1975.
- [5] G. C. Sih and D. H. Song, "Damage Prediction of Projectile Penetration Process Based on Energy Dissipation Rate", AMMRC Technical Report No. 85-26, Watertown, Massachusetts, August 1985.
- [6] G. C. Sih, "Mechanics and Physics of Energy Density and Rate of Change of Volume with Surface", Journal of Theoretical and Applied Fracture Mechanics, Vol. 4, No. 3, pp. 157-173, 1985.
- [7] G. C. Sih and D. Y. Tzou, "Nonhomogeneous Energy Dissipation Ahead of Slowly Growing Crack", Institute of Fracture and Solid Mechanics, IFSM-84-126, December 1984.



- [8] K. C. Dao and D. A. Shockey, "A Ref. Method for Measuring Shear Band Temperature", J. Appl. Phys., Vol. 50, No. 12, pp. 8244-8246, 1979.
- [9] G. L. Moss, "Shear Strains, Strain Rates and Temperature Damages in Adiabatic Shear Bands", Ballistic Research Laboratory, Aberdeen Proving Ground, Maryland, ARBRL-TR-02242, May 1980.
- [10] J. G. Michopoulos, G. C. Sih, S. C. Chou and J. F. Dignam, "Energy Dissipation in Highly Compressed Cylindrical Bar Specimens", Journal of Theoretical and Applied Fracture Mechanics, Vol. 2, No. 2, pp. 105-110, 1984.
- [11] G. C. Sih and D. Y. Tzou, "Heating Preceded by Cooling Ahead of Crack: Macrodamage Free Zone", Journal of Theoretical and Applied Fracture Mechanics, Vol. 6, No. 2, pp. 103-111, 1986.
- [12] G. C. Sih, D. Y. Tzou and J. G. Michopoulos, "Secondary Temperature Fluctuation in Cracked 1020 Steel Specimen Loaded Monotonically", Journal of Theoretical and Applied Fracture Mechanics, Vol. 7, No. 2, 1987 (in press).

# DISTRIBUTION LIST

No. of  
Copies

To

Office of the Under Secretary of Defense for Research and Engineering (ET),  
The Pentagon, Washington, DC 20301  
1 ATTN: Mr. J. Persh, Staff Specialist for Materials and Structures,  
(Room 3D1089)

Commander, U.S. Army Laboratory Command, 2800 Powder Mill Road,  
Adelphi, MD 20783-1145  
1 ATTN: SLCIS-IM-TL

Commander, Defense Technical Information Center, Cameron Station,  
Building 5, 5010 Duke Street, Alexandria, VA 22304-6145  
2 ATTN: DTIC-FDAC

Commander, U.S. Army Materiel Command, 5001 Eisenhower Avenue,  
Alexandria, VA 22333  
1 ATTN: AMCLD, R. Vitali, Office of Laboratory Management

Director, U.S. Army Strategic Defense Command, P.O. Box 1500,  
Huntsville, AL 35807-3801  
1 ATTN: DASD-H-L, M. Capps  
1 DASD-H-L, Dr. S. Proffitt  
1 DASD-h-h, R. Buckelew  
1 DASD-H-E, J. Katechis

Director, U.S. Army Strategic Defense Command, P.O. Box 1500,  
Huntsville, AL 35807  
1 ATTN: DASD-H-Y, Col. K. Kawano  
1 DASD-H-W, Dr. E. Wilkinson  
1 DASD-H-W, J. Papadopoulos  
1 DASD-H-W, S. Brockway

Director, Defense Nuclear Agency, Washington, DC 20305-1000  
1 ATTN: SPAS, Maj. D. K. Apo  
1 SPLH, J. W. Somers  
1 SPLH, Dr. B. Steverding

Director, Army Ballistic Research Laboratories, Aberdeen Proving Ground,  
MD 21005  
1 ATTN: AMDAR-BLT, Dr. N. J. Huffington, Jr.  
1 AMDAR-BLT, Dr. T. W. Wright

Commander, Air Force Materials Laboratory, Air Force Systems Command,  
Wright-Patterson Air Force Base, Dayton, OH 45433  
1 ATTN: LNC, Dr. D. Schmidt

Commander, BMO/ABRES Office, Norton Air Force Base, CA 92409  
1 ATTN: Capt. S. Opel

No. of  
Copies

To

Commander, Air Force Materials Laboratory, Wright-Patterson Air Force Base,  
Dayton, OH 45433

1 ATTN: AFML/MBM, Dr. S. W. Tsai

Commander, Naval Ordnance Systems Command, Washington, DC 20360

1 ATTN: ORD-03331, Mr. M. Kinna

Naval Post Graduate School, Monterey, CA 93943

1 ATTN: Code NC4(67WT), Prof. E. M. Wu

Commander, Naval Surface Weapons Center, Silver Springs, MD 20910

1 ATTN: C. Lyons

1 C. Rowe

1 Defense Documentation Center, Cameron Station, Building 5, 5010 Duke Street,  
Alexandria, VA 22314

Aerospace Corporation, P.O. Box 92957, Los Angeles, CA 90009

1 ATTN: Dr. R. Cooper

AVCO Corporation, Government Products Group, 201 Lowell Street,  
Wilmington, MA 01997

1 ATTN: Dr. W. Reinecke

1 P. Rolincik

ETA Corporation, P.O. Box 6625, Orange, CA 92667

1 ATTN: D. L. Mykkinen

Fiber Materials, Inc., Biddeford Industrial Park, Biddeford, ME 04005

1 ATTN: M. Subilia, Jr.

1 L. Landers

1 R. Burns

General Electric Company, Convair Division, 5001 Kearney Villa Road,  
San Diego, CA 92138

1 ATTN: J. Hertz

General Research Corporation, 5383 Hollister Avenue, Santa Barbara, CA 93111

1 ATTN: Dr. R. Wengler

1 Dr. R. Parisse

1 J. Green

Hercules Aerospace Corporation, P.O. Box 98, Magna, UT 84044-0098

1 ATTN: Dr. S. W. Beckwith (X2F5)

Kaman Sciences Corporation, P.O. Box 7463, Colorado Springs, CO 80933

1 ATTN: Dr. D. C. Williams

Ktech, 911 Pennsylvania Avenue, N.E., Albuquerque, NM 87110

1 ATTN: Dr. D. Keller

Lawrence Livermore National Laboratory, P.O. Box 808 (L-342), Livermore,  
CA, 94550

1 ATTN: Dr. W. W. Feng

No. of  
Copies

To

Lehigh University, Institute of Fracture and Solid Mechanics,  
Bethlehem, PA 18015

1 ATTN: Dr. George C. Sih  
1 Packard Lab., Bldg. 39

Los Alamos National Laboratory, Los Alamos, NM 87545

1 ATTN: Dr. W. D. Birchler, Mail Stop G787  
1 Henry L. Horak

Martin Marietta Aerospace, P.O. Box 5837, Orlando, FL 32805

1 ATTN: V. Hewitt  
1 Frank H. Koo

Massachusetts Institute of Technology, Department of Aeronautics and  
Astronautics, Cambridge, MA 02139

1 ATTN: Prof. H. H. Pian (Room 311, Bldg. 73)

Pacifica Technology, Inc., P.O. Box 148, Del Mar, CA 92014

1 ATTN: Dr. Ponsford

Radkowski Associates, P.O. Box 5474, Riverside, CA 92507

1 ATTN: Dr. P. Radkowski

Rohr Industries, Inc., P.O. Box 878, Chula Vista, CA 92012-0878

1 ATTN: Dr. T. H. Tsiang, MZ-19T

Sandia Laboratories, P.O. Box 5800, Albuquerque, NM 87115

1 ATTN: Dr. W. Alzheimer  
1 Dr. M. Forrestal  
1 Dr. E. P. Chen, Div. 1524

Southwest Research Institute, 8500 Culebra Road, San Antonio, TX 78206

1 ATTN: A. Wenzel

SPARTA, Inc., 1055 Wall Street, Suite 200, P.O. Box 1354, La Jolla, CA 92038

1 ATTN: J. Wonacott  
1 J. Glatz

Terra Tek, Inc., 420 Wakara Way, Salt Lake City, UT 84108

1 ATTN: Dr. A. H. Jones

University of Washington, FS-10, Guggenheim Bldg., Seattle, WA 98195

1 ATTN: K. Y. Lin

Director, U.S. Army Materials Technology Laboratory, Watertown, MA 02172-0001

2 ATTN: SLCMT-IML  
1 SLCMT-IMA-T  
1 SLCMT-ISC  
1 SLCMT-BM, J. F. Dignam  
25 SLCMT-BM, S. C. Chou (COR)  
1 SLCMT-BM, L. R. Aronin  
1 SLCMT-BM, D. P. Dandekar

U.S. Army Materials Technology Laboratory, Watertown, Massachusetts 02172-0001 FRAGMENTATION AND PLUGGING FAILURE OF PROJECTILE/TARGET SYSTEM G. C. Sih and Y. D. Lee Lehigh University Bethlehem, Pennsylvania 18015 Final Report MIL TR 87-18, March 1987, 120 pp - illus - tables Contract DAAG46-85-K-0011	AD UNCLASSIFIED UNLIMITED DISTRIBUTION Key Words Impact Damage Strain energy methods	The energy density theory is applied to analyze the progressive damage of a projectile/target system with emphases placed on failure by fragmentation and/or fracture. Presented is a finite element code that accounts for the exchange of surface and volume energy density in each element. Such an interaction being neglected in the conventional theories of continuum mechanics plays a major role in the damage process where energy is transferred from the projectile to the target during impact. The dynamically loaded elements are not only highly stressed but they also undergo high gradients of strain whose history is no longer preassumed as in the classical approach. The distribution for each time increment is determined analytically. This enables a realistic prediction of the damage states and provides a consistent means of analyzing projectile/target failure. Results are obtained for a projectile made of tungsten impacting a target plate made of 4340 steel at a velocity of 1,200 m/sec. Appropriate time increments are chosen such that a sequence of damage states can be exhibited leading up to the final fracture of the target plate by plugging whose thickness is approximately one-half of that of the target plate. As thermal/mechanical interaction effects are inherently coupled in the energy density theory, heat dissipation and temperature change are automatically embedded in the solution. Information such as the latent heat used to alter the material microstructure can be found in a straightforward manner for estimating the location and size of the so-called "adiabatic shear band" that occurs during plugging, a topic that will be left for future investigation.
U.S. Army Materials Technology Laboratory, Watertown, Massachusetts 02172-0001 FRAGMENTATION AND PLUGGING FAILURE OF PROJECTILE/TARGET SYSTEM G. C. Sih and Y. D. Lee Lehigh University Bethlehem, Pennsylvania 18015 Final Report MIL TR 87-18, March 1987, 120 pp - illus - tables Contract DAAG46-85-K-0011	AD UNCLASSIFIED UNLIMITED DISTRIBUTION Key Words Impact Damage Strain energy methods	The energy density theory is applied to analyze the progressive damage of a projectile/target system with emphases placed on failure by fragmentation and/or fracture. Presented is a finite element code that accounts for the exchange of surface and volume energy density in each element. Such an interaction being neglected in the conventional theories of continuum mechanics plays a major role in the damage process where energy is transferred from the projectile to the target during impact. The dynamically loaded elements are not only highly stressed but they also undergo high gradients of strain whose history is no longer preassumed as in the classical approach. The distribution for each time increment is determined analytically. This enables a realistic prediction of the damage states and provides a consistent means of analyzing projectile/target failure. Results are obtained for a projectile made of tungsten impacting a target plate made of 4340 steel at a velocity of 1,200 m/sec. Appropriate time increments are chosen such that a sequence of damage states can be exhibited leading up to the final fracture of the target plate by plugging whose thickness is approximately one-half of that of the target plate. As thermal/mechanical interaction effects are inherently coupled in the energy density theory, heat dissipation and temperature change are automatically embedded in the solution. Information such as the latent heat used to alter the material microstructure can be found in a straightforward manner for estimating the location and size of the so-called "adiabatic shear band" that occurs during plugging, a topic that will be left for future investigation.
U.S. Army Materials Technology Laboratory, Watertown, Massachusetts 02172-0001 FRAGMENTATION AND PLUGGING FAILURE OF PROJECTILE/TARGET SYSTEM G. C. Sih and Y. D. Lee Lehigh University Bethlehem, Pennsylvania 18015 Final Report MIL TR 87-18, March 1987, 120 pp - illus - tables Contract DAAG46-85-K-0011	AD UNCLASSIFIED UNLIMITED DISTRIBUTION Key Words Impact Damage Strain energy methods	The energy density theory is applied to analyze the progressive damage of a projectile/target system with emphases placed on failure by fragmentation and/or fracture. Presented is a finite element code that accounts for the exchange of surface and volume energy density in each element. Such an interaction being neglected in the conventional theories of continuum mechanics plays a major role in the damage process where energy is transferred from the projectile to the target during impact. The dynamically loaded elements are not only highly stressed but they also undergo high gradients of strain whose history is no longer preassumed as in the classical approach. The distribution for each time increment is determined analytically. This enables a realistic prediction of the damage states and provides a consistent means of analyzing projectile/target failure. Results are obtained for a projectile made of tungsten impacting a target plate made of 4340 steel at a velocity of 1,200 m/sec. Appropriate time increments are chosen such that a sequence of damage states can be exhibited leading up to the final fracture of the target plate by plugging whose thickness is approximately one-half of that of the target plate. As thermal/mechanical interaction effects are inherently coupled in the energy density theory, heat dissipation and temperature change are automatically embedded in the solution. Information such as the latent heat used to alter the material microstructure can be found in a straightforward manner for estimating the location and size of the so-called "adiabatic shear band" that occurs during plugging, a topic that will be left for future investigation.

END  
DATE  
FILMED

5-88  
DTIC